INFORMATION TO USERS

UNIVERSITY OF OKLAHOMA

GRADUATE COLLEGE

COMPUTER-INTEGRATED FINITE ELEMENT MODELING AND

SIMULATION OF HUMAN MIDDLE EAR

A DISSERTATION

SUBMITTED TO THE GRADUATE FACULTY

In partial fulfillment of the requirements for the

degree of

DOCTOR OF PHILOSOPHY

By

QUNLI SUN

Norman, Oklahoma

2001

UMI Number: 3028807

UMI®

COMPUTER-INTEGRATED FINITE ELEMENT MODELING AND

SIMULATION OF HUMAN MIDDLE EAR

A DISSERTATION APPROVED FOR

THE SCHOOL OF AEROSPACE AND MECHANICAL ENGINEERING

BY

_____
Dr. Kuang-Hua Chang (Chair)
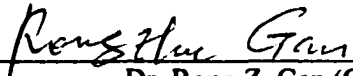
_____
Dr. Rong Z. Gan (Chair)
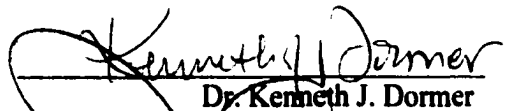
_____
Dr. Kenneth J. Dormer

_____
Dr. John Y. Cheung
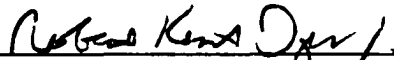
_____
Dr. Robert K. Dyer

_____
Dr. Harold L. Stalford

ACKNOWLEDGMENTS

helping me prepare my defense presentation, and to Jason L. Dickman for fabricating the physical model for me.

Thanks my colleagues, friends, professors and staffs of AME who helped me throughout my studies at OU. I would like specially to acknowledge Lingtao Cao, Sung-Hwan Joo, Wei Lu, Dr. Qiuli Sun, Kaiming Xia and Dr. Huan Zeng for their friendship and help.

There is no word to express my appreciation to my parents and parents-in-law for their understanding and endless love. I would like to thank my brothers, sister, brothers-in-law and sisters-in-law for their encouragement and support. I am greatly indebted to my wife for her unconditional support and love, and also for her assistance in making the histological section slides.

TABLE OF CONTENTS

LIST OF FIGURES

LIST OF TABLES

ABSTRACT

The work reported in this dissertation is the result of a joint venture of biomedical scientists and engineers for understanding human middle ear mechanics through finite element modeling and analysis. The main objective of the research is to explore the middle ear dynamics by using an accurate finite element model of the human middle ear.

The research started with developing a systematic and accurate geometric modeling method that can be employed to reconstruct the middle ear from the histological sections of a human temporal bone in the Computer-Aided Design (CAD) environment. Using the method, a solid model of human middle ear was constructed which reveals excellent accuracy in geometry.

Then a finite element model of the human middle ear was built by using the geometry translated from the CAD model and the published material properties of the middle ear system. The finite element model was finalized as the base-line finite element model by adjusting physical parameters based on the stapes footplate displacements obtained by laser Doppler interferometry measurements. Finally, the accuracy of the base-line finite element model was verified by using four sets of published experimental measurements. These verifications demonstrate that the base-line model constructed using the geometric modeling method developed in this research is adequate in predicting the dynamic behaviors of the middle ear. Therefore, it is appropriate to employ the finite

element model to simulate the middle ear frequency response characteristics, which are the main concerns in the middle ear sound transmission study.

The base-line finite element model was employed for three preliminary clinical applications. The results suggest that the base-line finite element model is very useful in the study of the middle ear mechanics, and the design and test of implantable hearing devices.

CHAPTER ONE

INTRODUCTION

Hearing loss is the second most widely spread impairment in the United States. More than 24 million Americans have a hearing and speech impairment, and 3% of all children are hearing impaired. Because of the rapid increase in the aged population, the number of people with communication disorders is growing faster than the general population [Silverstein *et al.* 1992, VMBHRC 2000]

Dramatic advances in medicine and technology have led to new surgical reconstruction techniques and implantable hearing devices that allow physicians or surgeons to help patients for rehabilitation. The further advancement of the techniques and devices requires a better understanding of transfer characteristics of the ear where the airborne sound is first transformed into mechanical vibrations of the ossicular chain, and then to the fluid vibrations in the inner ear. However, the mechanics of hearing is not yet fully understood, in spite of the considerable amount of research and publications. This is why middle ear mechanics has gained a growing interest in both experiment and modeling over the past years. It is a challenging task to gain more insights into the middle ear mechanics. This task must be tackled by interdisciplinary collaboration of physicians and engineers.

1.1 Middle Ear Modeling: History And Current Status

Attempts to provide an accurate mathematical model of the middle ear began with the work of Helmholtz in 1869. Helmholtz suggested that the eardrum's curvature was the primary cause of the transformer ratio of the middle ear [Helmholtz 1874]. Since then, a number of analysis methods have been attempted to explore the middle ear mechanics. One of the main modeling methods is circuit analog analysis. The method provided many insights and is still used widely in recent years [Zwislocki 1975; Kringlebotn 1988; Goode et al. 1994; Rosowski 1996; Hudde & Weistenhöfer 1997]. However, these circuit analog models are not suitable to capture the actual stress field, detailed vibration modes, the influence of ultrastructural modifications, as well as nonhomogeneous, anisotropic material properties of the middle ear.

Some of these models, such as Onchi [Onchi 1949] and Hudde et al. [Hudde & Weistenhöfer 1997], actually employed multibody dynamics approach [Roberson & Schwertassek 1988]. Even though the circuit analog part is taken away, the method still works by directly solving a set of differential equations. Eiber's model is another valuable multibody model for ossicles [Eiber 1996]. In his analysis, the eardrum was examined by finite element method. Multibody dynamics approach is excellent in dealing with a system with rigid motion but will experience difficulty while modeling a "flabby" body such as the eardrum.

Another main modeling method is the finite element method (FEM). FEM was developed in 1960s as an approach for solving structural mechanics problems. With the rapid advances of computer technology, FEM has been recognized as a powerful, general numerical approximation method for any physical problems that can be formulated as

partial differential equations. FEM has been widely used to investigate biological systems because of the following advantages:

(1) It accurately models the complicated irregular geometry of biological structures;

(2) It realistically models the non-homogenous, anisotropic mechanical properties of the biological materials;

(3) Its various result-visualization methods, such as numerical, graphical and animated ones, enable the result to be understood and interpreted easily and accurately.

The investigation on the FEM analysis of the middle ear mechanics has been reported in many papers. Different finite element (FE) models have been used to simulate the static or dynamic behaviors of the subsets of the middle ear or the entire middle ear.

The first FE model of the eardrum was presented by Funnell et al. in 1978. It was a static three dimensional (3D) model of the cat [Funnell & Laslo 1978]. The inertial effects were later added to the model, and the natural frequencies and mode shapes were calculated [Funnell 1983]. The damping effects were not included in either of those two models. The damping effects were added and the frequency responses of the cat eardrum were compared with the experimental results in a later paper [Funnell, Decraemer & Khanna 1987]. A further improvement was completed by incorporating an elastic manubrium into the model [Funnel, Khanna & Decraemer 1992]. In this paper, it is worth mentioning that the manubrium was reconstructed from serial histological sections. A set of histological sections of a cat middle ear were used to reconstruct the geometry of the ossicles, the posterior incudal ligament and the manubrium for the finite element model. However, no detailed discussion was revealed to delineate how to generate the 3D surfaces by joining a set of histological section contours and how to determine the relative spatial positions and

orientations among the middle ear components. Based on the model developed in 1987, the mechanical coupling between the eardrum and the manubrium was studied [Funnell 1996]. In these papers, the actions of the ossicular chain and cochlea on the eardrum were represented as a single effective torsional stiffness and a moment of inertia at the "hinge" of the manubrium. The model (developed in 1992) was also improved by adding explicit representations of the ossicles and the cochlear load. The effects of two types of middle ear surgeries were simulated using this improved cat middle ear model [Ladak & Funnell 1996]. The modeling method of Funnell et al. is simple but may not accurate due to the limited geometric information. Their interests seemed to focus on the investigation of the characteristics of cat middle ears.

Following the eardrum modeling procedure of Funnell et al. a FE model of the eardrum was developed to build an eardrum rupture criterion by Stuhmiller [Stuhmiller 1989]. Stuhmiller quantified the blast environment into different types of pressure histories and successfully related the tensile stress responsible for injuries to various types of pressures by static and dynamic response analyses.

William et al. began publishing their models in 1988. A two dimensional (2D) cross sectional model, including eardrum and malleus, was created to examine the static behavior of the human eardrum [Lesser & Williams 1988]. A different 2D cross sectional model of the eardrum was developed to relate some diseases to the maximum shearing stress of the eardrum [Lesser, Williams & Skinner 1988]. Another 2D cross section model was employed to investigate the stress and displacement levels in the reconstructed ossicular chain [Lesser, Williams & Blayney 1991]. The 2D cross sectional model revealed some of the static and dynamic characteristics of the middle ear. However, these models are oversimplified.

4

The first 3D middle ear FE model of Williams *et al.* was published in 1990 to examine the effect of several eardrum geometric and material parameters on the natural frequencies of the eardrum [Williams & Lesser 1990]. The geometric modeling method is similar to Funnell *et al.*'s, but the different element type and varying eardrum thickness were employed in the FE model. Note that no ossicular loading was incorporated in the model. The model was modified to investigate dynamic characteristics of the Fisch II spandrel total ossicular replacement prosthesis [Williams & Lesser 1992]. The model was improved by introducing beam elements connected at the nodes of shell elements in order to simulate the radial and circumferential fibers of the eardrum's ultrastructure. This model was employed to examine the dynamic behaviors of the normal eardrum [Williams & Lesser 1993], as well as the mode shapes of damaged and repaired eardrums [Williams, Blayney & Lesser 1997]. The model was modified by adding solid elements to represent malleus and incus, and was employed to investigate the dynamic behaviors of the reconstructed middle ear using two different stapes replacement [Williams, Blayney & Lesser 1995]. The modified model was later used to examine the dynamic characteristics and the harmonic response of diseased, repaired and reconstructed middle ear [Williams, Blayney & Rice 1996a,b; Blayney, Williams & Rice 1997]. The geometric modeling method of Williams *et al.* is very similar to Funnell *et al.*'s, which is simple but inaccurate due to the insufficient geometric information. Values of some of the physical parameters employed in their models seem unreasonable compared to the published data. The main contributions of Williams *et al.* lie in the fact that their work related the mechanics characteristics of the middle ear to the clinical applications.

The middle ear FE model of Wada *et al.* was published in 1992 [Wada, Metoki & Kobayashi 1992]. Their model included eardrum, ossicles and cochlear impedance; and it was

assumed a fixed rotational axis from the anterior process of malleus to the short process of the incus. So the elasticity of the anterior mallear ligament and the posterior incudial ligament was neglected. The mechanical properties and boundary conditions of the middle ear were determined by comparing the numerical results obtained from the FE analysis and those measured from fresh cadavers. The model was modified in their later papers [Wada, Koike & Kobayashi 1996; Koike, Wada et al. 1996] to include middle ear ligaments, middle ear cavity (as a rectangular solid) and ear canal (as a rigid tube). The forced frequency response to an acoustic excitation was performed. The model was also employed to investigate the acoustic properties of some middle ear prostheses [Koike, Wada & Kobayashi 2000].

An accurate geometric modeling method for the components of the human middle ear was presented by Beer *et al.* [Beer et al. 1996; Drescher, Schmidt & Hardtke 1998]. In this method, the surfaces of the middle ear components including malleus, incus, stapes and eardrum were measured by laser scanning microscopy, and then the geometric model for each middle ear component was created based on the characteristic points measured. The FE models of the middle ear obtained by this method were assembled into different sub-models to investigate their dynamic characteristics [Beer et al. 1996; Drescher, Schmidt & Hardtke 1998; Beer et al. 1999]. The submodel of the eardrum with malleus and ligaments was also employed to conduct parameter identification study [Bornitz et al. 1999], and to examine the dynamic behavior of the middle ear reconstructed by a special Bell prosthesis [Zahnert et al. 1996]. The geometric modeling method employed by Beer *et al.* is very accurate for each component. However, although the scaling procedure was performed for assembly, the inconsistency between different components was unavoidable because each component came from different

temporal bones. And it's hard to keep these components in proper spatial positions and orientations while assembling. They did not present a model of the entire middle ear.

A middle ear FE model created by Prendergast et al. was published in 1999 [Prendergast, Ferris et al. 1999]. The model is very similar to Wada et al.'s, both in geometry and in mechanical properties. The important differences of Prendergast et al.'s model from Wada et al.'s are: (1) The ear canal was modeled more accurately than Wada et al.'s, (2) anisotropic and non-homogenous mechanical properties were used in eardrum, and (3) the boundary conditions of the eardrum and the incudomallear joint were handled in a way different from Wada et al.'s. The model was employed to examine the middle ear dynamic characteristics, with and without a partial or total ossicular replacement [Ferris & Prendergast 2000]. The model was also used to investigate the effect of the ventilation tubes on stresses and vibration modes of the eardrum [Prendergast, Kelly et al. 1999].

The models of Wada et al. and Prendergast et al.'s were categorized as the detailed analysis models with validations. But the predication may be impaired by their inaccurate geometry, especially when the analysis results are not so satisfactory compared with experimental results as presented in Prendergast et al.'s work.

It is well known that an accurate 3D geometric model of the human middle ear is the crucial first step for developing a 3D FE model for middle ear mechanical analysis. A review about the accurate geometric reconstruction of the ear is presented next. Besides Funnell et al. and Beer et al. mentioned above, other authors who developed accurate ear geometric reconstruction methods include Takagi et al., Fujiyoshi et al. and Weistenhöfer et al.. Although these methods were developed for other applications, for example, the cochlear length measurement, they can also be used for finite element modeling. Takagi

and Sando's method for studying the 3D structure of the temporal bone provided a wire frame model of the cochlea [Takagi & Sando 1989; Takahashi *et al.* 1989]. In the method, each histological section of the temporal bone was projected onto a paper for magnification. Then these papers with magnified images were stacked and aligned, and the outlines of the structures were input into a computer by a digitizer. Obviously, the error induced in this procedure was not trivial. Fujiyoshi *et al.* proposed a method for reconstructing the temporal bone, which is similar to Takagi and Sando's method except for the histological section preparation [Fujiyoshi, Mogi *et al.* 1992]. Fujiyoshi *et al.* employed a microscope television camera for section digitization and 3D-reconstruction software for creating the geometry of a monkey ear. These two methods seem to capture detailed geometric information with some success. However, the models were not connected to commercial CAD (Computer-Aided Design) software for the computer-integrated application. Weistenhöfer and Hudde presented a two-step procedure to create a geometric model of human ossicles [Weistenhöfer & Hudde 1999]. The ossicles' silhouettes under different but well-defined angles were projected on to paper using a special device and an overhead projector. The silhouettes were captured by hand drawing on the paper and scanned into computer. The solid geometric models of ossicles were then generated by extruding those silhouettes in AutoCAD [Autodesk, Inc. 1995]. This procedure may provide accurate geometry for the ossicles. However, it is difficult to determine proper spatial positions and orientations of each ossicles while assembling. Furthermore, it is almost impossible to create geometry of the eardrum by using this procedure.

All authors mentioned above tried to develop an accurate model of the middle ear. Their models are either geometric or FE. All existing models of the middle ear

contributed to the advancement of the middle ear mechanics in following aspects:

(1) Geometric reconstruction of the middle ear;

(2) Finite element modeling of the middle ear;

(3) Investigation and test of the middle ear material properties;

(4) Calibrations and verifications of finite element models of the middle ear;

(5) Clinical applications of finite element models of the middle ear.

However, no model is perfect. In addition, there is not a feasible computer-integrated finite element modeling method to systematically combine all the aspects together. Therefore, a simple, systematic and computer-integrated method is needed to help researchers create accurate finite element models of the entire human middle ear, including malleus, incus, stapes, eardrum, articulations and other suspensory ligaments and muscles. And a better FE model of the middle ear is needed to predict the dynamic behaviors of normal, diseased, and altered human middle ears.

1.2 Hypotheses And Objectives

As we know, all research is hypothesis driven. The hypotheses of this study are formulated as follows:

(1) Finite element method can be used to predict the dynamic behaviors of normal, diseased, and altered human middle ears;

(2) An accurate and systematic geometric modeling method can be developed to support the human middle ear FE modeling;

(3) The FE middle ear model can be calibrated using experimental results to produce the base-line FE model;

(4) Clinical applications can be characterized by identifying and quantifying FE model parameters such as geometric characteristic parameters and material properties.

Based on the hypotheses formulated above, the objectives of this proposed research are defined as follows:

(1) Understand middle ear mechanics by combining the FE structural frequency response analysis and the Laser Doppler Interferometry (LDI) experimental measurements.

(2) Develop a computer-integrated modeling method that supports engineers to convert a set of histological sections into an accurate finite element model.

(3) Create a base-line middle ear finite element model that captures the structural characteristics of human middle ear.

(4) Simulate the diseased or altered middle ear by varying parameters of the base-line FE model, which link to realistic clinical applications.

1.3 Approaches

In this research, advanced computer-based modeling and simulating techniques, namely, experiment- and computer-based imaging processes, Computer-Aided Design (CAD) [Lee 1999] and Computer-Aided Engineering (CAE) [Lee 1999] are employed to reconstruct the geometry of human middle ear, and to explore the middle ear mechanics. The whole research can be categorized into four parts: theoretical and FE modeling preparations, geometric modeling, FE modeling and FE simulations, as shown in Figure 1.1. The theoretical and FE modeling preparation utilizes the finite element method and structural vibration theory, describes the basic FE modeling procedure by creating a simple model, and investigates the material properties of middle ear components and attachments. This part will be discussed in Chapters 2 and 3. The second part, an advanced geometric modeling method, will be introduced in Chapter 4. The FE modeling will be discussed in Chapter 5 with the detailed considerations in the middle ear FE modeling and the model verifications. Chapter 6 introduces some clinical applications of the FE model, such as the stapes rocking study, the mass loading effect of implants and the eardrum stiffness study. Chapter 7 gives the conclusions of the research and recommendations for future work.
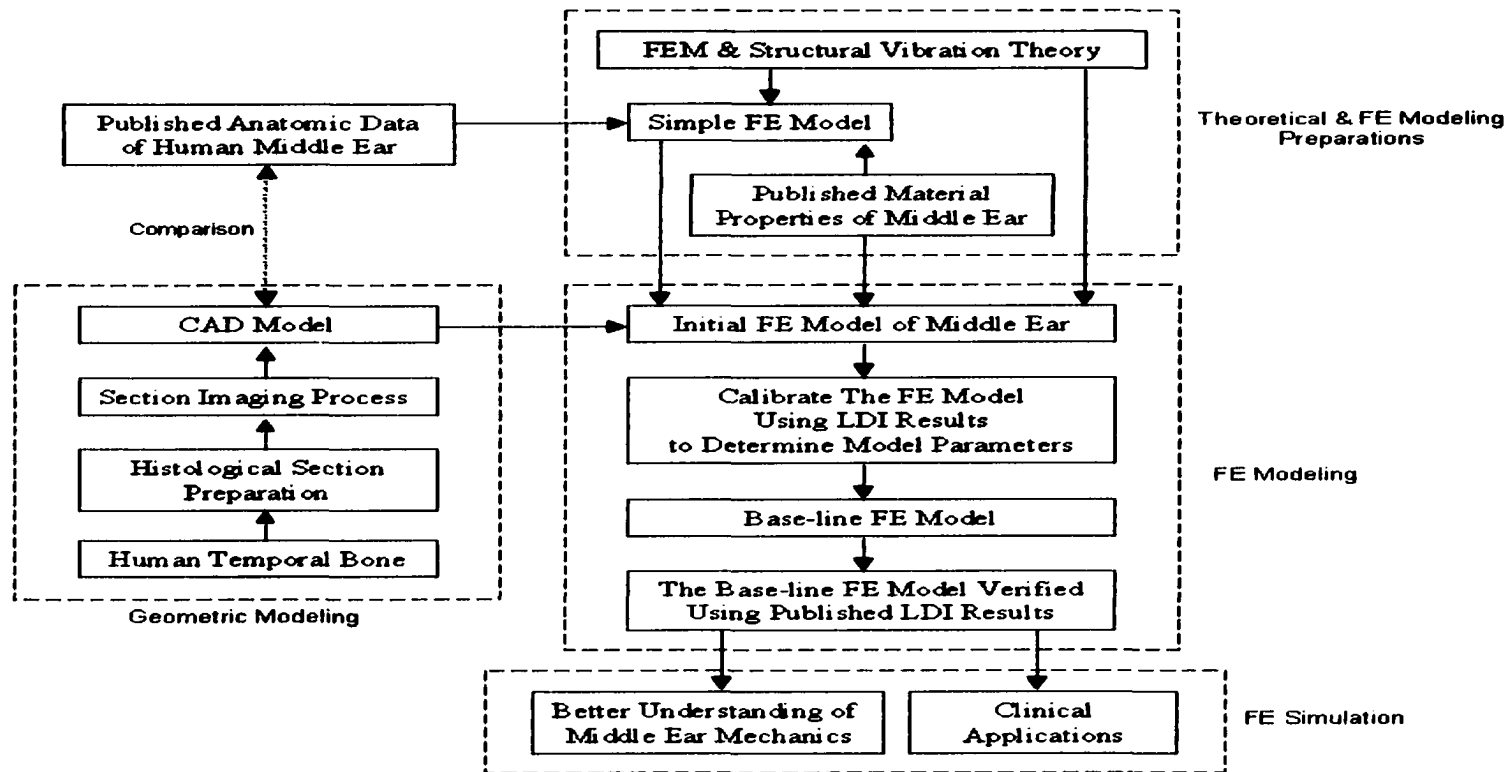
Figure 1.1 Computer-integrated FE modeling and simulation of human middle ear

CHAPTER TWO

FUNDAMENTALS OF FINITE ELEMENT ANALYSIS

This chapter provides the basic concepts, basic theory and solution techniques of the finite element method (FEM) for structural dynamic problems. The contents in this chapter are the key for understanding how to convert the middle ear mechanical analysis into a structural dynamic analysis, although some work described in this chapter can be taken care of by ANSYS [SAS IP Inc. 1998a], a commercial FEM software that was employed in the research. The contents in this chapter are also the key to correctly solving problems using commercial software and interpreting results. The first two sections describe the basic concepts and equations of finite element structural analysis [Szabó & Babuška 1991]. The third section introduces a solution technique for structural dynamic problems. The fourth section discusses damping expression in structural analysis [Gatti & Ferrari 1999; Hart & Wong 2000]. The chapter closes with the descriptions of element types employed in this research [SAS IP Inc. 1998b].

2.1 Basic Concepts Of The Finite Element Method

The finite element method is a computer-based computation method that can be used to analyze a field, which is defined as a physical quantity varying with position within the object. There are many kinds of fields, and each field has a different influence on the object's performance. The fields are related to the potentials as their derivatives with

respect to position. The exact form of the spatial derivative may vary with the type of fields. In this research, the object is a structure like the middle ear system, so the introduction to FEM is devoted to structural problems. For a structure, the field is stress and the potential is displacement. In general, a structure serves to resist applied loads and other influences. The theory requires discretization of a given structure into a network of finite elements and implementation of the analysis on a digital computer. Advances in computer hardware and software have made it easier and more efficient to use FEM for solving complex structural problems.

A finite element (FE) is a subregion of a continuum. It is of finite size (not infinitesimal) and usually has a simpler geometry than that of the continuum. The points where the finite elements are interconnected are called nodes or nodal points, and the procedure in selecting the nodes and forming finite elements is called discretization. FEM enables us to convert a problem with an infinite number of degrees of freedom to one with a finite number in order to simplify the solution process. FEM yields an approximate solution based on an assumed displacement function, stress function, or a mixture of them within each finite element, which are called shape functions. The assumption of displacement functions is the most commonly used technique.

FEM begins with building a finite element model of a structure. The FE model is an assembly of finite elements, which are obtained by discretizing the continuum. The finite element model contains the following information about the structure:

- Geometric domain, which is subdivided into finite elements;
- Material properties, which is assigned to each finite element;
- Loads, which are applied as exciting force;

- Constraints, which are applied to prevent rigid body motion.

Material properties, loads, and constraints can often be expressed quickly and easily, but geometry is usually difficult to describe for a complex structure. A typical structural finite element analysis includes the following steps:

(1) Discretize the structure. The structure is divided in to finite elements. Finite element analysis (FEA) preprocessors, such as HyperMesh [Altair Computing Inc. 1997] and Patran [MacNeal-Schwendler Corporation 1998], help the user create the finite element meshes. This is one of the most crucial steps in determining the solution accuracy of the problem.

(2) Define the element properties. At this step, the user must define the element material properties and select the types of finite elements that are the most suitable to model the physical system.

(3) Assemble the element mass, damping and stiffness matrices. The mass, damping and stiffness matrices of any element can be derived from an energy method based on its assumed shape function. They are then assembled to form the mass, damping and stiffness matrices of the system. These matrices relate the nodal displacement, velocity and acceleration to applied forces at the nodes.

(4) Apply the loads. Externally applied concentrated or distributed forces, moments, and ground motions are provided at this step.

(5) Define boundary conditions. The support conditions must be provided, i.e., the nodal displacements at some boundaries must be set to known values.

(6) Solve the system of linear algebraic equations. The above steps lead to a system of simultaneous algebraic equations where the nodal displacements are the unknowns.

(7) Calculate stresses, reactions, natural modes or other pertinent information.

2.2 Basic Equations Of The Finite Element Method

2.2.1 Basic Equations In Elasticity

For an elastic continuum under loads including body forces and boundary surface loads, as shown in Figure 2.1 (a), the stress state at any point can be expressed by nine
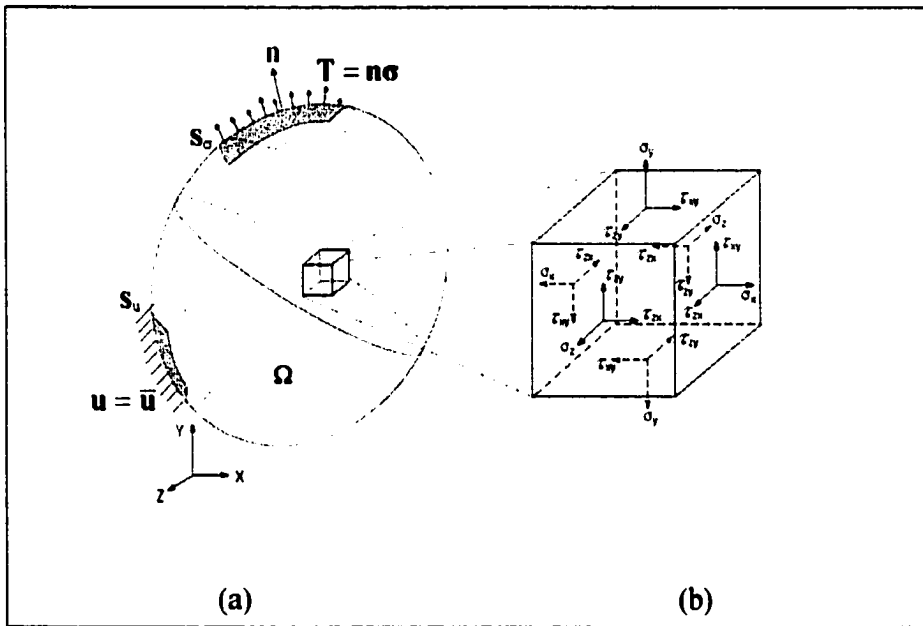
Figure 2.1 An elastic continuum and an infinitesimal element in its field
(The body forces, **b**, are not shown in the figure)

stress components with respect to a right-hand orthogonal coordinate system. The body forces are denoted by b_x, b_y and b_z that are the forces per unit volume in the respective x-, y- and z-directions of the coordinate system and can be written in a vector form as

$$\mathbf{b} = \{b_x, b_y, b_z\}^T \tag{2.1}$$

where the superscript "T" means the transpose of a vector or matrix. Figure 2.1 (b) shows an infinitesimal element of the continuum at any given point in the Cartesian coordinates,

with the edges of *dx*, *dy* and *dz* long. The normal and shear stresses are indicated by arrows on the faces of the infinitesimal element. The normal stresses are labeled σ_x, σ_y, and σ_z, whereas the shear stresses are labeled τ_{xy}, τ_{yz}, τ_{zx}, τ_{yx}, τ_{zy}, and τ_{xz}. From equilibrium of the element, we know

$$\tau_{xy} = \tau_{yx}, \quad \tau_{yz} = \tau_{zy}, \quad \tau_{xz} = \tau_{zx}. \tag{2.2}$$

Therefore only six stress components are independent. Corresponding to stresses, the deformation is expressed as normal and shear strains. Normal strains, ε_x, ε_y, and ε_z, are defined as

$$\varepsilon_x = \frac{\partial u}{\partial x}, \quad \varepsilon_y = \frac{\partial v}{\partial y}, \quad \varepsilon_z = \frac{\partial w}{\partial z} \tag{2.3}$$

where *u*, *v* and *w* are displacements at the given point in the respective x-, y- and z-directions. Shear strains, γ_{xy}, γ_{yz}, γ_{zx}, γ_{yx}, γ_{zy}, and γ_{xz} are defined as

$$\gamma_{xy} = \frac{\partial u}{\partial y} + \frac{\partial v}{\partial x} = \gamma_{yx}, \quad \gamma_{yz} = \frac{\partial v}{\partial z} + \frac{\partial w}{\partial y} = \gamma_{zy}, \quad \gamma_{xz} = \frac{\partial u}{\partial z} + \frac{\partial w}{\partial x} = \gamma_{zx}. \tag{2.4}$$

Obviously, only three of the shear strains are independent. For convenience, the stresses, strains and displacements are represented as vectors

$$\boldsymbol{\sigma} = \left\{ \sigma_x, \sigma_y, \sigma_z, \tau_{xy}, \tau_{yz}, \tau_{zx} \right\}^T, \quad \boldsymbol{\varepsilon} = \left\{ \varepsilon_x, \varepsilon_y, \varepsilon_z, \gamma_{xy}, \gamma_{yz}, \gamma_{zx} \right\}^T, \quad \mathbf{u} = \left\{ u, v, w \right\}^T. \tag{2.5}$$

According to the dynamic equilibrium of an infinitesimal element, we have the dynamic equilibrium equation

$$\mathbf{L}^T \boldsymbol{\sigma} + \mathbf{b} = \rho \ddot{\mathbf{u}} + \mu \dot{\mathbf{u}} \tag{2.6}$$

where ρ is the mass density and μ is the damping factor. $\mathbf{L}^T$ is the transpose of a linear differential operator that is defined to satisfy matrix manipulation as

$$L = \begin{bmatrix} \dfrac{\partial}{\partial x} & 0 & 0 & \dfrac{\partial}{\partial y} & 0 & \dfrac{\partial}{\partial z} \\ 0 & \dfrac{\partial}{\partial y} & 0 & \dfrac{\partial}{\partial x} & \dfrac{\partial}{\partial z} & 0 \\ 0 & 0 & \dfrac{\partial}{\partial z} & 0 & \dfrac{\partial}{\partial y} & \dfrac{\partial}{\partial x} \end{bmatrix}^{\text{T}} . \tag{2.7}$$

Equations (2.3) and (2.4) are called the strain-displacement relationships and can be written as

$$\varepsilon = Lu . \tag{2.8}$$

The stress-strain relationships can be written in matrix form as

$$\sigma = D\varepsilon \tag{2.9}$$

where **D** is called the elasticity matrix and can be drawn from the theory of elasticity. For an isotropic material,

$$D^{-1} = \frac{1}{E} \begin{bmatrix} 1 & -v & -v & 0 & 0 & 0 \\ -v & 1 & -v & 0 & 0 & 0 \\ -v & -v & 1 & 0 & 0 & 0 \\ 0 & 0 & 0 & 2(1+v) & 0 & 0 \\ 0 & 0 & 0 & 0 & 2(1+v) & 0 \\ 0 & 0 & 0 & 0 & 0 & 2(1+v) \end{bmatrix} \tag{2.10}$$

where E is Young's modulus, v is Poisson's ratio and the superscript "–1" means the inverse of a matrix. For an orthotropic material,

$$D^{-1} = \begin{bmatrix} 1/E_x & -v_{xy}/E_y & -v_{xz}/E_z & 0 & 0 & 0 \\ -v_{yx}/E_x & 1/E_y & -v_{yz}/E_z & 0 & 0 & 0 \\ -v_{zx}/E_x & -v_{zy}/E_y & 1/E_z & 0 & 0 & 0 \\ 0 & 0 & 0 & 1/G_{xy} & 0 & 0 \\ 0 & 0 & 0 & 0 & 1/G_{yz} & 0 \\ 0 & 0 & 0 & 0 & 0 & 1/G_{zx} \end{bmatrix} \tag{2.11}$$

where E_x and E_y are the Young's modulus in the x- and y-directions, respectively. G_{xy}, G_{yz} and G_{zx} are the shear modulus in the xy-, yz- and zx-planes, respectively. ν_{xy}, ν_{yx}, ν_{yz}, ν_{zy}, ν_{xz} and ν_{zx} are the Poisson's ratios and satisfy

$$\frac{\nu_{yx}}{E_x} = \frac{\nu_{xy}}{E_y}, \quad \frac{\nu_{zx}}{E_x} = \frac{\nu_{xz}}{E_z}, \quad \frac{\nu_{zy}}{E_y} = \frac{\nu_{yz}}{E_z}. \tag{2.12}$$

On a part of the boundary exist surface loads, denoted T_x, T_y and T_z, which are the forces per unit area in x-, y- and z-directions. The part of the boundary is called force boundary, denoted as S_σ, and the surface loads can be written in vector as

$$\mathbf{T} = \left\{T_x, T_y, T_z\right\}^{\mathrm{T}}. \tag{2.13}$$

The boundary that has known displacements $\bar{\mathbf{u}}$ is called the displacement boundary, denoted as S_u. Thus, the boundary conditions are expressed by

$$\mathbf{T} = \mathbf{n\sigma} \quad (on\, S_\sigma) \quad , \quad \mathbf{u} = \bar{\mathbf{u}} \quad (on\, S_u) \tag{2.14}$$

where $\mathbf{n}$ is an operator consisted of the directional cosines of the outer normal of the force boundary, n_x, n_y and n_z, and is defined as

$$\mathbf{n} = \begin{bmatrix} n_x & 0 & 0 & n_y & 0 & n_z \\ 0 & n_y & 0 & n_x & n_z & 0 \\ 0 & 0 & n_z & 0 & n_y & n_x \end{bmatrix}. \tag{2.15}$$

2.2.2 Structural Dynamic Equilibrium Equations

In FEM, a structure such as the middle ear system is first discretized as an n-degree of freedom finite elements system. Every element can be regarded as a continuum as shown in Figure 2.1 (a). The nodal displacement vector of any element is represented by

$$\mathbf{d}^e = \left\{d_1, d_2, \cdots, d_{ne}\right\}^{\mathrm{T}} \tag{2.16}$$

where *ne* is the number of degrees of freedom of the element. Assume displacement shape functions, $\mathbf{N}(x,y,z)$, that relate generic displacements to nodal displacements as follows:

$$\mathbf{u} = \mathbf{N}(x,y,z)\mathbf{d}^e . \tag{2.17}$$

The discussion on displacement shape functions can be found in related references [Szabó & Babuška 1991]. Substituting Eq.(2.17) into Eq.(2.8), it follows that

$$\boldsymbol{\varepsilon} = \mathbf{L}\mathbf{u} = \mathbf{L}\mathbf{N}(x,y,z)\mathbf{d}^e = \mathbf{B}\mathbf{d}^e \tag{2.18}$$

where

$$\mathbf{B} = \mathbf{L}\mathbf{N}(x,y,z) . \tag{2.19}$$

Substituting Eq.(2.18) into Eq.(2.9) gives

$$\boldsymbol{\sigma} = \mathbf{D}\boldsymbol{\varepsilon} = \mathbf{D}\mathbf{B}\mathbf{d}^e . \tag{2.20}$$

Assuming a small virtual displacement vector $\delta\mathbf{d}^e$ and using Eq.(2.17) and (2.18), it follows that

$$\delta\mathbf{u} = \mathbf{N}\delta\mathbf{d}^e, \quad \delta\boldsymbol{\varepsilon} = \mathbf{B}\delta\mathbf{d}^e . \tag{2.21}$$

Thus, the virtual strain energy δU_e in an element can be written as

$$\delta U_e = \int_\Omega \delta\boldsymbol{\varepsilon}^T \boldsymbol{\sigma} d\Omega . \tag{2.22}$$

And the total virtual work of the body forces, boundary surface forces, inertial forces and damping forces for an element, δW_e, is

$$\delta W_e = \int_\Omega \delta\mathbf{u}^T \mathbf{b} d\Omega + \int_{S_\sigma} \delta\mathbf{u}^T \mathbf{T} dS - \int_\Omega \delta\mathbf{u}^T \rho\ddot{\mathbf{u}} d\Omega - \int_\Omega \delta\mathbf{u}^T \mu\dot{\mathbf{u}} d\Omega . \tag{2.23}$$

Applying the virtual work principle, $\delta U_e = \delta W_e$, to an element gives

$$\int_\Omega \delta\boldsymbol{\varepsilon}^T \boldsymbol{\sigma} d\Omega = \int_\Omega \delta\mathbf{u}^T \mathbf{b} d\Omega + \int_{S_\sigma} \delta\mathbf{u}^T \mathbf{T} dS - \int_\Omega \delta\mathbf{u}^T \rho\ddot{\mathbf{u}} d\Omega - \int_\Omega \delta\mathbf{u}^T \mu\dot{\mathbf{u}} d\Omega . \tag{2.24}$$

This equation is the Galerkin integral form of the dynamic equilibrium equation Eq.(2.6) and the force boundary condition Eq.(2.14). Substituting Eqs.(2.17), (2.20), and (2.21) into Eq.(2.24) and canceling $\delta\mathbf{d}^{e^T}$ from both sides of the equation, we have

$$(\int_\Omega \rho\mathbf{N}^T\mathbf{N}d\Omega)\ddot{\mathbf{d}}^e + (\int_\Omega \mu\mathbf{N}^T\mathbf{N}d\Omega)\dot{\mathbf{d}}^e + (\int_\Omega \mathbf{B}^T\mathbf{D}\mathbf{B}d\Omega)\mathbf{d}^e = \int_\Omega \mathbf{N}^T\mathbf{b}d\Omega + \int_{S_\sigma}\mathbf{N}^T\mathbf{T}dS. \qquad (2.25)$$

Thus,

$$\mathbf{M}^e\ddot{\mathbf{d}}^e + \mathbf{C}^e\dot{\mathbf{d}}^e + \mathbf{K}^e\mathbf{d}^e = \mathbf{F}^e \qquad (2.26)$$

where

$$\mathbf{M}^e = \int_\Omega \rho\mathbf{N}^T\mathbf{N}d\Omega, \quad \mathbf{C}^e = \int_\Omega \mu\mathbf{N}^T\mathbf{N}d\Omega, \quad \mathbf{K}^e = \int_\Omega \mathbf{B}^T\mathbf{D}\mathbf{B}d\Omega \qquad (2.27)$$

are the mass, damping and stiffness matrices of the element, respectively. While

$$\mathbf{F}^e = \int_\Omega \mathbf{N}^T\mathbf{b}dV + \int_{S_\sigma}\mathbf{N}^T\mathbf{T}dS \qquad (2.28)$$

is the element nodal load vector. The element nodal displacement vector $\mathbf{d}^e$ can be expressed using the system nodal displacement vector $\mathbf{X}(t)$ by a transformation matrix $\mathbf{G}^e$ as follows:

$$\mathbf{d}^e = \mathbf{G}^e\mathbf{X}(t) \qquad (2.29)$$

Substituting Eq.(2.29) into Eq.(2.26), premultiplying matrix $\mathbf{G}^T$ and summing them for all elements, we have

$$\sum_e (\mathbf{G}^{eT}\mathbf{M}^e\mathbf{G}^e)\ddot{\mathbf{X}}(t) + \sum_e (\mathbf{G}^{eT}\mathbf{C}^e\mathbf{G}^e)\dot{\mathbf{X}}(t) + \sum_e \mathbf{G}^{eT}\mathbf{K}^e\mathbf{G}^e\mathbf{X}(t) = \sum_e \mathbf{G}^{eT}\mathbf{F}^e \qquad (2.30)$$

where

$$\mathbf{M} = \sum_e \mathbf{G}^{eT}\mathbf{M}^e\mathbf{G}^e, \quad \mathbf{C} = \sum_e \mathbf{G}^{eT}\mathbf{C}^e\mathbf{G}^e, \quad \mathbf{K} = \sum_e \mathbf{G}^{eT}\mathbf{K}^e\mathbf{G}^e \qquad (2.31)$$

are called the mass, damping and stiffness matrices of the system, respectively. While

$$F(t) = \sum_e \mathbf{G}^{eT} \mathbf{F}^e \qquad (2.32)$$

is called the external load vector of the system. Thus the system dynamic equilibrium equation becomes

$$\mathbf{M}\ddot{\mathbf{X}}(t) + \mathbf{C}\dot{\mathbf{X}}(t) + \mathbf{K}\mathbf{X}(t) = \mathbf{F}(t) \qquad (2.33)$$

where

$$\mathbf{M} = \begin{bmatrix} m_{11} & m_{12} & \cdots & m_{1n} \\ m_{21} & m_{22} & \ddots & m_{2n} \\ \vdots & \ddots & \ddots & \vdots \\ m_{n1} & m_{n2} & \cdots & m_{nn} \end{bmatrix}, \mathbf{C} = \begin{bmatrix} c_{11} & c_{12} & \cdots & c_{1n} \\ c_{21} & c_{22} & \ddots & c_{2n} \\ \vdots & \ddots & \ddots & \vdots \\ c_{n1} & c_{n2} & \cdots & c_{nn} \end{bmatrix}, \mathbf{K} = \begin{bmatrix} k_{11} & k_{12} & \cdots & k_{1n} \\ k_{21} & k_{22} & \ddots & k_{2n} \\ \vdots & \ddots & \ddots & \vdots \\ k_{n1} & k_{n2} & \cdots & k_{nn} \end{bmatrix} \qquad (2.34)$$

$$\mathbf{X}(t) = \{x_1(t), x_2(t), \cdots, x_n(t)\}^T \qquad (2.35)$$

$$\mathbf{F}(t) = \{F_1(t), F_2(t), \cdots, F_n(t)\}^T \qquad (2.36)$$

where n represents the total number of degrees of freedom. $\mathbf{M}$, $\mathbf{C}$ and $\mathbf{K}$ are symmetrical matrices. The displacement vector, $\mathbf{X}(t)$, contains terms that include translations in x-, y-, and z-directions, and rotations in θ_x-, θ_y-, and θ_z-directions. The external load vector, $\mathbf{F}(t)$, contains terms that include forces in x-, y-, and z-directions and moments in θ_x-, θ_y-, and θ_z-directions. When the displacement boundary conditions are applied, Eq.(2.33) is reduced by eliminating the constrained displacements and corresponding rows and columns in $\mathbf{M}$, $\mathbf{C}$ and $\mathbf{K}$. For convenience, the reduced degrees of freedom is still donated by n and the reduced system dynamic equilibrium equation is still expressed as Eqs.(2.33)~(2.36). Right now, $\mathbf{M}$, $\mathbf{C}$ and $\mathbf{K}$ are symmetric positive definite matrices.

2.3 Solution Of Structural Dynamic Response

When the dynamic equilibrium equation of the middle ear system is obtained using the basic principles of finite element method, we can solve the system for the structural response. In this section, the modal superposition method is described to solve the displacement response of the system to harmonic loads. The natural frequencies and natural modes are first calculated through the undamped free vibration analysis of the system. Then the displacement response is expressed as the linear combination of the natural modes of the system. The dynamic equilibrium equation is decoupled using Rayleigh damping assumption and the orthogonal properties of natural modes, and then solved numerically.

2.3.1 Undamped Free Vibration

The undamped free vibration is represented by Eq.(2.33) without damping ($C = 0$) and external load ($F = 0$). The result is a matrix equation of motion

$$\mathbf{M}\ddot{\mathbf{X}}(t) + \mathbf{K}\mathbf{X}(t) = \mathbf{0}. \tag{2.37}$$

Assume the solution of Eq.(2.37) as

$$\mathbf{X}(t) = \begin{Bmatrix} x_1(t) \\ x_2(t) \\ \vdots \\ x_n(t) \end{Bmatrix} = \begin{Bmatrix} \bar{a}_1(t) \\ \bar{a}_2(t) \\ \vdots \\ \bar{a}_n(t) \end{Bmatrix} \cos\omega t + \begin{Bmatrix} \bar{b}_1(t) \\ \bar{b}_2(t) \\ \vdots \\ \bar{b}_n(t) \end{Bmatrix} \sin\omega t = \bar{\mathbf{A}}\cos\omega t + \bar{\mathbf{B}}\sin\omega t. \tag{2.38}$$

Substituting Eq.(2.38) into Eq.(2.37) and collecting terms gives

$$[-\mathbf{M}\omega^2 + \mathbf{K}]\bar{\mathbf{A}}\cos\omega t + [-\mathbf{M}\omega^2 + \mathbf{K}]\bar{\mathbf{B}}\sin\omega t = \mathbf{0}. \tag{2.39}$$

Since $\sin\omega t$ and $\cos\omega t$ cannot be zero at the same time, therefore

23

$$[-M\omega^2 + K]\overline{A} = 0, \quad [-M\omega^2 + K]\overline{B} = 0. \tag{2.40}$$

The non-trivial solution of Eq.(2.40) can be obtained by setting the determinant of the matrix $[-M\omega^2 + K]$ to zero, i.e.,

$$\left| -M\omega^2 + K \right| = 0. \tag{2.41}$$

Equation (2.41) is an nth-order polynomial, and therefore there are n unknown ω^2. Since both M and K are symmetric positive definite matrices, there will always be n real solutions of ω^2, denoted as $\omega_1^2, \omega_2^2, \cdots, \omega_n^2$, which satisfy

$$\omega_1^2 \le \omega_2^2 \le \cdots \le \omega_n^2. \tag{2.42}$$

The smallest value of ω_i (i.e., ω_1) is referred to as the fundamental natural frequency of vibration, the second smallest value of ω_i (i.e., ω_2) is called the second natural frequency of vibration, and so forth. The quantity of ω_i^2 is called the ith eigenvalue of the system. Each natural frequency of the system has a corresponding eigenvector, denoted as φ_i. And ω_i and φ_i are related by the equation

$$[-M\omega_i^2 + K]\varphi_i = 0. \tag{2.43}$$

The eigenvectors are called natural modes of the system, which take the form

$$\varphi_i = \{\varphi_{1i}, \varphi_{2i}, \cdots, \varphi_{ni}\}^T. \tag{2.44}$$

The n solutions of ω previously computed show that the response of the structure can be represented as the combinations of n natural modes. Therefore,

$$X(t) = \sum_{i=1}^{n} [\overline{A}_i \cos\omega_i t + \overline{B}_i \sin\omega_i t]. \tag{2.45}$$

When Eq.(2.45) is substituted into Eq.(2.37), it follows that

$$\sum_{i=1}^{n} [-\mathbf{M}\omega_i^2 + \mathbf{K}][\overline{\mathbf{A}}_i \cos\omega_i t + \overline{\mathbf{B}}_i \sin\omega_i t] = 0.$$ (2.46)

Therefore, to obtain a nontrivial solution, it must follow that

$$[-\mathbf{M}\omega_i^2 + \mathbf{K}]\overline{\mathbf{A}}_i = 0, \quad [-\mathbf{M}\omega_i^2 + \mathbf{K}]\overline{\mathbf{B}}_i = 0.$$ (2.47)

Comparing Eq.(2.43) with Eq.(2.47) gives

$$\overline{\mathbf{A}}_i = a_i\varphi_i, \quad \overline{\mathbf{B}}_i = b_i\varphi_i.$$ (2.48)

It follows from Eq.(2.45) that

$$\mathbf{X}(t) = \sum_{i=1}^{n} \varphi_i[a_i \cos\omega_i t + b_i \sin\omega_i t] = \sum_{i=1}^{n} \varphi_i q_i(t)$$ (2.49)

where

$$q_i(t) = a_i \cos\omega_i t + b_i \sin\omega_i t.$$ (2.50)

This is the solution of the undamped free vibration. The values of a_i and b_i can be determined based on the given initial conditions.

2.3.2 Orthogonality Of Natural Modes

Since the orthogonal properties of natural modes are the prerequisite for decoupling the dynamic equilibrium equations, we discuss them in detail in this section. Natural frequencies of vibration, $\omega_1^2, \omega_2^2, \cdots, \omega_n^2$, and the natural modes, $\varphi_1, \varphi_2, \cdots, \varphi_n$, satisfy the eigenvalue equation. The norm (or length) of any natural mode is defined as

$$\|\varphi_i\| = \sqrt{(\varphi_{1i})^2 + (\varphi_{2i})^2 + \cdots + (\varphi_{ni})^2}.$$ (2.51)

Because each natural mode has an arbitrary scaling factor, they can always be normalized with the norm equal to 1. This type of normalization of natural modes is called norm

normalization. Denoting the normalized natural modes as $\hat{\varphi}_1, \hat{\varphi}_2, \cdots, \hat{\varphi}_n$, it then follows that

$$\hat{\varphi}_i = \left\{ \frac{\varphi_{1i}}{\|\varphi_i\|}, \frac{\varphi_{2i}}{\|\varphi_i\|}, \cdots, \frac{\varphi_{ni}}{\|\varphi_i\|} \right\}^{\mathrm{T}} = \{\hat{\varphi}_{1i}, \hat{\varphi}_{2i}, \cdots, \hat{\varphi}_{ni}\}^{\mathrm{T}}. \tag{2.52}$$

The advantage of the norm normalized natural modes is that the sizes of the elements in the natural modes do not become large and thus do not result in numerical ill-conditioning when used in other matrix equations. If Eq.(2.43) is divided by the norm of the natural mode φ_i, then it follows that

$$\frac{1}{\|\varphi_i\|}[-\mathbf{M}\omega_i^2 + \mathbf{K}]\varphi_i = [-\mathbf{M}\omega_i^2 + \mathbf{K}]\hat{\varphi}_i = \mathbf{0}. \tag{2.53}$$

Consider the natural frequencies of vibration, ω_i and ω_j, and their corresponding natural modes, $\hat{\varphi}_i$ and $\hat{\varphi}_j$. Equation (2.53) can be written for each natural frequency, and it follows that

$$[-\mathbf{M}\omega_i^2 + \mathbf{K}]\hat{\varphi}_i = \mathbf{0} \tag{2.54a}$$

$$[-\mathbf{M}\omega_j^2 + \mathbf{K}]\hat{\varphi}_j = \mathbf{0}. \tag{2.54b}$$

Premultiplying Eq.(2.54a) by $\hat{\varphi}_j^{\mathrm{T}}$, Eq.(2.54b) by $\hat{\varphi}_i^{\mathrm{T}}$ gives

$$\hat{\varphi}_j^{\mathrm{T}}[-\mathbf{M}\omega_i^2 + \mathbf{K}]\hat{\varphi}_i = \mathbf{0} \tag{2.55a}$$

$$\hat{\varphi}_i^{\mathrm{T}}[-\mathbf{M}\omega_j^2 + \mathbf{K}]\hat{\varphi}_j = \mathbf{0}. \tag{2.55b}$$

Since both $\mathbf{M}$ and $\mathbf{K}$ are symmetrical matrices, it follows that

$$\hat{\varphi}_j^{\mathrm{T}}\mathbf{M}\hat{\varphi}_i = \hat{\varphi}_i^{\mathrm{T}}\mathbf{M}\hat{\varphi}_j, \quad \hat{\varphi}_j^{\mathrm{T}}\mathbf{K}\hat{\varphi}_i = \hat{\varphi}_i^{\mathrm{T}}\mathbf{K}\hat{\varphi}_j. \tag{2.56}$$

Substracting Eq.(2.55b) from Eq.(2.55a) and using the property of the mass matrix $\mathbf{M}$ and stiffness matrix $\mathbf{K}$ in Eq.(2.56), it follows that

$$\hat{\varphi}_j^T \mathbf{M} \hat{\varphi}_i (\omega_i^2 - \omega_j^2) = 0. \tag{2.57}$$

For any $\omega_i \neq \omega_j$, it follows that $\hat{\varphi}_j^T \mathbf{M} \hat{\varphi}_i = 0$. This is known as the orthogonal property of two natural modes with respect to the mass matrix $\mathbf{M}$. A similar orthogonal property of two natural modes with respect to the stiffness matrix $\mathbf{K}$ can also be derived from Eq.(2.55). It states that $\hat{\varphi}_i^T \mathbf{K} \hat{\varphi}_i = 0$ for any $\omega_i \neq \omega_j$. In summary, the orthogonal property for the system mass and stiffness matrices states that

$$\hat{\varphi}_j^T \mathbf{M} \hat{\varphi}_i = \hat{\varphi}_i^T \mathbf{M} \hat{\varphi}_i = \begin{cases} \hat{m}_i & i = j \\ 0 & i \neq j, \end{cases} \quad \hat{\varphi}_j^T \mathbf{K} \hat{\varphi}_i = \hat{\varphi}_i^T \mathbf{K} \hat{\varphi}_i = \begin{cases} \hat{k}_i & i = j \\ 0 & i \neq j. \end{cases} \tag{2.58}$$

Define the modal matrix of norm normalized natural modes to be

$$\hat{\mathbf{\Phi}} = [\hat{\varphi}_1, \hat{\varphi}_2, \cdots, \hat{\varphi}_n] = \begin{bmatrix} \hat{\varphi}_{11} & \hat{\varphi}_{12} & \cdots & \hat{\varphi}_{1n} \\ \hat{\varphi}_{21} & \hat{\varphi}_{22} & \ddots & \hat{\varphi}_{2n} \\ \vdots & \ddots & \ddots & \vdots \\ \hat{\varphi}_{n1} & \hat{\varphi}_{n2} & \cdots & \hat{\varphi}_{nn} \end{bmatrix} \tag{2.59}$$

and it follows that

$$\hat{\mathbf{M}} = \hat{\mathbf{\Phi}}^T \mathbf{M} \hat{\mathbf{\Phi}} = \begin{bmatrix} \hat{m}_1 & 0 & \cdots & 0 \\ 0 & \hat{m}_2 & \ddots & 0 \\ \vdots & \ddots & \ddots & \vdots \\ 0 & 0 & \cdots & \hat{m}_n \end{bmatrix}, \quad \hat{\mathbf{K}} = \hat{\mathbf{\Phi}}^T \mathbf{K} \hat{\mathbf{\Phi}} = \begin{bmatrix} \hat{k}_1 & 0 & \cdots & 0 \\ 0 & \hat{k}_2 & \ddots & 0 \\ \vdots & \ddots & \ddots & \vdots \\ 0 & 0 & \cdots & \hat{k}_n \end{bmatrix}. \tag{2.60}$$

Note that these relationships exist for any normalization of the natural modes although the orthogonal relationships were derived using the norm normalized natural modes.

2.3.3 Damped Response

Having the discussions in Sections 2.3.1 and 2.3.2, we can solve the middle ear system for the structural response. Using the modal superposition method, the structural response is expressed as a linear combination of its natural modes

$$\mathbf{X}(t) = \hat{\boldsymbol{\varphi}}_1 q_1(t) + \hat{\boldsymbol{\varphi}}_2 q_2(t) + \cdots + \hat{\boldsymbol{\varphi}}_n q_n(t) = \hat{\boldsymbol{\Phi}}\mathbf{Q}(t) \tag{2.61}$$

where $q_1(t), q_2(t), \cdots, q_n(t)$ are called the generalized coordinates and

$$\mathbf{Q}(t) = \{q_1(t), q_2(t), \cdots, q_n(t)\}^{\mathrm{T}} \tag{2.62}$$

is called the generalized coordinate vector. For a large system, it may not be feasible to calculate all the natural frequencies and natural modes. Consider the first k natural frequencies and natural modes, where $k \le n$, then Eq.(2.61) becomes

$$\mathbf{X}(t) = \hat{\boldsymbol{\varphi}}_1 q_1(t) + \hat{\boldsymbol{\varphi}}_2 q_2(t) + \cdots + \hat{\boldsymbol{\varphi}}_k q_k(t) = \hat{\boldsymbol{\Phi}}\mathbf{Q}(t) \tag{2.63}$$

where

$$\hat{\boldsymbol{\Phi}} = [\hat{\boldsymbol{\varphi}}_1, \hat{\boldsymbol{\varphi}}_2, \cdots, \hat{\boldsymbol{\varphi}}_k] = \begin{bmatrix} \hat{\varphi}_{11} & \hat{\varphi}_{12} & \cdots & \hat{\varphi}_{1k} \\ \hat{\varphi}_{21} & \hat{\varphi}_{22} & \ddots & \hat{\varphi}_{2k} \\ \vdots & \ddots & \ddots & \vdots \\ \hat{\varphi}_{n1} & \hat{\varphi}_{n2} & \cdots & \hat{\varphi}_{nk} \end{bmatrix}, \quad \mathbf{Q}(t) = \begin{Bmatrix} q_1(t) \\ q_2(t) \\ \vdots \\ q_k(t) \end{Bmatrix}. \tag{2.64}$$

Note that $\hat{\boldsymbol{\Phi}}$ is a $n \times k$ matrix that is not a square matrix. Substituting Eq.(2.63) into the dynamic equilibrium equation, Eq.(2.33), it follows that

$$\mathbf{M}\hat{\boldsymbol{\Phi}}\ddot{\mathbf{Q}}(t) + \mathbf{C}\hat{\boldsymbol{\Phi}}\dot{\mathbf{Q}}(t) + \mathbf{K}\hat{\boldsymbol{\Phi}}\mathbf{Q}(t) = \mathbf{F}(t). \tag{2.65}$$

Premultiplying Eq.(2.65) by $\hat{\boldsymbol{\Phi}}^{\mathrm{T}}$ gives

$$\hat{\boldsymbol{\Phi}}^{\mathrm{T}}\mathbf{M}\hat{\boldsymbol{\Phi}}\ddot{\mathbf{Q}}(t) + \hat{\boldsymbol{\Phi}}^{\mathrm{T}}\mathbf{C}\hat{\boldsymbol{\Phi}}\dot{\mathbf{Q}}(t) + \hat{\boldsymbol{\Phi}}^{\mathrm{T}}\mathbf{K}\hat{\boldsymbol{\Phi}}\mathbf{Q}(t) = \hat{\boldsymbol{\Phi}}^{\mathrm{T}}\mathbf{F}(t). \tag{2.66}$$

Using Rayleigh proportional damping, the damping matrix $\mathbf{C}$ is a linear combination of the mass and the stiffness matrices:

$$C = \alpha M + \beta K . \tag{2.67}$$

where α and β are the damping parameters and their units are s^{-1} (second^{-1}) and s (second), respectively. Because the natural modes are orthogonal to the mass and stiffness matrices, the modes will be orthogonal to the damping matrix. Therefore, it follows that

$$\hat{\Phi}^T M \hat{\Phi} = \begin{bmatrix} \hat{\varphi}_1^T \\ \hat{\varphi}_2^T \\ \vdots \\ \hat{\varphi}_k^T \end{bmatrix} \begin{bmatrix} m_{11} & m_{12} & \cdots & m_{1n} \\ m_{21} & m_{22} & \ddots & m_{2n} \\ \vdots & \ddots & \ddots & \vdots \\ m_{n1} & m_{n2} & \cdots & m_{nn} \end{bmatrix} [\hat{\varphi}_1, \hat{\varphi}_2, \cdots, \hat{\varphi}_k] = \begin{bmatrix} \hat{m}_1 & 0 & \cdots & 0 \\ 0 & \hat{m}_2 & \ddots & 0 \\ \vdots & \ddots & \ddots & \vdots \\ 0 & 0 & \cdots & \hat{m}_k \end{bmatrix} = \hat{M} \tag{2.68a}$$

$$\hat{\Phi}^T K \hat{\Phi} = \begin{bmatrix} \hat{\varphi}_1^T \\ \hat{\varphi}_2^T \\ \vdots \\ \hat{\varphi}_k^T \end{bmatrix} \begin{bmatrix} k_{11} & k_{12} & \cdots & k_{1n} \\ k_{21} & k_{22} & \ddots & k_{2n} \\ \vdots & \ddots & \ddots & \vdots \\ k_{n1} & k_{n2} & \cdots & k_{nn} \end{bmatrix} [\hat{\varphi}_1, \hat{\varphi}_2, \cdots, \hat{\varphi}_k] = \begin{bmatrix} \hat{k}_1 & 0 & \cdots & 0 \\ 0 & \hat{k}_2 & \ddots & 0 \\ \vdots & \ddots & \ddots & \vdots \\ 0 & 0 & \cdots & \hat{k}_k \end{bmatrix} = \hat{K} \tag{2.68b}$$

$$\hat{\Phi}^T C \hat{\Phi} = \hat{\Phi}^T (\alpha M + \beta K) \hat{\Phi} = \alpha \hat{\Phi}^T M \hat{\Phi} + \beta \hat{\Phi}^T K \hat{\Phi}$$

$$= \begin{bmatrix} \alpha \hat{m}_1 + \beta \hat{k}_1 & 0 & \cdots & 0 \\ 0 & \alpha \hat{m}_2 + \beta \hat{k}_2 & \ddots & 0 \\ \vdots & \ddots & \ddots & \vdots \\ 0 & 0 & \cdots & \alpha \hat{m}_k + \beta \hat{k}_k \end{bmatrix} = \begin{bmatrix} \hat{c}_1 & 0 & \cdots & 0 \\ 0 & \hat{c}_2 & \ddots & 0 \\ \vdots & \ddots & \ddots & \vdots \\ 0 & 0 & \cdots & \hat{c}_k \end{bmatrix} = \hat{C} \tag{2.68c}$$

Substituting Eq.(2.68) into Eq.(2.66) gives

$$\hat{M}\ddot{Q}(t) + \hat{C}\dot{Q}(t) + \hat{K}Q(t) = \hat{\Phi}^T F(t) . \tag{2.69}$$

Equation (2.69) represents k uncoupled equations, each of which takes the form

$$\hat{m}_i \ddot{q}_i(t) + \hat{c}_i \dot{q}_i(t) + \hat{k}_i q_i(t) = \hat{\varphi}_i^T F(t) \tag{2.70}$$

or alternatively

$$\ddot{q}_i(t) + 2\zeta_i \omega_i \dot{q}_i(t) + \omega_i^2 q_i(t) = \hat{\varphi}_i^T F(t) / \hat{m}_i \tag{2.71}$$

where ω_i is the ith natural frequency and ζ_i is called i^{th} modal damping. They are defined as

$$\omega_i^2 = \hat{k}_i / \hat{m}_i, \quad 2\zeta_i \omega_i = \hat{c}_i / \hat{m}_i \qquad (2.72)$$

When the external load vector $\mathbf{F}(t)$ in Eqs.(2.33) and (2.71) is sinusoidal loads with frequency p as

$$\mathbf{F}(t) = \mathbf{F}_0 \sin pt, \qquad (2.73)$$

the oscillating motion forced by this type of loads is called harmonic response or frequency response. The ith uncoupled dynamic equilibrium equation becomes

$$\ddot{q}_i(t) + 2\zeta_i \omega_i \dot{q}_i(t) + \omega_i^2 q_i(t) = f_{0i} \sin pt / \hat{m}_i \qquad (2.74)$$

where

$$f_{0i} = \hat{\boldsymbol{\varphi}}_i^T \mathbf{F}_0 \qquad (2.75)$$

The particular solution (steady response) takes the form

$$q_i(t) = A_1 \cos pt + A_2 \sin pt \qquad (2.76)$$

Substituting Eq.(2.76) into Eq.(2.74) gives

$$-p^2(A_1 \cos pt + A_2 \sin pt) + 2\zeta_i \omega_i p(-A_1 \sin pt + A_2 \cos pt)$$
$$+ \omega_i^2(A_1 \cos pt + A_2 \sin pt) = f_{0i} \sin pt / \hat{m}_i \qquad (2.77)$$

Collecting the cosine terms into one equation and the sine terms into another equation gives the two simultaneous equations for A_1 and A_2. These equations are

$$-p^2 A_1 + 2\zeta_i \omega_i p A_2 + \omega_i^2 A_1 = 0 \qquad (2.78a)$$

$$-p^2 A_2 - 2\zeta_i \omega_i p A_1 + \omega_i^2 A_2 = f_{0i} / \hat{m}_i. \qquad (2.78b)$$

Let $r_i = p / \omega_i$, which is the ratio of the forcing frequency to the ith natural frequency of the system. Solving Eq.(2.78) gives

$$A_1 = -\frac{f_{0i}}{\hat{k}_i}\left(\frac{2\zeta_i r_i}{(1-r_i^2)^2 + (2\zeta_i r_i)^2}\right), \quad A_2 = \frac{f_{0i}}{\hat{k}_i}\left(\frac{1-r_i^2}{(1-r_i^2)^2 + (2\zeta_i r_i)^2}\right). \tag{2.79}$$

It follows from Eq.(2.76) that

$$q_i(t) = \frac{f_{0i}/\hat{k}_i}{(1-r_i^2)^2 + (2\zeta_i r_i)^2}\left(-2\zeta_i r_i \cos pt + (1-r_i^2)\sin pt\right). \tag{2.80}$$

Substituting Eq.(2.80) into Eq.(2.63) gives

$$\mathbf{X}(t) = \sum_{i=1}^{k}\hat{\varphi}_i q_i(t) = \sum_{i=1}^{k}\frac{f_{0i}/\hat{k}_i}{(1-r_i^2)^2 + (2\zeta_i r_i)^2}\left(-2\zeta_i r_i \cos pt + (1-r_i^2)\sin pt\right)\hat{\varphi}_i. \tag{2.81}$$

This solution is the displacement response of the system to harmonic exciting loads.

2.4 Damping Parameters

Damping is an important dynamic characteristic of structures. It is also an important parameter for biological systems. However, the damping effect is hard to determine because the damping factor μ of a material is hard to evaluate. In engineering, the damping effect of a material is considered by assuming certain damping parameters such as Rayleigh damping parameters, α and β. These parameters are converted to the modal damping ζ_i that appears in Eq.(2.81). When Rayleigh damping is used, the values of α and β can be determined by assuming first two modal dampings. Then the modal damping ζ_i for i^{th} modes can be obtained by the following equation

$$\zeta_i = \frac{\alpha + \beta\omega_i^2}{2\omega_i} \tag{2.82}$$

Although the Rayleigh damping parameters were assumed for the whole system in the above discussion, they also can be assumed for any subsystem to deal with different materials used in the system. Of course, the damping factor μ can be directly used for the mass-spring-damper system. Some commercial finite element analysis codes such as ANSYS employ the similar damping expressions.

2.5 Element Types Employed In The Research

To build the finite element model of human middle ear, four types of elements were employed. The section provides the descriptions of ANSYS element types used in the finite element model.

2.5.1 COMBIN14 Spring-Damper Element

COMBIN14, as illustrated in Figure 2.2, is the spring-damper element that has longitudinal displacement in one, two or three dimensions. The element is a uniaxial tension-compression element with two nodes I and J, each having up to three degrees of freedom: translations in the nodal x-, y-, z-directions. No bending or torsion load are considered. It is massless. In Figure 2.2, k and μ are the spring constant and the damping coefficient of the damper, respectively. F, d_I and d_J are the axial force and displacement at points I and J, and have a relation of $F = -k\left|d_I - d_J\right| - \mu\left|\dot{d}_I - \dot{d}_J\right|$. COMBIN14 was employed to model the stapedius annular ligament and the cochlear impedance.
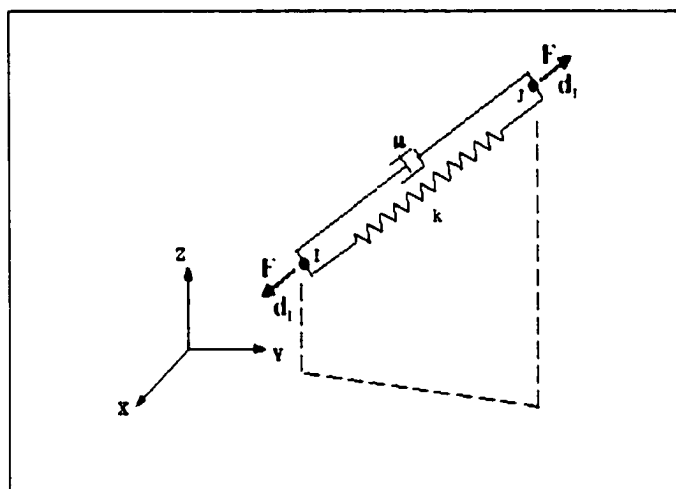
Figure 2.2 COMBIN14 spring-damper

2.5.2 SHELL41 Membrane Shell Element

SHELL41, illustrated in Figure 2.3, has membrane (in-plane) stiffness but no bending (out-of-plane) stiffness. Only normal loads are permitted. The element is defined by four nodes, *I, J, K* and *L*, each having three degrees of freedom: translations in the nodal x-, y-, z-directions. The element can be the quadrilateral element or triangular element. The circled numbers in Figure 2.3 represent the surface identification. SHELL41 was employed to model the eardrum, which will be presented in Chapter 3.
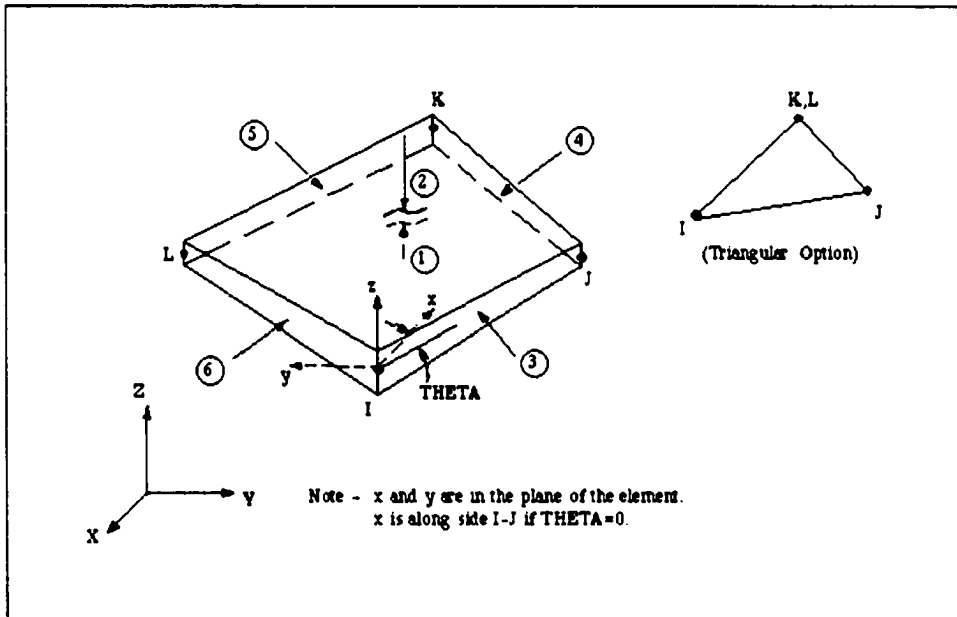
Figure 2.3 SHELL41 membrane shell

2.5.3 SOLID45 3D Structural Solid Element

SOLID45, illustrated in Figure 2.4, is used for the three dimensional modeling of solid structures. The element is defined by eight nodes, *I, J, K, L, M, N, O* and *P*, each having three degrees of freedom: translations in the nodal x-, y-, z-directions. The

element can be the hexahedral (brick element), pentahedral (prism element) or tetrahedral. The circled numbers in Figure 2.4 are the surface identification numbers. The element type was employed to model the ossicles, ligaments and muscles.
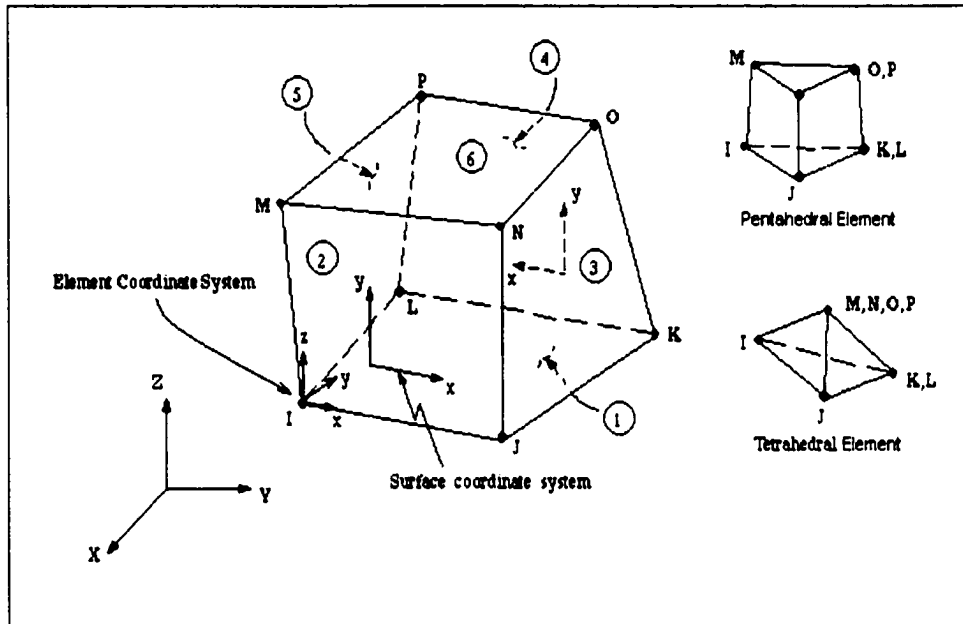
Figure 2.4 SOLID45 3D structural solid

2.5.4 SHELL63 Elastic Shell Element

SHELL63, illustrated in Figure 2.5, has both bending and membrane capabilities. Both in-plane and normal loads are permitted. The element is defined by four nodes, I, J, K and L, each having six degrees of freedom: translations in the nodal x-, y-, z-directions and rotations about the nodal x-, y-, z-axes. The element can be the quadrilateral element or triangular element. The circled numbers in Figure 2.5 represent the surface identification. The element was employed to model the eardrum, which will be discussed in chapter 5.

35
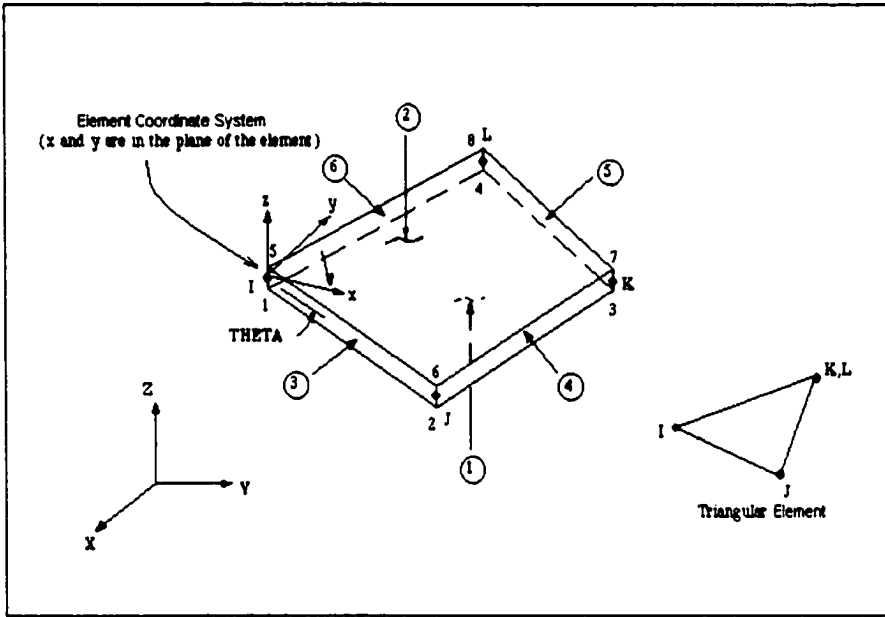
Figure 2.5 SHELL63 elastic shell

CHAPTER THREE

PRELIMINARY STUDY OF HUMAN MIDDLE EAR

MECHANICS

Before developing the computer integrated modeling and simulating method, a simple FE model was created to provide a quick look of the behaviors of the middle ear. In addition, the simple model provides the FE modeling experience for creating the next more accurate model by using serial histological sections of a human temporal bone. This simple model provides:

(1) Preliminary understanding on the anatomy and functions of human middle ear;

(2) Valuable FE modeling experiences that can be used to build a more accurate FE model;

(3) Thorough investigation about the physiological ranges of mechanical properties of the human middle ear;

(4) Initial observations about the effects of the physical parameters and boundary conditions on middle ear mechanics.

3.1 Structures And Functions Of Human Ear

A human ear is divided into three sections: the outer ear, the middle ear and the inner ear, as shown in Figure 3.1.

The outer ear consists of the external pinna (auricle) and auditory meatus (ear canal), which is terminated by the tympanic membrane (eardrum). The pinna helps to collect sound and determine the direction of sound sources of high frequency. The ear canal acts as a pipe resonator that boosts hearing sensitivity in the range of 2,000 to 5,000 Hz.
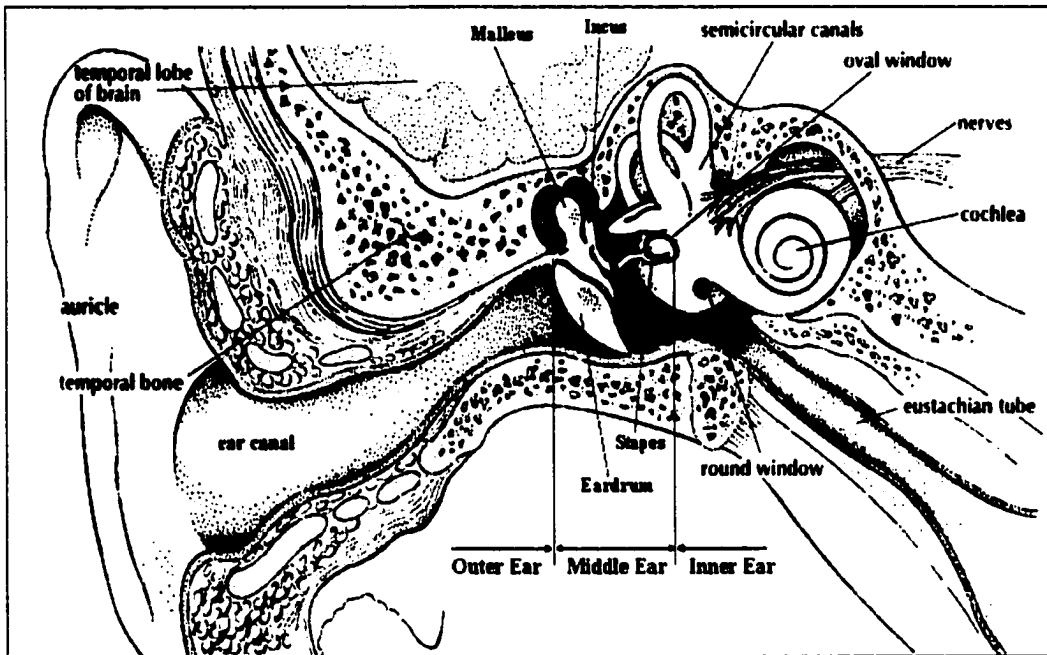
Figure 3.1 A schematic diagram of human ear

The middle ear lies in a cavity of complex form in the outer, mastoid portion of the temporal bone. The cavity is filled with air and connects the middle ear to the pharynx through the Eustachian tube to provide a means of pressure equalization. The middle ear begins with the eardrum, to which are attached three small bones (ossicles). The eardrum, which is a fiber composite with a cross section consisting of several layers and regions, is kept taut by the tensor tympani muscle. The eardrum ultrastructure study shows the regularity of the radial and circumferential fibers appearing in the pars tensa [Lim 1968 & 1970; Shimada & Lim 1971]. These two sets of fibers represent a majority of the stiff fibers appearing

38

in the eardrum. The main portion of the eardrum (pars tensa) is firmly held in a groove in a bony ring formed by the walls of the ear canal, except in a triangular region (pars flaccida) at the upper border (notch of Rivinus) where this ring is incomplete and the connection is lax. The eardrum changes the pressure variations of incoming sound waves into mechanical vibrations to be transmitted via two distinct mechanisms: "ossicular coupling" and "acoustic coupling" [Peake et al. 1992; Merchant et al. 1997 &1998].

The first ossicle, the malleus, is attached to the eardrum along a radius running from the notch of Rivinus to the center of the eardrum (umbo) by the handle (manubrium) of the malleus. The second ossicle, the incus, extends from the malleus to the third ossicle, the stapes. The stapes has its footplate held firmly in the oval window by the stapedius annular ligament. The three ossicles are joined by means of articulations and suspended in the middle ear cavity by ligaments, muscles and attachment. They are the tensor tympani muscle, the posterior stapedial muscle, the superior, anterior and lateral ligaments of the malleus, the posterior ligament of the incus, and the malleus attachment on the eardrum, as shown in Figure 3.2.

The ossicles play a very important role in the hearing process. They act together as a mechanical transformer to fulfill the "ossicular coupling" of sound transmission from the eardrum to the cochlea. Another function of the ossicles is to protect the inner ear from very loud noise and sudden pressure change. Loud sound triggers two sets of muscles: tensor tympani muscle tightens the eardrum and posterior stapedial muscle pulls the stapes footplate away from the oval window of the inner ear.

The inner ear contains the semicircular canals, the vestibule and the cochlea. Only the cochlea is concerned with hearing. The other parts are the body's horizontal-vertical detectors necessary for balance. The cochlea is filled with liquid (cochlear fluid) and
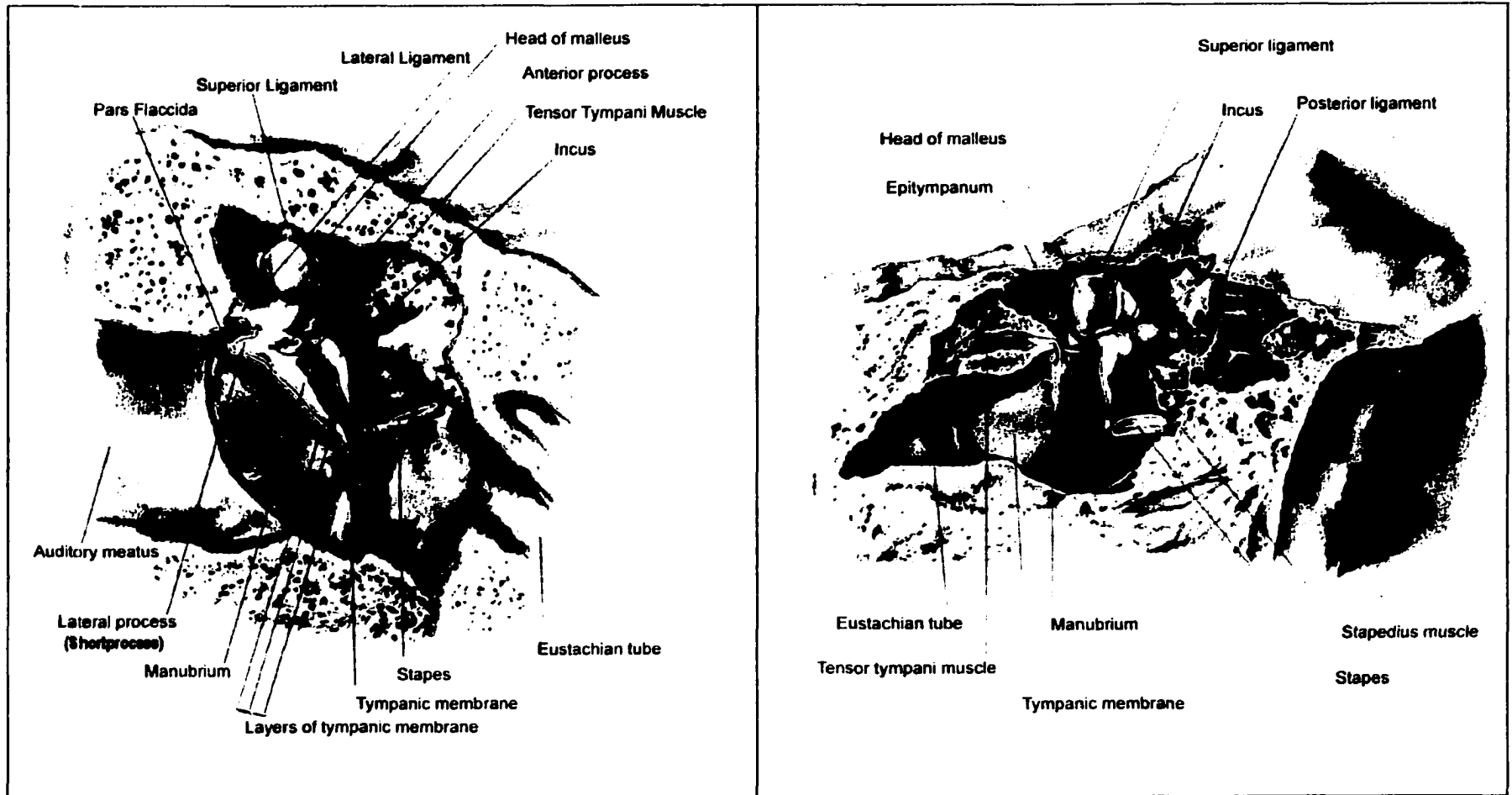
Figure 3.2 The anatomy of human middle ear
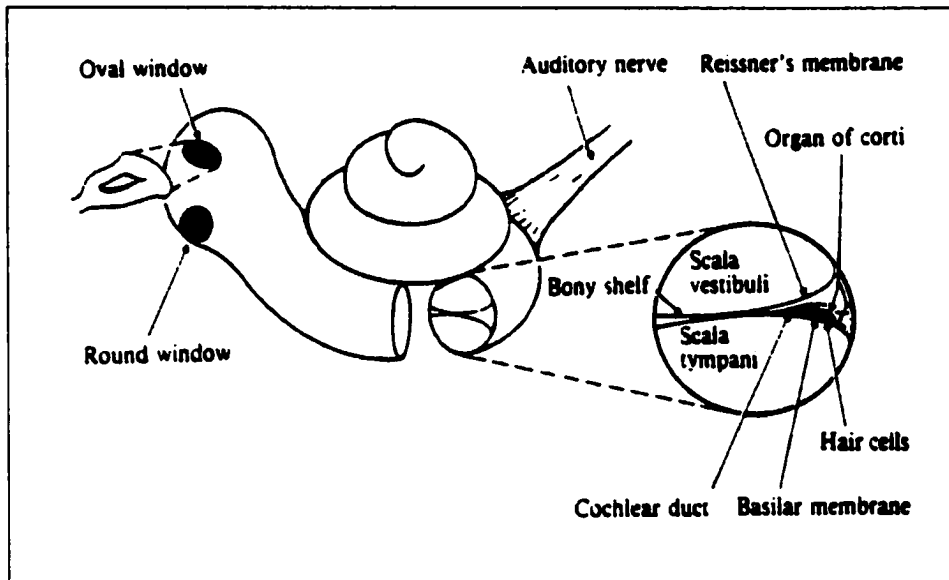
Figure 3.3 Schematic diagram of cochlea

surrounded by rigid bony walls. Its cross-section shows three distinct chambers that run

the entire length: the scala vestibuli, the scala tympani and the cochlear duct, as shown in

Figure 3.3. Resting on the basilar membrane is the delicate and complex organ of corti

that contains several rows of tiny hair cells to which are attached nerve fibers. When the

stapes footplate vibrates against the oval window, hydraulic pressure waves are

transmitted rapidly down the scala vestibuli, inducing ripples in basilar membrane. When

the basilar membrane vibrates, the hairs of the hair cells are bent, thus generating nerve

impulse to the brain. The impulse rate on the auditory nerve depends on both the intensity

and frequency of the sound [Rossing 1990; Wever & Lawrence 1954; Anson & Donaldson 1981].

41

3.2 Sound Pressure Level (SPL)

In Section 3.1, we discussed the anatomy and functions of human ear. In the process of hearing, our ears respond to the sound pressure stimuli of sound waves. In a sound wave, there are extremely small periodic variations in atmospheric pressure to which our ears respond in rather complex manner. The minimum pressure fluctuation to which the ear can respond is less than one billionth of the atmospheric pressure at sea level. This threshold of audibility, which varies from person to person, corresponds to a sound pressure amplitude of about $2 \times 10^{-5} N/m^2$ at a frequency of 1,000 Hz. The threshold of pain corresponds to pressure amplitude approximately one million times greater, but still less than one thousandth of atmospheric pressure. Because of the wide range of pressure stimuli (p), it is convenient to measure sound pressures on a logarithmic scale, called the decibel (dB) scale. Although a decibel scale is actually a means for comparing two sounds, we can define scale of sound level by comparing sounds to a reference sound with standard reference sound pressure $p_0 = 2 \times 10^{-5} N/m^2$. The Sound Pressure Level (SPL), denoted by L_p, is defined as

$$L_p = 20 \log \frac{p}{p_0} \quad (dB\ SPL) \ . \tag{3.1}$$

Thus the conversion formula from SPL to pressure is

$$p = p_0 10^{\frac{L_p}{20}} = 2 \times 10^{-5} \times 10^{\frac{L_p}{20}} \quad (N/m^2) \ . \tag{3.2}$$

42

3.3 A Simple Human Middle Ear FE Model

The construction of the middle ear geometry is the first step to build a three-dimensional finite element model. HyperMesh [Altair Computing Inc.], a commercial FEA pre- and post-processing software, was employed to build the simple model. The model consisted of the eardrum, the ossicular chain, and associated ligaments and muscles. The basic geometric data of the middle ear components and the original authors are listed in Table 3.1. However, most of the data came from Wever & Lawrence's book [Wever & Lawrence 1954].

The key dimensions and characteristics of the entire middle ear system are shown in Figure 3.4 that was drawn by Gan [Gan 1998] based on Wever et al.'s desciptions [Wever & Lawrence 1954; Kirikae 1960; Åwengen et al. 1996; Gulick et al. 1989; Anson & Donaldson 1981].

Table 3.1 Basic anatomic data for human middle ear

EARDRUM	Published Data	Sources
Diameter along manubrium	8.0~10.0 mm	Gray 1918 *
Diameter perpendcular to manubrium	7.5~9.0 mm	Helmholtz 1863 *
Height of Cone	1.54 mm 2.00mm	Wada et al. 1992 Siebenmann 1897 *
Area	55.8~85.0 mm²	Wever & Lawrence 1954, Keith 1918* von Békésy 1941 *
Thickness	0.1 mm 0.04~0.075 mm 0.132 mm	Helmholtz 1863 * Kirikae 1960 Wada et al. 1992
MALLEUS		
Length from end of manubrium to end of lateral process	5.8 mm	Stuhlman 1937 *
Total Length	7.6~9.1 mm	Bast & Anson 1949 *
Weight	23~27 mg	Stuhlman 1937 *, Wever & Lawrence 1954
INCUS		
Length along long process	7.0 mm	Stuhlman 1937 *
Length along short process	5.0 mm	Stuhlman 1937 *
Weight	25~32 mg	Stuhlman 1937 *, Wever & Lawrence 1954
STAPES		
Height	2.5~4.0 mm	Stuhlman 1937 *, Wever & Lawrence 1954
Length of footplate	2.64~3.36 mm 2.5 mm	Wever & Lawrence 1954 Our Measurement
Width of footplate	0.7~1.66 mm	Helmholtz 1863 *, Wever & Lawrence 1954
Weight	2.05~4.35 mg	Wever & Lawrence 1954

* The work was done by the listed authors but the data came from Wever & Lawrence's book [Wever & Lawrence 1954].
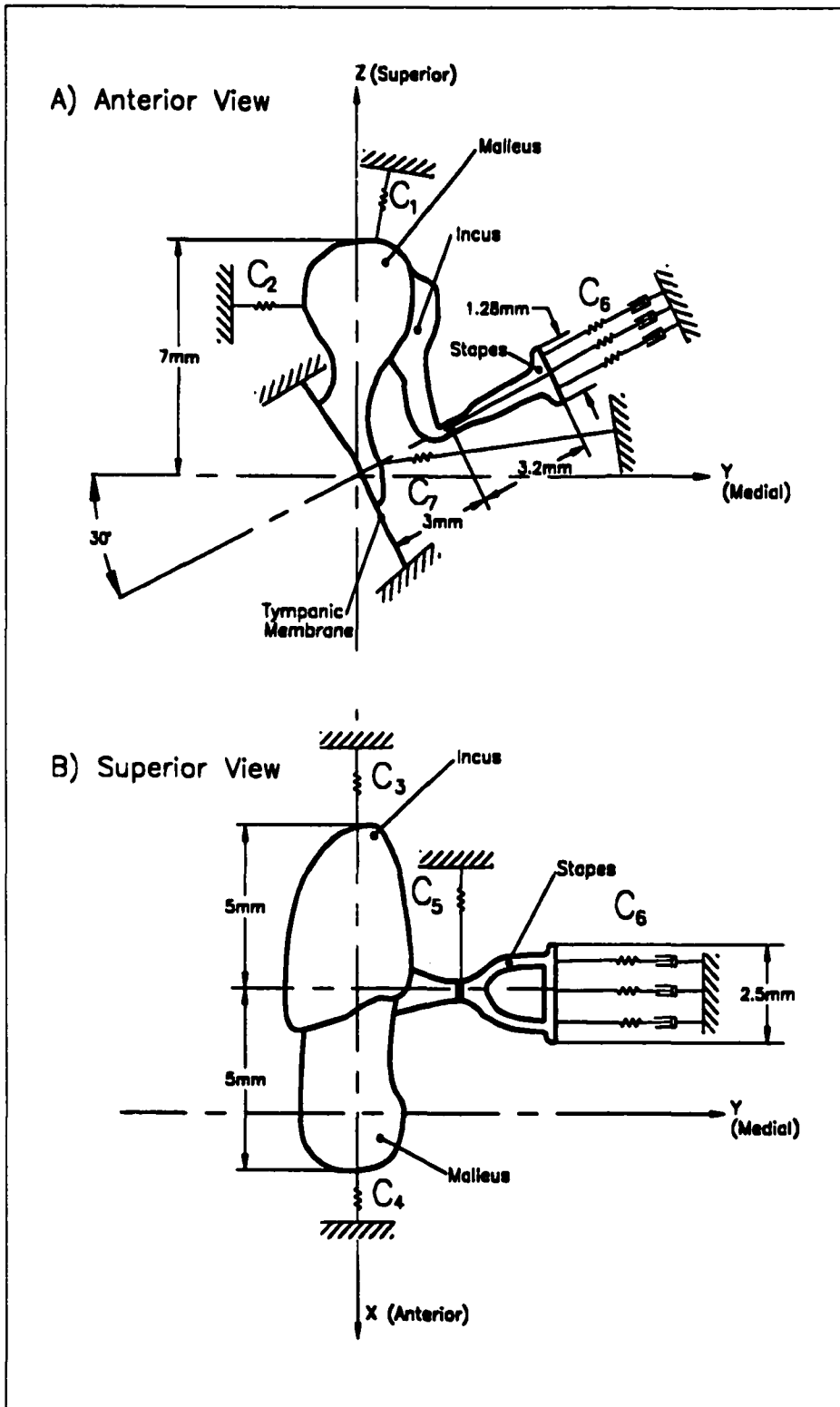
Figure 3.4 Schematic drawing of human middle ear

Eardrum

The eardrum was modeled as an unsymmetrical spatial elliptic conic shell. The geometry was obtained by trimming an elliptic conic surface with a long bottom radius of 5.659 mm, a short bottom radius of 4.523 mm and a height of 2.0 mm using an elliptic cylindrical surface with a long bottom radius of 4.6 mm and a short bottom radius of 4.342 mm. Then the trimmed surface was meshed with 127 triangular and quadrilateral membrane elements with a uniform thickness of 0.132 mm, as shown in Figure 3.5(a).

| (a) Eardrum | (b) Malleus |
| (c) Incus | (d) Stapes |
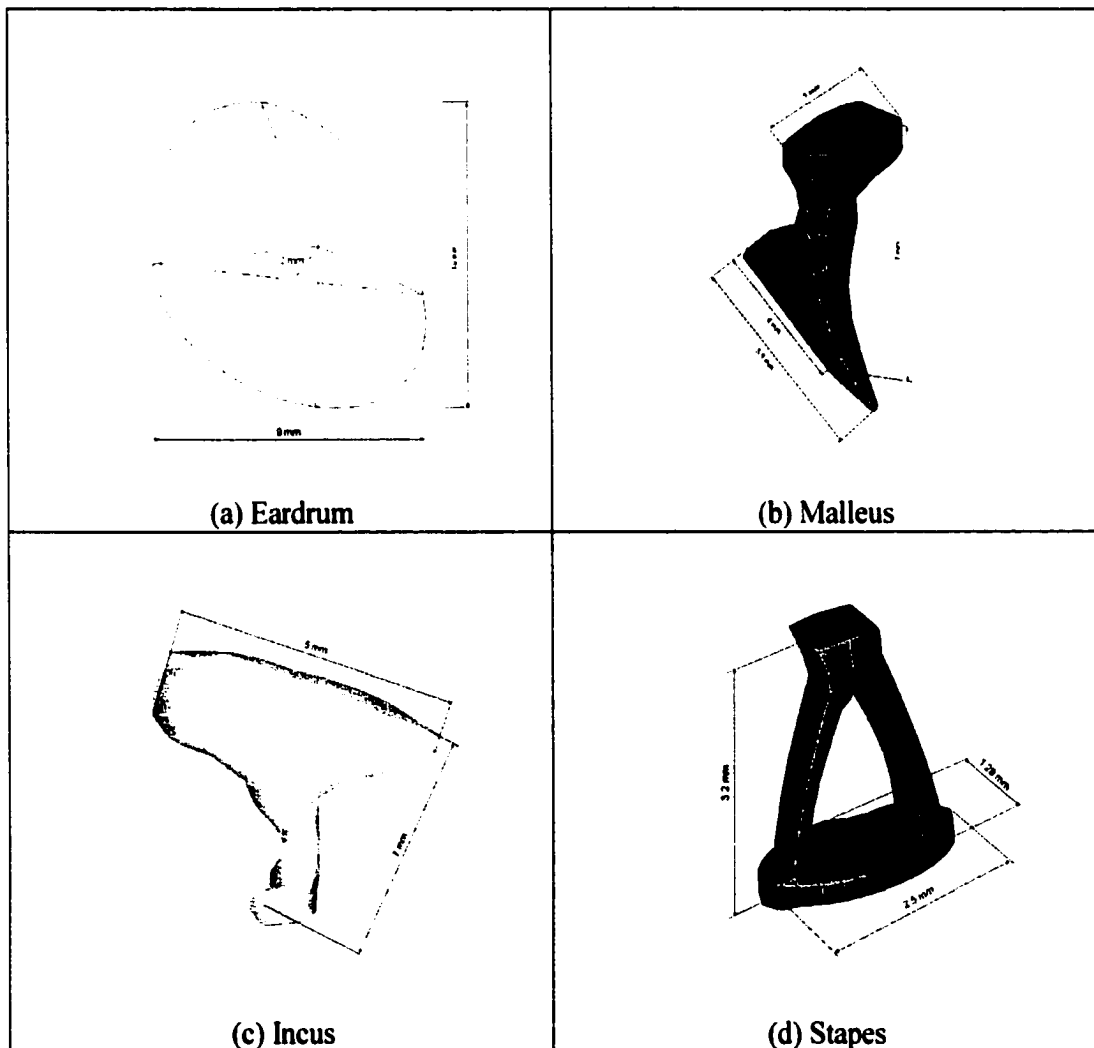
Figure 3.5 Geometric characteristics of the simple model

Ossicles

The characteristic points, lines and surfaces were first created based on the key dimensions of the ossicles listed in Table 3.1 and the relative position of the ossicular chain in space shown in Figure 3.4. Then the FE model was built by directly creating solid elements using these characteristic points, lines and surfaces. The whole ossicular chain consisted of 181 8-node-hexahedral, 6-node-pentahedral, and 4-node-tetrahedral solid elements, as shown in Figure 3.5 (b, c, d).

The dimensions of eardrum, malleus, incus and stapes were defined in four local reference frames. Then each of these component FE models was transformed into the global coordinate system by transforming the corresponding reference frame to global coordinate frame.

Ligaments and Muscles

There are four ligaments and two muscles included in the model, following the drawing shown in Figure 3.4. They are the superior mallear ligament (C1), the lateral mallear ligament (C2), the anterior mallear ligament (C4), the posterior incudal ligament (C3), the posterior stapedial muscle (C5) and the tensor tympani muscle (C7). Each ligament or muscle was modeled as a set of linear springs (COMBIN14 elements) along three orthogonal directions.

Middle Ear FE Model

The middle ear FE model was created by assembling these individual components in global coordinate frame and applying the boundary conditions and loads. The eardrum and the malleus were coupled along the manubrium by coupling their corresponding

nodes. The malleus, incus and stapes are connected at incudomalleolar joint and incudostapedial joint by coupling their corresponding nodes respectively. Each ligament or muscle was attached to the appropriate position of the ossicles at one end and fixed at another end. The tympanic ring was modeled as a set of linear springs (COMBIN14 elements) along three orthogonal directions to simulate the elastic boundary of the eardrum. The impedance of the cochlear fluid (C6) was simplified as three linear springs with dashpots (COMBIN14 elements). Consequently, the ossicles were held on the eardrum by the malleus, and in the oval window by the stapes footplate with resistance provided by a set of linear springs with dashpots. The ossicles were also supported by six sets of linear springs. The eardrum was supported by a set of linear springs. The simple middle ear FE model is shown in Figure 3.6.
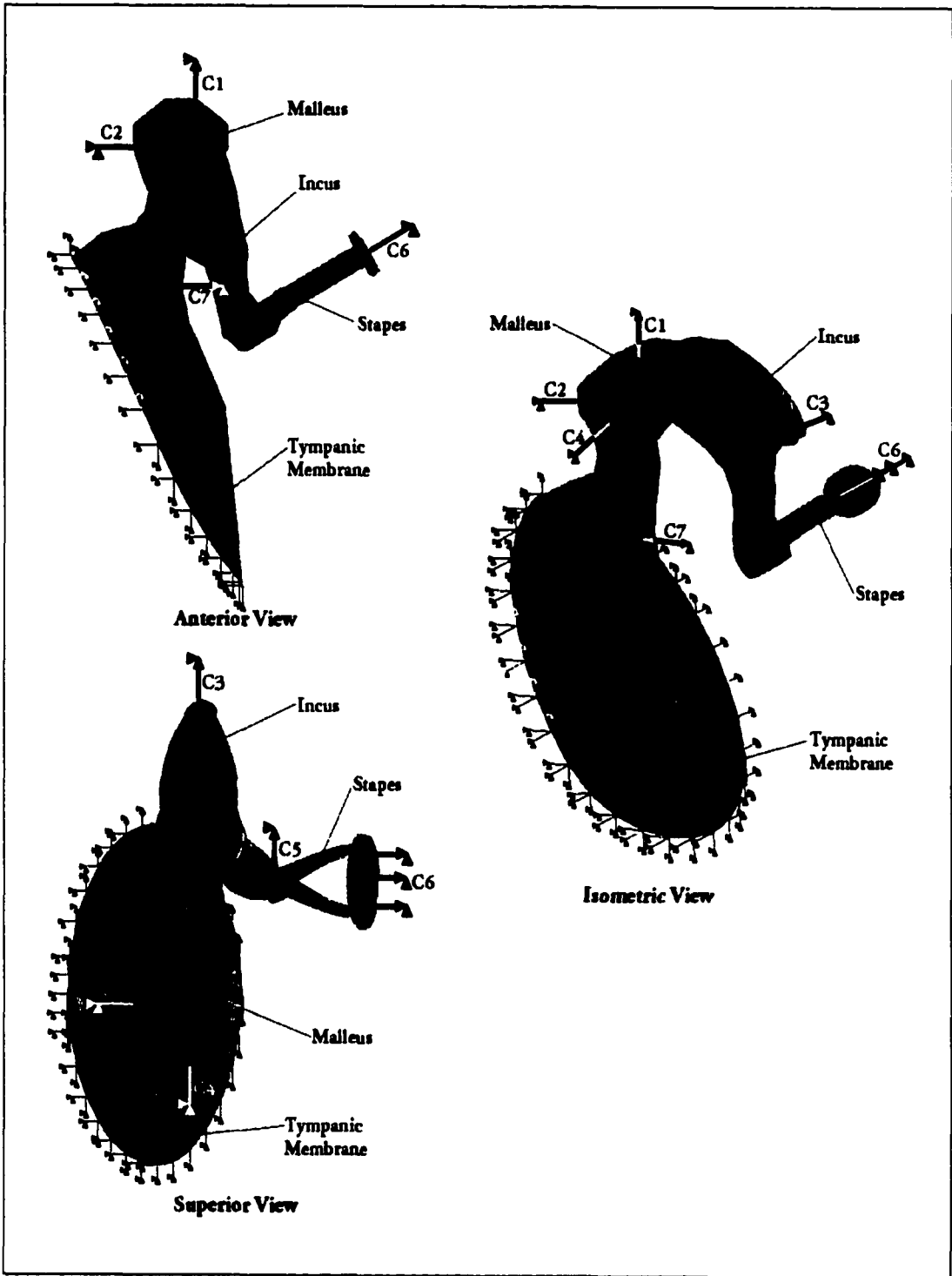
Figure 3.6 A simple finite element model of human right middle ear

3.4 A Review On Mechanical Properties Of The Middle Ear

It is very difficult to determine the mechanical properties of biological materials because either they cannot be isolated for testing or the size of the available specimens is too small to conduct meaningful measurement. Furthermore, it is difficult to keep these specimens in the normal living conditions for measurements [Fung 1996]. Consequently, there are not many experimental data published for mechanical properties of the middle ear. A thorough literature survey was conducted for available mechanical property data of the middle ear. Results of the survey are listed in Table 3.2 and 3.3. Note that the data listed in these tables came partly from experimental measurements, but mostly from estimates. Almost all of the ligament and muscle properties came from estimations. Although the damping coefficients of the middle ear were reported in some papers, big differences existed among the data from different sources. The exception is the damping coefficient of the cochlear fluid, which is 0.620 $N\cdot s/m$ [Wada et al. 1996], 0.624 $N\cdot s/m$ [Koike et al. 1996], 0.717 $N\cdot s/m$ [Ferris et al. 2000] and 0.737 $N\cdot s/m$ [Prendergast et al. 1999]. However, it was at specific frequencies that these values were obtained. Therefore, they cannot be used as a standard to select the damping coefficient of the cochlear fluid. This will be discussed in Chapter 5.

For this simple model, the mechanical properties of the middle ear components were assumed homogeneous and isotropic, and were selected based on those listed in Table 3.2. The densities of malleus, incus and stapes were determined by dividing their corresponding weights obtained from Table 3.2 by their respective volumes obtained from the FE model. It is because the coarse geometry of the FE model caused overlarge volumes of the ossicles so that we had to use the calculated densities to match the weights of the three ossicles. The mechanical properties used for the main components of the

Table 3.2 Published mechanical properties of middle ear components

EARDRUM	Published Data	Sources
Density (kg/m^3)	1.0×10^3 1.2×10^3	Funnell et al. 1983, 1987, 1992 Williams et al. 1990 Wada et al. 1990, 1992, Beer et al. 1996 Ferris et al. 2000.
Young's Modulus (N/m^2) Isotropic	2.0×10^7 2.0×10^7 (pars tensa), 1.0×10^7 (pars flaccida) 3.2×10^7 3.3×10^7 (pars tensa), 1.1×10^7 (pars flaccida) 4.0×10^7 $1.0 \times 10^7 \sim 2.0 \times 10^9$	von Békésy 1949, 1960 Funnell et al. 1978, 1983, 1987, 1992, 1996 Ladak et al. 1996 Wada et al. 1992 Wada et al. 1990, 1996 Kirikae 1960 Williams et al. 1990
Anisotropic	$4.0 \times 10^6 \sim 4.0 \times 10^7$ (circumferential, pars tensa) $2.0 \times 10^7 \sim 4.0 \times 10^7$ (radial, pars tensa) 1.0×10^7 (pars flaccida) 2.0×10^7 (circumferential), 3.2×10^7 (radial)	Prendergast, Ferris et al. 1999 Ferris, Prendergas et al. 2000 Prendergast, Ferris et al. 1999 Ferris, Prendergas et al. 2000 Prendergast, Ferris et al. 1999 Ferris, Prendergas et al. 2000 Beer et al. 1996

MALLEUS		
Density (kg/m^3)	2.55×10^3 (for head) 4.53×10^3 (for neck) 3.70×10^3 (for handle) 2.30×10^3	Kirikae et al. 1960, Wada et al. 1992 Williams et al. 1990
Weight (mg)	23~27	Stuhlman 1937 , Wever et al. 1954
Young's Modulus (N/m^2)	1.00×10^{10} 1.20×10^{10} 1.41×10^{10} 1.483×10^{10} 2.00×10^{10}	Funnell et al. 1978, Williams et al. 1990 Wada et al. 1996 Kirikae et al. 1960, Herrmann et al. 1972 Koike 1996, Wada et al. 1992, 1996 Speirs et al. 1999 Prendergast et al. 1999 Funnell et al. 1992, 1996

INCUS		
Density (kg/m^3)	2.36×10^3 (for body) 2.26×10^3 (for short process) 5.08×10^3 (for long process) 2.30×10^3	Kirikae et al. 1960, Wada et al. 1992 Williams et al. 1990
Weight (mg)	25~32	Stuhlman 1937 , Wever et al. 1954
Young's Modulus (N/m^2)	1.00×10^{10} 1.20×10^{10} 1.41×10^{10} 2.00×10^{10}	Funnell et al. 1978, Williams et al. 1990 Wada et al. 1996 Kirikae et al. 1960, Herrmann et al. 1972 Koike 1996, Wada et al. 1992, 1996 Speirs et al. 1999 Prendergast et al. 1999 Funnell et al. 1992, 1996

STAPES		
Density (kg/m^3)	2.20×10^3 2.30×10^3	Kirikae 1960 Williams et al. 1990
Weight (mg)	2.05~4.35	Wever et al. 1954
Young' Modulus (N/m^2)	1.00×10^{10} 1.20×10^{10} 1.41×10^{10} 2.00×10^{10}	Funnell et al. 1978, Williams et al. 1990 Wada et al. 1996 Kirikae et al. 1960, Herrmann et al. 1972 Koike 1996, Wada et al. 1992, 1996 Prendergast et al. 1999 Funnell et al. 1992, 1996

Table 3.3 Published mechanical properties of ligaments, muscles, joints and cochlear fluid stiffness

Ligaments/ Muscles Boundary Conditions	Young's Modulus or Spring Constant	
	Published data	Source
Superior mallear ligament (C1)	4.9×10^4 N/m^2	Beer et al. 1996
Lateral mallear ligament (C2)	6.7×10^6 N/m^2	Beer et al. 1996
Posterior incudal ligament (C3)	6.5×10^5 N/m^2	Wada et al. 1996, Prendergast 1999, Ferris et al. 2000
Anterior mallear ligament (C4)	5.2×10^5 N/m^2 2.1×10^7 N/m^2	Beer et al. 1996 Wada et al. 1996, Prendergast 1999, Ferris et al. 2000
Posterior stapedial muscle (C5)	7.4×10^4 N/m^2 5.2×10^5 N/m^2	Beer et al. 1996 Wada et al. 1996, Prendergast 1999, Ferris et al. 2000
Cochlear fluid (C6)	440 N/m (for cat) 510 N/m (for cat) 0 N/m	Ladak et al. 1996 Funnell et al. 1978 Wada et al. 1996
Tensor Tympani tendon (C7)	1.4×10^4 N/m^2 2.6×10^6 N/m^2	Beer et al. 1996 Wada et al. 1996, Prendergast 1999
Incudomalleolar joint		
Incudostapedial joint	6.0×10^5 N/m^2	Wada et al. 1996, Prendergast 1999, Ferris et al. 2000
Stapedial annular ligament	6.5×10^4 N/m^2 1.0×10^4 N/m^2	Wada et al. 1996, Prendergast 1999, Ferris et al. 2000 Lynch et al. 1982

simple model are listed in Table 3.4. As shown in Table 3.4, the densities are much less than the published data in Table 3.2.

Because the ligaments and muscles were modeled as a set of linear springs along the three directions of the global coordinate system, it was inconvenient to adopt the stiffness data for the ligaments and muscles based on Table 3.3. In addition, there lack reliable published damping data. Thus the initial FE model was created without ligaments, muscles and damping. In this initial model, the stiffness of cochlear impedance was set to 440 N/m based on Ladak et al. estimation [Ladak et al. 1996], and the spring constants of the eardrum supports were set to 10^6 N/m to simulate the fixed constrains. The adjustment of the initial FE mode focused on the adjustments of the stiffness of ligaments and muscles and the damping parameters of the system.

Table 3.4 Mechanical properties of the middle ear components employed for the simple FE model

Properties	Eardrum	Malleus	Incus	Stapes
Density: ρ (kg/m^3)	1.2×10^3	0.85×10^3	1.35×10^3	1.55×10^3
Young's modulus: E (N/m^2)	3.2×10^7	1.41×10^{10}	1.41×10^{10}	1.41×10^{10}
Poisson's ratio: ν	0.3	0.3	0.3	0.3

3.5 Simple FE Model Calibration

The experimental measurements used for the simple FE model calibration were conducted by Gan *et al.* on seventeen normal fresh-frozen, cadaveric temporal bones (age 32 to 96 years, 13 males and 4 females) [Gan *et al.* 2001]. A small reflective tape was placed on the center of the stapes footplate to serve as a laser-reflective target. When pure tone narrow band, filtered sound of 90 dB SPL was delivered near the eardrum in the ear canal, the displacement of the stapes footplate caused by the sound pressure on the eardrum was measured across the frequency range of 250-8,000 Hz. The measurement was conducted using a single point laser Doppler interferometer by focusing the helium-neon laser beam onto the reflective tape on the center of the stapes footplate. The measured mean peak-to-peak displacement of the stapes footplate on the seventeen temporal bones was employed to calibrate the FE model. The mean curve was employed instead of 17 curves so that the average trend of the frequency response curves of the stapes footplate displacement can be captured easily.

To be consistent with the experimental setup, the simple FE model was applied a uniform pressure of 90 dB SPL (0.632 N/m^2) on the lateral side of the eardrum. The harmonic analysis was conducted on the FE model across the frequency range of 250-8,000 Hz. The displacements of the stapes footplate in frequency field were collected and converted to the peak-to-peak displacement response of the stapes footplate. The objective of the FE model calibration process is to match the FE model prediction with the experimental curve obtained by the laser Doppler interferometry (LDI) as close as possible, by adjusting undetermined model parameters of the simple model. The curve obtained from the initial model was shown in Figure 3.7 with the LDI curve, the mean of 17 experimental curves.
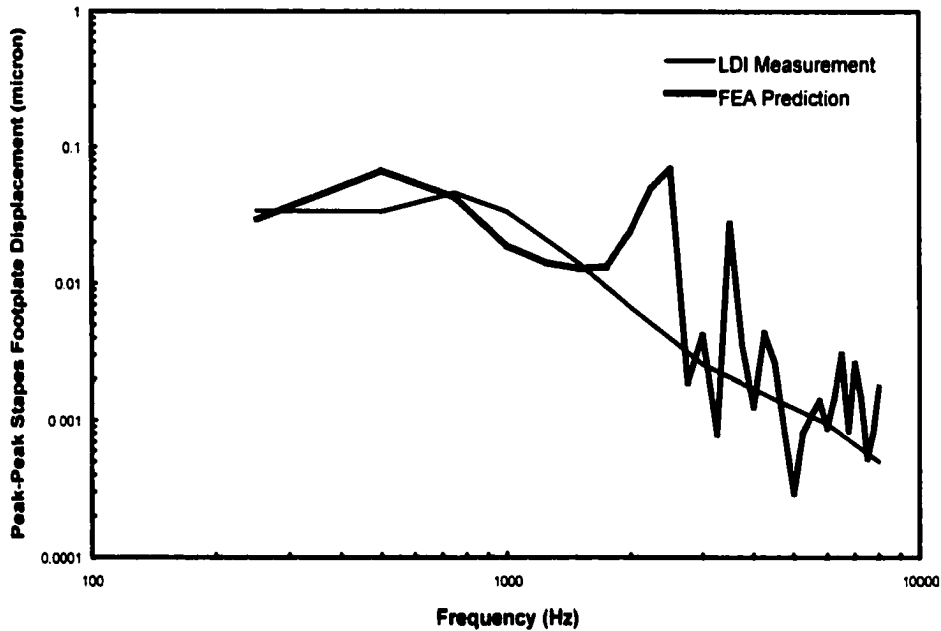
Figure 3.7 Stapes footplate displacement frequency response for the initial FE model

During the FE model calibration process, the dimensions and geometric shape of the model were kept constant. The published mechanical properties were selected for the main middle ear components. The parameters to be adjusted were mainly limited to the mechanical properties of ligaments, muscles and eardrum periphery support. In another word, the FE model calibration process was nothing but finding an optimum combination for the mechanical properties of ligaments and muscles by means of the cycling optimization method [Reklaitis *et al.* 1983]. The stiffness of the ligaments or muscles was alternatively cycled to search for a set of optimum ligament or muscle stiffness values.

Next, we show how to estimate the adjustment ranges for the stiffness of ligaments and muscles. According to Wever and Lawrence's work, the length and cross-sectional area of the tensor tympani muscle are 25 *mm* and 5.85 *mm*^{2} respectively, and the length and cross-sectional area of the posterior stapedial muscle are 6.3 *mm* and 4.9 *mm*^{2}

respectively [Wever and Lawrence 1954]. By assuming a muscle to be a bar (a two-force element), then we can estimate the longitudinal stiffness of the muscle by the following formula:

$$k = \frac{EA}{L}$$ (3.3)

where k is the longitudinal stiffness; L and A are the length and the cross-sectional area of the muscle, respectively; and E is the Young's modulus of the muscle. If the bar is regarded as a spring, the longitudinal stiffness is its spring constant. In Table 3.3, there are two values, 1.4×10^4 N/m^2 and 2.6×10^6 N/m^2, for the Young's modulus of the tensor tympani muscle; and two values, 7.4×10^4 N/m^2 and 5.2×10^5 N/m^2, for the Young's modulus of the posterior stapedial muscle. Based on the above discussion, we estimated two spring constant values, 3.3 N/m and 608.4 N/m, for the tensor tympani muscle; and two spring constant values, 57.6 N/m and 404 N/m, for the posterior stapedial muscle. Therefore the stiffness adjustment range of the muscles was set to be between 0 and 1000 N/m. Under the assumption that the stiffness difference among ligaments and muscles is not too large, the stiffness adjustment range of ligaments were also set to 0~1000 N/m.

In the adjustment range, the cycling processes were conducted. The first ligament C1 was added to the initial model. The stapes footplate frequency response curves with the stiffness values of 0, 100, 200, 300, 400 N/m for ligament C1 were calculated. The curves of different stiffness values obtained from finite element analysis (FEA) were compared with the experimental curve, as illustrated in Figure 3.8. In the figure, it is seen clearly that the stiffness of ligament C1 affects the frequency response curve significantly. From these curves, the stiffness value that gives the "best" curve oscillating along or closest to the experimental curve was adopted. In this case, the value of 300 N/m was selected for ligament C1. Then the second ligament was added with the first ligament kept in the
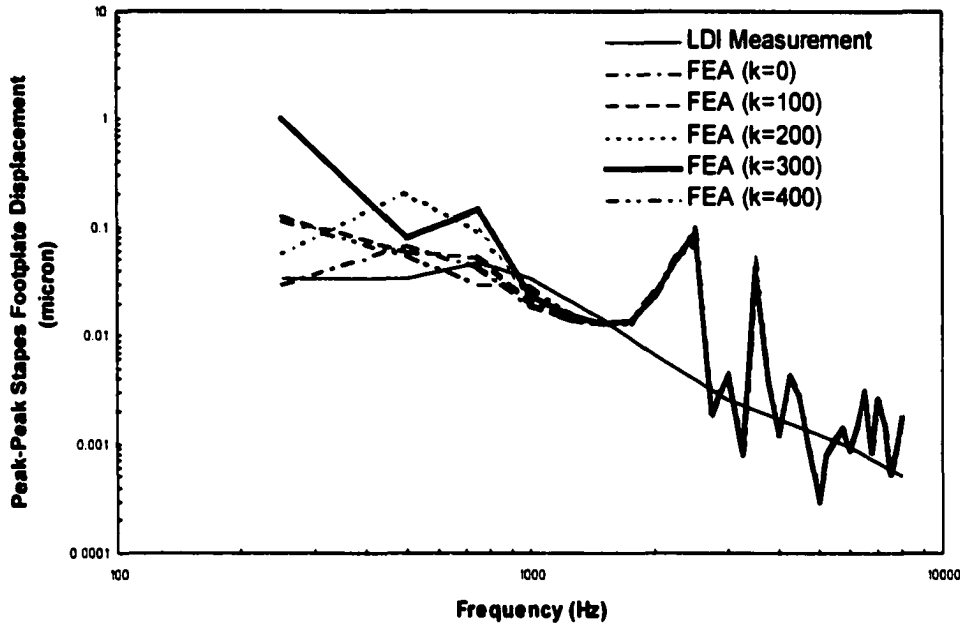
Figure 3.8 Select the optimum stiffness value of ligament C1

model. The same procedure was conducted and the "best" stiffness value was obtained for the second ligament. When the "best" stiffness value for the last ligament or muscle was adopted, the first cycle ended. The stapes footplate displacement response curve after completing first cycle is shown in Figure 3.9. The stiffness values are 300, 400, 400, 300, 50, 300 N/m, respectively, for ligaments C1, C2, C3, C4, C5 and C7.

The second cycle started with the set of ligament or muscle stiffness values obtained from the first cycle. The same procedure was used except keeping all ligaments and muscles in each step. When the cycling procedure was performed several times and the frequency response curve obtained from the FEA could not be further improved, the set of ligament or muscle stiffness values was accepted.

The same method was employed to search for the optimum cochlear fluid impedance stiffness, the Young's modulus of the eardrum and the damping coefficients of the
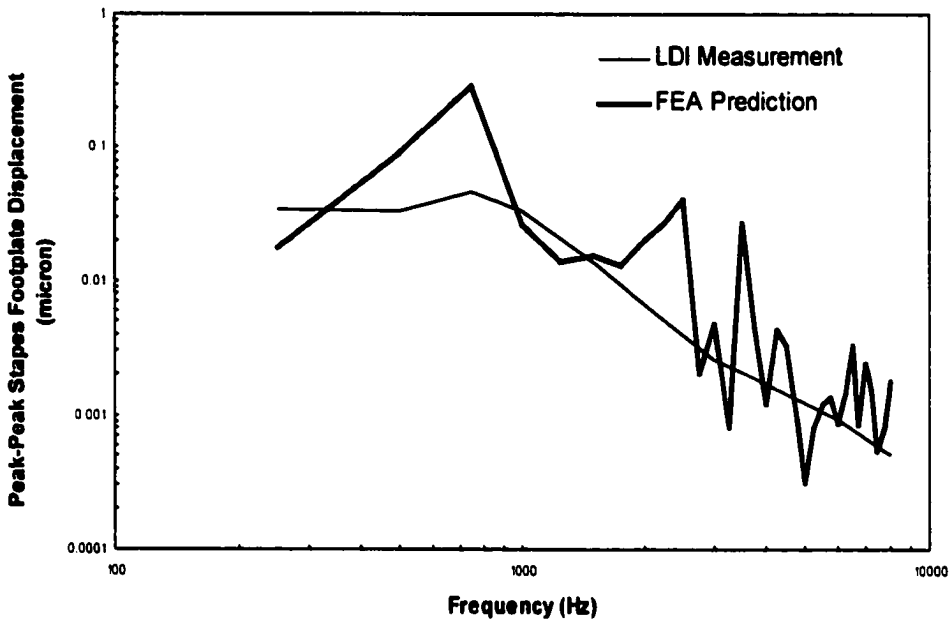
Figure 3.9 FE stapes footplate displacement response curve after first cycle

model. Figure 3.10 shows the stapes footplate displacement frequency response curve

using the optimum combination of the mechanical properties that is shown in Tables 3.5

and 3.6.

Table 3.5 Mechanical properties of the human middle ear simple FE model

Properties	Eardrum	Malleus	Incus	Stapes
Density: ρ (kg/m^3)	1.2×10^3	0.85×10^3	1.35×10^3	1.55×10^3
Young's modulus: E (N/m^2)	1.6×10^7	1.41×10^{10}	1.41×10^{10}	1.41×10^{10}
Poisson's ratio: v	0.3	0.3	0.3	0.3
Damping coefficients: β (s)	0.0001	0.0001	0.0001	0.0001

Table 3.6 Boundary conditions of the human middle ear simple FE model

Ligaments/Conditions		Spring Constant (N/m)	Damping (N-s/m)
Superior mallear ligament	C1	500	0
Lateral mallear ligament	C2	400	0
Posterior incudal ligament	C3	500	0
Anterior mallear ligament	C4	300	0
Posterior stapedial muscle	C5	50	0
Cochlear fluid	C6	60	0.054
Tensor Tympani tendon	C7	40	0
Eardrum Support Spring		1.0×10^0	0
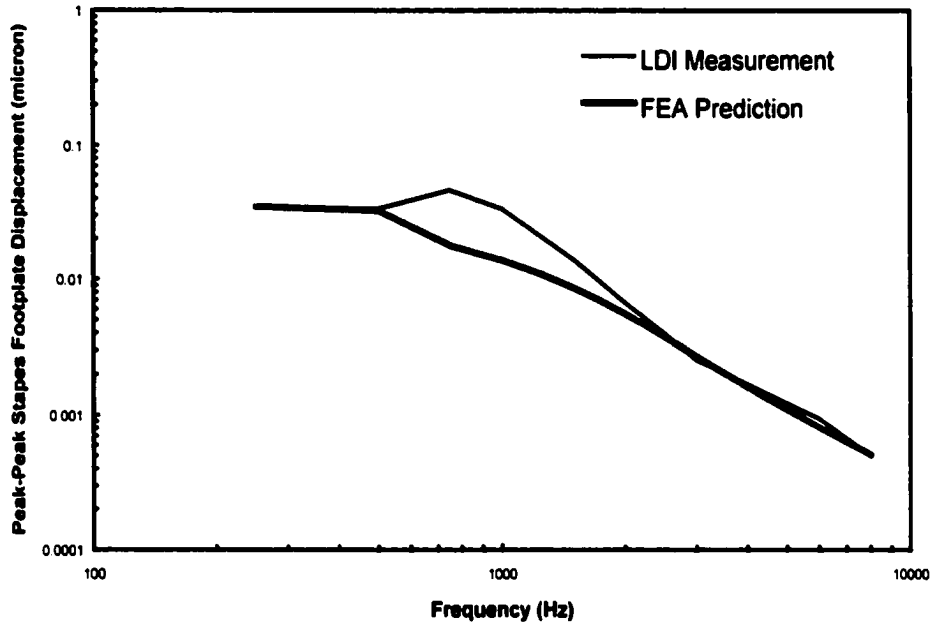
Figure 3.10 FE stapes footplate displacement frequency response curve after cycling
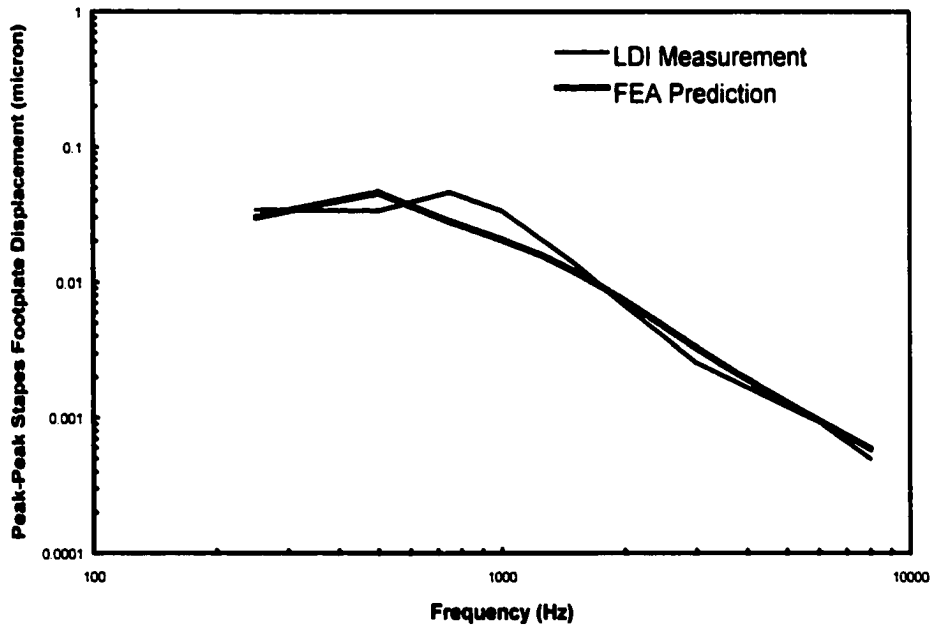
Figure 3.11 FE stapes footplate displacement frequency response curve
after changing the thickness of the eardrum to 0.074 mm

To further improve the curve, the thickness of the eardrum is uniformly changed to 0.074 mm that is another published data, so that the resulting curve is closer to the experimental one, as shown in Figure 3.11.

3.6 Observations And Lessons Learned

Observations and lessons learned from this simple FE model are summarized as follows:

(1) The frequency response curve of stapes footplate displacement obtained using the simple FE model is plotted with the 17 LDI experimental curves in Figure 3.12. It is shown that the FE curve matches the experimental curves very well. However, some important parameters of the FE model, such as the densities of ossicles and Young's modulus of the eardrum are out of the reasonable ranges, as listed in Table 3.3.
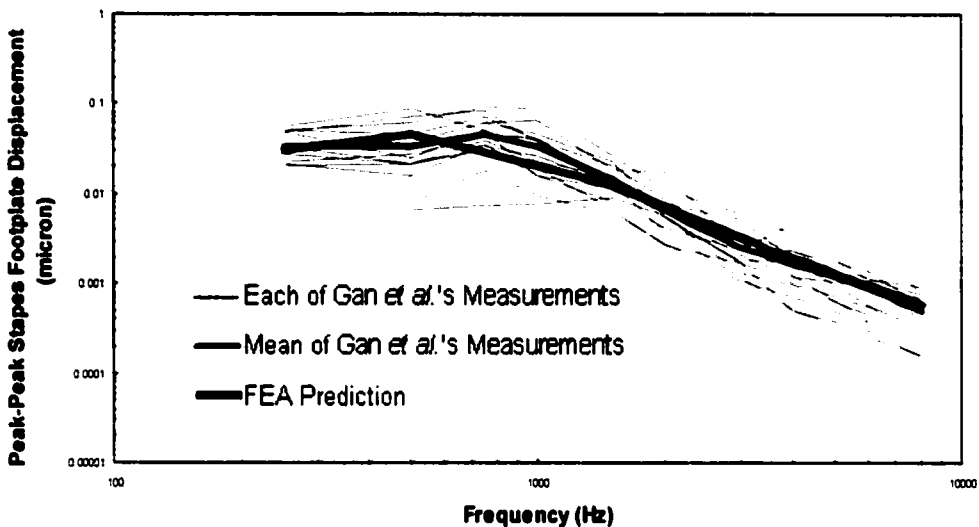
Figure 3.12 Stapes footplate displacement frequency response curves:
FEA prediction and Gan *et al.* 17 LDI experimental curves (2001)

(2) The stiffness of ligaments or muscles affects the stapes footplate frequency response curve significantly, especially, in low frequency range.

(3) The Young's modulus of the eardrum affects the frequency response curve significantly in all frequency range.

(4) The effect of damping coefficients was complicated. The stiffness matrix multiplier β smoothed the curves in all frequency range. The larger the stiffness matrix multiplier, the flatter the curve. The damping coefficient of the cochlear fluid had an important impact on magnitude of the frequency response curve, especially in high frequencies.

(5) The support elasticity at the eardrum periphery had no significant influence on the frequency response curve. It is unreasonable in reality though. One possible explanation is that the membrane element (SHELL 41) employed in modeling the eardrum makes its periphery so flexible that the additional support elasticity is almost ineffective.

The simple FE model is successful in supporting the preliminary study of human middle ear mechanics. With this model, we have not only obtained a valuable FE modeling experience but also developed a satisfactory method of calibrating the FE model. In addition, we obtained good results using the simple model. These results help us better understand the middle ear mechanics.

However, the simple FE model has to be improved to predict the behavior of human middle ear more accurately. This is particularly because its geometric shape and spatial arrangement are based on sketch and best possible characteristic geometric dimensions. Furthermore, the ultrastructure of the eardrum was neglected and a number of main mechanical properties, such as mass densities, were out of the physiologically reasonable ranges. Therefore, a new FE model of human middle ear needs to be developed based on serial histological sections of human temporal bone, which will be presented in the following chapters.

CHAPTER FOUR

COMPUTER-AIDED GEOMETRIC MODELING OF

HUMAN MIDDLE EAR

In this chapter, an advanced computer-aided modeling method that supports engineers to establish accurate 3D geometric and finite element models of human middle ear is presented. This method combines the traditional histological morphometry study and the computer-aided geometric modeling and computer-aided design (CAD) technology. In this method, a set of histological slides is employed for capturing the basic geometry of the middle ear. Although the magnetic resonance imaging (MRI) and the computer temography (CT) scans seem to be ideal for this purpose, the resolution for ordinary CT and MRI is not adequate. Moreover, both methods demand expensive equipment, the implementation of complex image processing and numerical techniques.

A brief overview of the proposed approach is shown in Figure 4.1. As illustrated in the figure, the proposed approach includes four stages that will be respectively discussed in the following four sections. In Section 4.1, the histological section preparation of human temporal bone, the first stage, will be discussed. Section 4.2 describes the stage of the scanning and imaging process. The section digitization and the solid model construction stages are respectively described in Section 4.3 and Section 4.4. Potential errors induced in various stages are discussed as well.

61
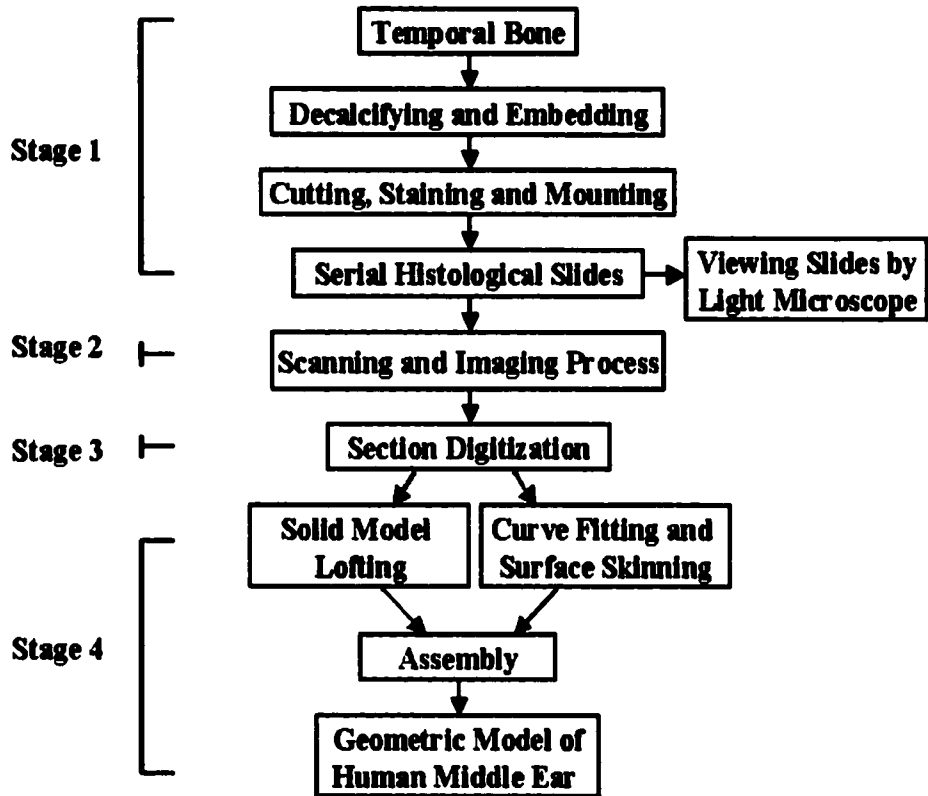
Figure 4.1 Computer-aided geometric modeling of human middle ear

4.1 Histological Section Slide Preparation Of Human Temporal Bone

4.1.1 Decalcifying And Embedding A Temporal Bone

A freshly extracted human temporal bone (female, age 52, right ear) was first observed under a Zeiss OPMI-1 operating microscope [Carl Zeiss, Inc.] to confirm an intact eardrum and normal ear canal. Then the bone was fixed in aldehyde and decalcified in 10% nitric acid for at least two weeks. The specimen was then run through graded alcohols to absolute alcohol ethyl for dehydrating. The temporal bone was placed in a jar with 3% celloidin dissolved in absolute alcohol ethyl. In order to ensure that the celloidin penetrated into every cavity of the temporal bone, the jar was left uncovered and was placed in a vacuum bottle on a moving table for a week. And then, the specimen was transferred to 6% and finally 12% celloidin each for one week. The temporal bone was allowed to harden slowly by controlled evaporation and finished off with immersion in chloroform over a two-week period. The resulting block, roughly $25 \times 20 \times 15$ mm^3 in size, was then removed from the container, trimmed and mounted on a metal chunk and stored in 70~80% alcohol [Igarashi 1964; Donahue & Gussen 1966].

4.1.2 Section Cutting

Before the specimen was cut for histological sections, four parallel fiducial holes were vertically (from superior to inferior) drilled in the celloidin block surrounding the middle ear structure. The holes were drilled with the guidance of the holes in a wooden block placed over the specimen in order to keep them perpendicular to the cutting plane. Permanent black ink was injected into these holes to color the fiducial marks. The

specimen was then cut horizontally on an AO 860 sliding microtome [American Optical Corporation] at a thickness of 20 µm for 600 histological sections that were saved in 80% alcohol. Illustrations and detailed steps of the cutting setup and procedure are described in Figures 4.2.

Cutting Setup

(1) Level the fixture set of the microtome using an Empire 360-4 level [Empire Level Mfg. Corp.] and tighten the tightening screw.

(2) Mount the celloidin block in the fixture and make sure its cutting plane is horizontal.

(3) Install a dripping bottle with 70% alcohol on a frame and adjust the dropping hose to drop alcohol on the cutting plane of the block for keeping the block hard.

(4) Adjust the knife stand to clear from the cutting plane of the celloidin.

(5) Mount the long knife on the knife stand.

(6) Set vertical increment at 20 µm on the microtome and tighten the screw.

Cutting Procedure

(1) Pull the knife through the block smoothly and quickly.

(2) Spread out the section.

(3) Put a slide paper with a serial number over the section.

(4) Slide the section away along the knife blade and put it in the 70% alcohol with its face down in a peri-dish.

(5) Store the sections in a covered bottle with 70% alcohol after finishing cutting.

Figure 4.2 Cutting setup and celloidin block cutting

4.1.3 Section Staining

The sliced temporal bone sections, obtained from the procedure described in Figure 4.2, were stained with eosin and hematoxylin in a sequential series of every 10th section. The detailed staining setup and procedure are described as in Figure 4.3.

Step #	Solutions for Staining	Solution Makeup	Purpose	Layover Time (Second)
1	Stilled water		Hydrate	15
2	Stilled water		Hydrate	15
3	Hemotoxylin (10%)	Diluted with stilled water	Stain	30
4	Tap water		Rinse	30
5	Alcohol Ethyl (50%)		Rinse	A few
6	Alcohol Ethyl (50%)		Rinse	A few
7	Clarifier	70% Alcohol Ethyl + 10% Acetic		A few
8	Tap water			A few
9	Bluing reagent	3 ml Ammonia Hydroxide + 1 liter tap water		30
10	Tap water			30
11	Alcohol Ethyl (95%)	Ethyl Alcohol – 190 proof		30
12	Eosin (1%)	5 gram Eosin Y + 500 ml stilled water	Stain	30
13	Alcohol Ethyl (70%)		Rinse	30
14	Alcohol Ethyl (100%)	Ethyl Alcohol – 200 proof	Dehydrate	30
15	Alcohol Ethyl (100%)	Ethyl Alcohol – 200 proof	Dehydrate	30
16	Alcohol Ethyl (100%)	Ethyl Alcohol – 200 proof	Dehydrate	30
17	100% Alcohol Ethyl + Chloroform	Half 100% Alcohol Ethyl + Half Chloroform		30
18	100% Alcohol Ethyl + Chloroform	Half 100% Alcohol Ethyl + Half Chloroform		30
19	α turpineal + histoclear	Half α turpineal + Half histoclear		30
20	α turpineal + histoclear	Half α turpineal + Half histoclear		30

Figure 4.3 The staining setup and procedure

4.1.4 Slide Mounting

Each stained section was mounted on a glass slide immediately after staining. A total of 60 slides were obtained, and the anatomical distance between two adjacent slides was about 0.2 mm. The section mounting follows the procedure shown in Figure 4.4.

(1)   Put a section on a slide (75×50×1 mm) from the α turpineal-histoclear solution and then spread it.
(2)   Align and trim the edge of the section.
(3)   Blot the section using bibulous paper.
(4)   Drop glue (permont) on the section.
(5)   Cover the section with a microscope cover glass (45×50×0.1 mm).
(6)   Remove the bubbles between the permount and the slide.
(7)   Weigh down the slide with two weights for one week.
(8)   Store slides in a slide box.

Figure 4.4 Section mounting procedure

The black ink injected in the fiducial holes for fiducial marks still remained around the edges of the four fiducial holes on each section after staining and mounting, so that the fiducial marks can be identified in the finished slides.

4.2 Imaging Process

The sixty slides, with the required geometric information of the middle ear enclosed, were scanned into computer as digital images with a resolution of 1200 pixels per inch. These images were saved in TIFF (Tag Image File Format), a common image format widely accepted. Each section image file was named as B plus its section serial number (for example, B450). Then the middle ear components, including malleus, incus, stapes and eardrum, were identified and marked on the section images by an otologist, as shown in Figure 4.5. Before digitizing these images, they were oriented, aligned, stretched and trimmed in Adobe Photoshop [Adobe Systems Incorporated] to maintain consistency across the sections by referring to the fiducial marks.
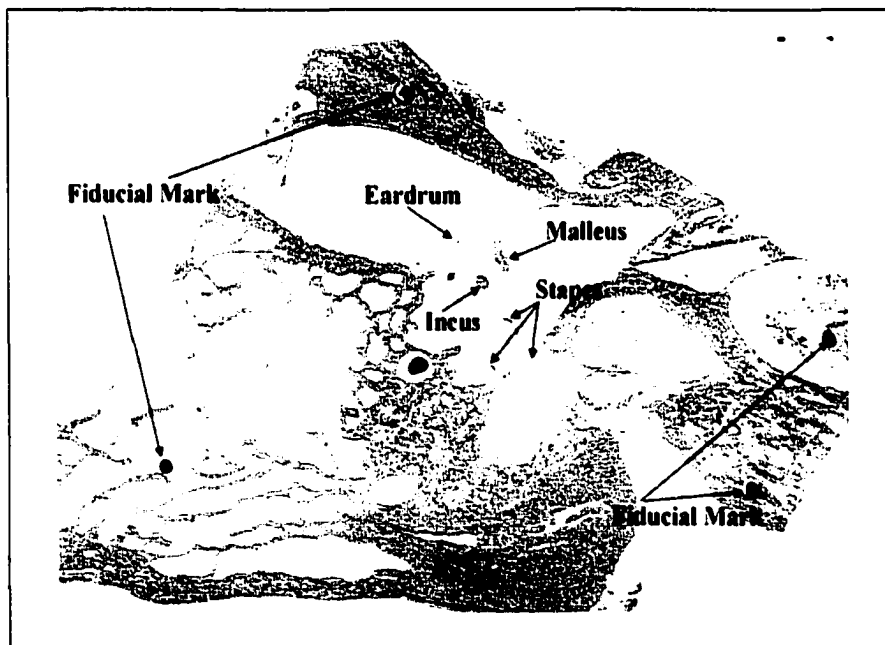
Figure 4.5 A typical section image identified by an otologist

There were three steps involved in the imaging process. First, the section images were rotated to make the two bottom fiducial marks align horizontally, as shown in

67

Figure 4.6. This step ensured that all section images were properly oriented. Second, a standard template with four fiducial marks (A, B, C, D) was constructed using a typical section image, as shown in Figure 4.7. Finally, the template was used as the base with

Step 1. Adjustment of Image Orientation

(1)   Start Photoshop and choose *File>Preferences>Units & Rulers* to set the unit to cm.

(2)   Choose *File>Preferences>Guides & Grid* to set a gridline every 1 cm and 10 subdivisions and turn on ruler and grid.

(3)   Import an image into Photoshop and choose *Image>Adjust>Brightness/Contrast* to adjust its *contrast/brightness* to make four fiducial marks (A, B, C, D) clear.

(4)   Measure the coordinates of the center of two fiducial marks (A and B) on the bottom of the image and record them. Then calculate the angle θ between the horizontal line and the line joining the centers of these two fiducial marks.

(5)   Choose *Image>Rotate Canvas>Arbitrary* to rotate the image with angle θ in order to make the two fiducial marks to lie on the same horizontal line.

(6)   Save the image.

(7)   Repeat (3) ~ (6) for each image.

Figure 4.6 The orientation of the images

68

Datum

Step 2. Constructing a Standard Template

(1)   Import a carefully oriented section image (for example, B450) into Photoshop as the base for constructing the standard template.

(2)   Choose *Layer>New layer* to get a new layer and name it "template".

(3)   Activate the template layer. Click *Elliptical Marquee Tool* and select one of the four fiducial marks. Choose *Select>Modify>Border* and type in a width value of 1 pixel. Then click *paint bucket tool* and fill the highlighted ring area with a solid color. Go through other three fiducial marks following the same procedure. By now, there are four small circles to serve as the reference points on the template.

(4)   Click *line tool* and draw a horizontal line connecting the centers of the two bottom circles (A and B), and two orthogonal lines through the centers of each circle. Use these lines as datum lines. The center of A, which is the intersection point of the horizontal line and the left vertical line, is taken as the datum point for aligning images.

(5)   Duplicate the template layer into a new file named template.

Figure 4.7 The standard template

the referencing datum point for calibrating all the section images, as shown in Figure 4.8. By aligning the fiducial marks on each section image with those on the template, the

Step 3. Adjusting Individual Images

(1)   Bring a properly oriented section image into Photoshop.

(2)   Activate the template file and choose *layer>duplicate layer* to duplicate the template into the new image.

(3)   Activate the background and select the center of fiducial mark A as the origin of this image. Click *Move Tool* to move the section image to make its origin coincide with the datum point of the template.

(4)   Compare the dimensions and the positions of the fiducial marks on the section image with the circles on the template. Modify the image to make the fiducial marks on the section image to match the corresponding circles as accurately as possible in dimension and position by scaling the new image. The scaling ratio is determined by the mean stretching rate of the distance of any two fiducial marks with respect to the corresponding distance of two circles on the template.

(5)   Delete the template layer. Click *Rectangular Marquee Tool* and select a standard sized rectangle with dimensions 1.2 cm×1.1 cm beginning from the left top position, which is recorded for all section images.

(6)   Choose *Image>Crop* to trim the section image as a standard sized image and save it in bitmap format to obtain a standard sized image file.

(7)   Repeat (1) ~ (6) for each section image to obtain the standard sized section image file.

Figure 4.8 Adjustments of the individual image

70

section images were calibrated. They were then trimmed to standard sized images, which

enclose ossicles, eardrum and surrounding structures, as shown in Figure 4.9.
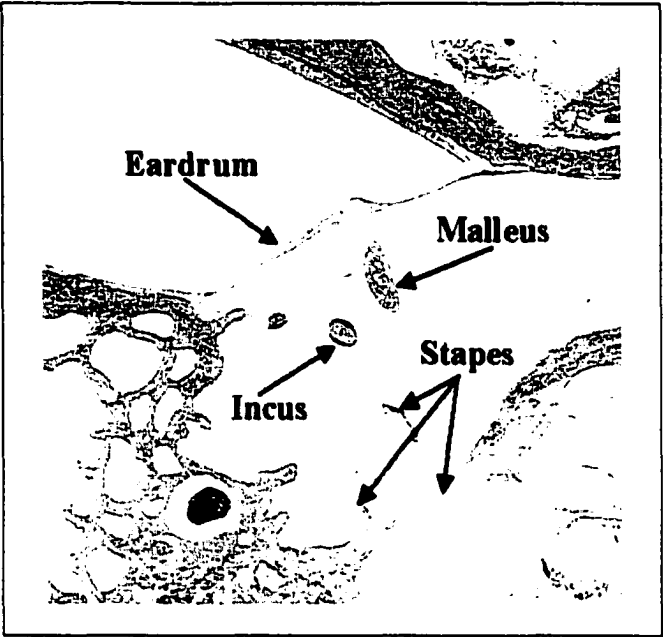
Figure 4.9 The standard sized section image

4.3 Section Digitization

After completing the imaging process, sixty standard sized section images were digitized using SolidWorks, a commercial CAD software. The standard sized section images were imported into SolidWorks and served as the information source of 2D geometric contours. The contours of each middle ear component on the section images were digitized for creating closed curves that characterized the middle ear geometry. The procedure is described as follows. A reference rectangle was created on the Plane1 (OXY plane) of the sketch mode in SolidWorks, as shown in Figure 4.10. Note that this rectangle was created with the same dimensions as the standard sized image to ensure that the actual size of the section image can be represented accurately in SolidWorks. Then sixty sketch planes parallel to plane1 were created in SolidWorks for digitization. Note that each section image was imported into SolidWorks on its corresponding sketch plane. The distance between two adjacent sketch planes was 0.2 mm, which was identical to the distance between two corresponding adjacent section images extracted from the temporal bone. The next step was to bring a standard sized section image onto the corresponding sketch plane, and fit it to the reference rectangle. The 2D contours of the middle ear components, including eardrum, malleus, incus and stapes, were then digitized on the sketch plane from the section image. This was carried out by properly marking points along their boundary using the "Point" option of the sketch mode in SolidWorks, as shown in Figure 4.10. Finally the image was removed from the sketch plane.

The same procedure was conducted for each standard sized section image. The digitized contours were saved separately for malleus, incus, stapes and eardrum. Then the files were used to build the contour curves for the middle ear components separately
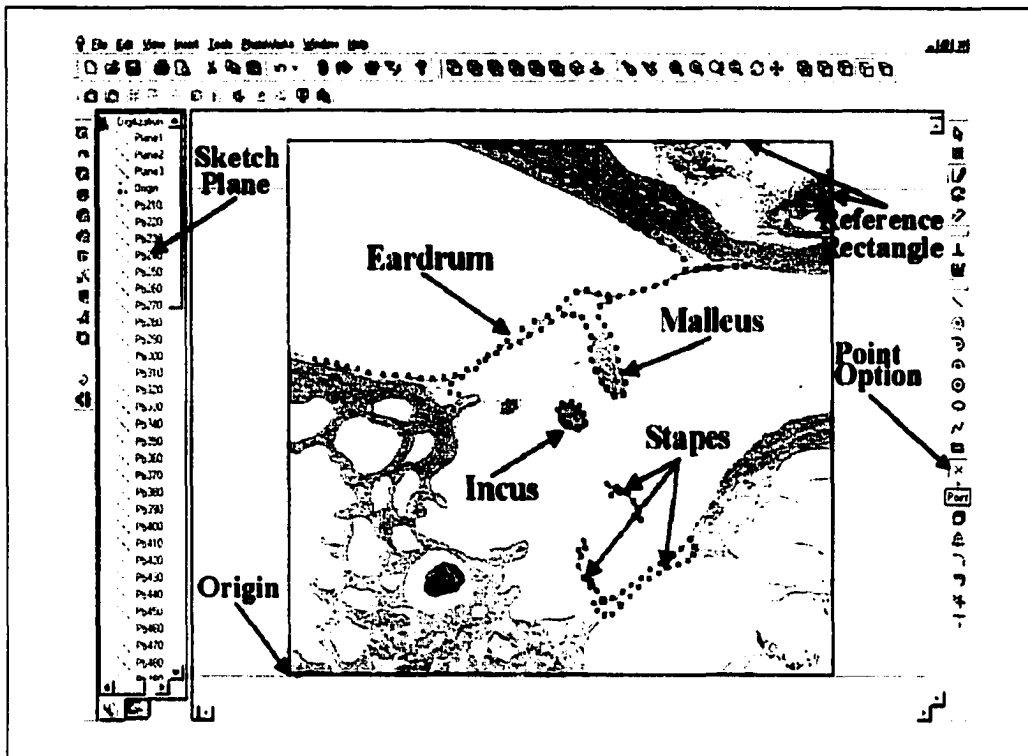
Figure 4.10 Reference rectangle, sketch plane and section contours
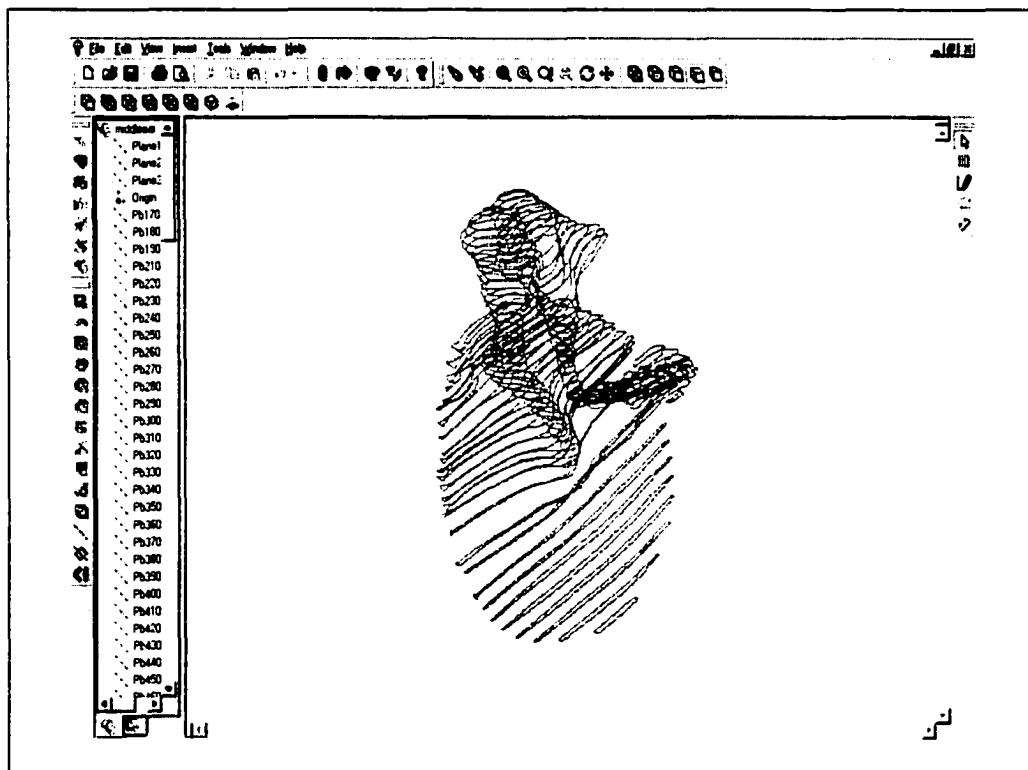
Figure 4.11 Section contours of the middle ear represented by a series of curves

using the "Spline" option of the sketch mode in SolidWorks. Figure 4.11 shows the section contours of the malleus represented by a set of serial Spline curves. In this way, the relative positions among middle ear components were well maintained for final assembly of the middle ear components. The procedure is summarized in Figure 4.12.

(1) Start SolidWorks and open a new part file. Choose *Tools>Options>Grid/Units* to set *Length Unit* as millimeters, *Major grid spacing* as 10 mm and *Minor-lines per major* as 10.

(2) Click Plane 1 and choose *Insert>Sketch*. Draw a rectangle with dimensions 12 mm×11 mm and make the left bottom corner of the rectangle coincide with the origin of the coordinate system in SolidWorks. Then choose *View>Modify>Zoom To Fit* to obtain a standard sized reference rectangle.

(3) Choose *Insert>Reference Geometry>Plane>Offset* to insert a reference plane parallel to Plane 1 for every image and renaming them as Pb plus section serial number (for example, Pb450). The distance between two adjacent reference planes is 0.2 mm.

(4) Choose *Insert>Object* to import a section image into SolidWorks. Select the corresponding reference plane and choose *Insert>Sketch*.

(5) Move the image to make the left bottom corner of the image coincide with that of the reference rectangle (origin of the SolidWorks' coordinate system) and drag the right top corner until the image fits into the reference rectangle.

(6) Choose *Tools>Sketch Entity>point* and click (with the Ctrl key pressed) along the contour of each component on the section image to digitize its boundary by generating a series of points. Close the sketch and delete the image. Then, rename the sketch as Sb plus its section number (for example, Sb450).

(7) Repeat (4) ~ (6) for all the images and save the working file under four different files named, separately by malleus, incus, stapes and eardrum.

(8) Open file named "malleus" in SolidWorks. Choose *Tools>Sketch Entity>spline* and click (with the Ctrl key pressed) on the digitized contour points of the malleus to create the closed contour curve for each sketch. Then save the file.

(9) Repeat (8) for the files named incus, stapes and eardrum.

Figure 4.12 Detailed procedure for section digitization

4.4 Solid Model Constructions

Two methods were employed for solid model constructions. The first method utilizes the "loft" and "doom" features available in SolidWorks to create the initial solid model of the middle ear. The second method involves curve fitting and surface skinning techniques that significantly improve the surface quality and geometric accuracy of the solid model. The second method creates solid models with much smoother surfaces. Both methods use the same set of discrete points obtained by digitization.

4.4.1 Solid Model Construction By "Loft" And "Doom" Features

The initial solid models were created using the "loft" and "doom" features in SolidWorks. The "loft" feature creates a solid model, as shown in Figure 4.13 (b), by connecting multiple closed curves on parallel planes along the plane normal direction, as

| (a) Closed Curves On Parallel Planes | (b) Lofting Solid | (c) Adding Dooms |
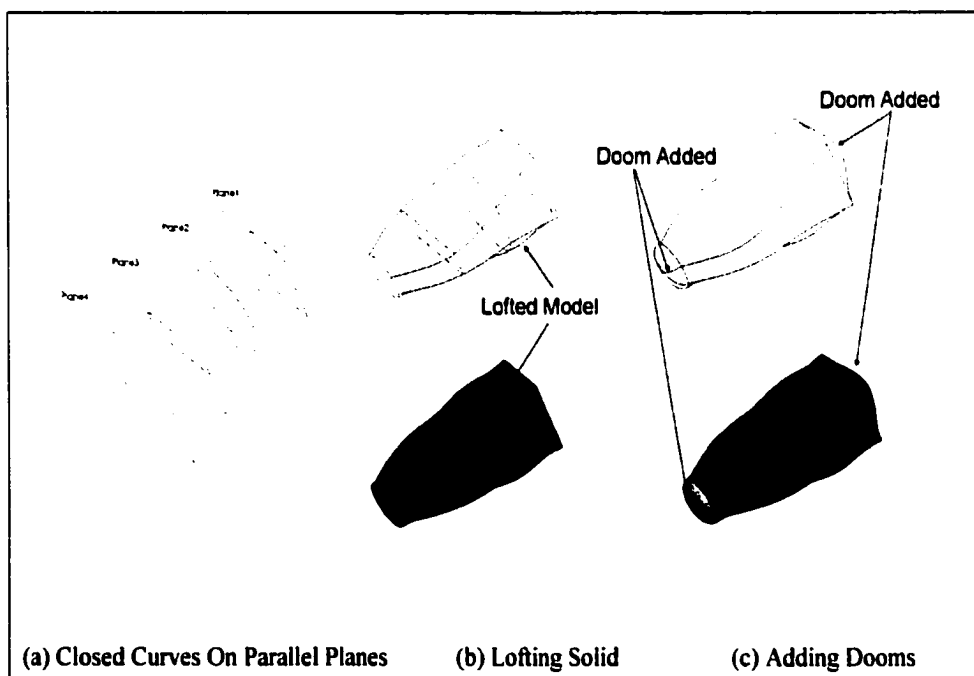
Figure 4.13 Solid model construction using "loft" and "doom" features

shown in Figure 4.13 (a). The "doom" feature adds dooms to the flat ends of the solid

model to create smooth closures for the structure, as shown in Figure 4.13 (c). Note that

the "doom" feature is C^0-continuous with the rest "loft" feature. Using the "loft" and

"doom" features, the solid models of the middle ear components were first created

separately, as shown in Figure 4.15. Then these component models were assembled to

create the entire middle ear by mating their coordinate systems, as shown in Figure 4.16.

The detailed procedure is summarized in Figure 4.14.

(1)	Open the file named malleus. Choose *Insert>Base>loft*, select the sketches representing the contours of malleus in a proper order, and click OK to create the solid model of malleus. Because the shape of each component often changes abruptly from one section to another section, sweeping through these sections for loft feature may not be straightforward in SolidWorks. Usually, these closed curves have to be divided into several overlapping groups for lofting, and some guide curves may be needed.
(2)	Choose *Insert>Features>Dome* to add a "cap" on each end of the solid model and save the file.
(3)	Repeat (1) and (2) for incus, stapes and eardrum.
(4)	Open a new assembly file. Choose *Insert>Component* to bring four components in. Assemble them by mating their coordinate systems.

Figure 4.14 The procedure of solid model construction
using "loft" and "doom" features

As shown in Figures 4.15 and 4.16, the lofted solid models are not smooth and the

rough surfaces will create difficulties in generating the finite element mesh for structural

analysis. In addition, it is problematic to translate the models from SolidWorks to other

modeling software for creating FE model. The solid model is not quite acceptable and

must be improved by other modeling techniques.

(a) Malleus   (b) Incus

(c) Stapes   (d) Eardrum
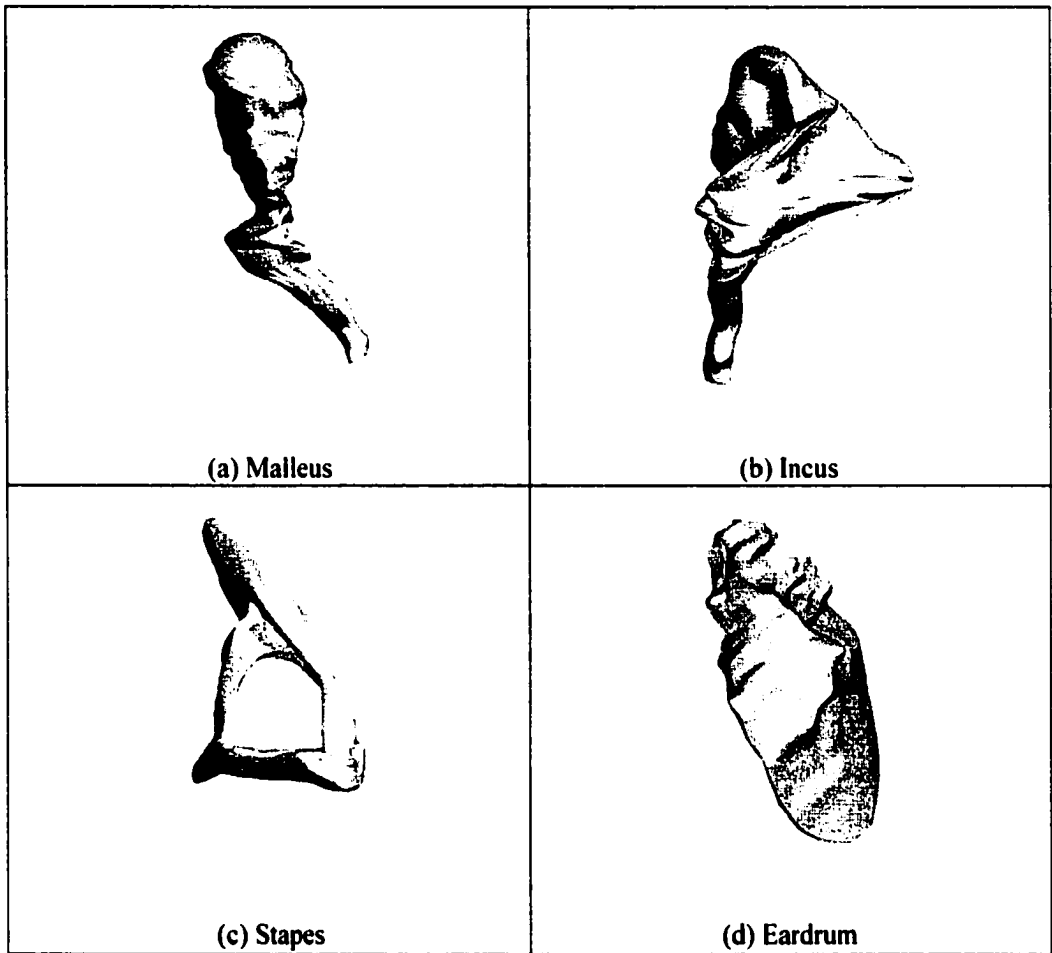
Figure 4.15 Lofted models of middle ear components

(a) Anterior View   (b) Isometric View
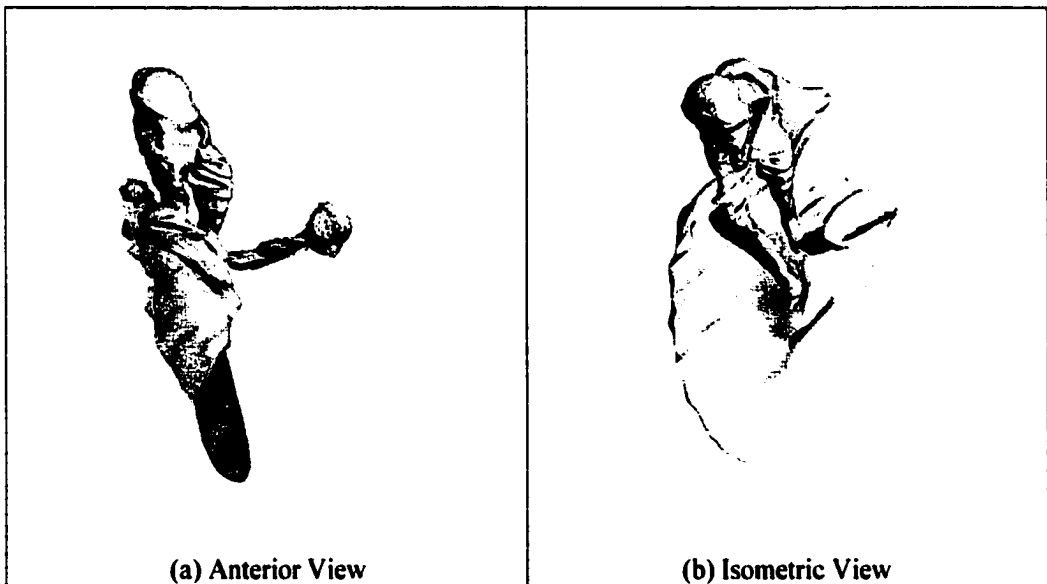
Figure 4.16 Lofted middle ear solid model

4.4.2 Solid Model Construction By Curve Fitting And Surface Skinning

To smooth the surfaces of the solid models, we employed the curve fitting and surface skinning techniques [Tang 1999]. The same set of discrete points obtained by digitizing section images of the temporal bone were retrieved from SolidWorks through its API (Application Protocol Interface). These points were employed for constructing B-Spline curves and surfaces externally to SolidWorks. These points were grouped by the individual middle ear components and arranged in sequences at each of the section images. The curve fitting technique was employed to best fit the geometric points with closed B-Spline curves on individual sections within a prescribed error bound. The surface skinning technique was then applied to quilt the series of sections using B-Spline surfaces. These techniques are briefly described as follows:

Curve Fitting Technique

The curve fitting technique employs the least square fitting for the given geometric points on a pre-selected section of an object. The best fitting curve can be obtained by minimizing the distance sum between the curve and the geometric points. The distance sum f is defined as

$$f = \sum_{j=0}^{r} \left\| \mathbf{P}_j - \mathbf{x}(u_j) \right\|^2 \tag{4.1}$$

where $\mathbf{P}_j$ is the position vector of the jth geometry point, and $r+1$ is the total number of geometric points of the contour; $\|\bullet\|$ is the norm of the vector $\bullet$; $\mathbf{x}(u)$ is the fitting B-Spline curve; $\mathbf{x}(u_j) = [x_1(u_j), x_2(u_j), x_3(u_j)]$ is the position vector of the fitting B-Spline curve at u_j, where u is the parametric coordinate of the curve. The u_j in Eq.(4.1) is defined

by the length ratio of the polygon formed by the geometric points P_j, as illustrated in Figure 4.17(a). Mathematically, the values of u_j can be calculated by

$$u_0 = 0, \quad u_j = (r+1) \sum_{k=0}^{j-1} \left| P_{(k+1)\bmod(r+1)} - P_k \right| \Big/ \sum_{k=0}^{r} \left| P_{(k+1)\bmod(r+1)} - P_k \right|, \quad (j = 1, r) \qquad (4.2)$$

and the B-Spline curve is defined as,

$$x(u) = \sum_{i=0}^{n} B_i \, N_{i,k}(u) \qquad (4.3)$$

where B_i is the ith control point shown in Figure 4.17(b), $n+1$ is the number of control points, and $N_{i,k}(u)$ is the basis function of the B-Spline curve defined recursively as

$$N_{i,k}(u) = \frac{(u - t_i) N_{i,k-1}(u)}{t_{i+k-1} - t_i} + \frac{(t_{i+k} - u) N_{i+1,k-1}(u)}{t_{i+k} - t_{i+1}} \quad ; \quad \begin{cases} N_{i,1}(u) = 1, & t_i \le u \le t_{i+1} \\ N_{i,1}(u) = 0, & otherwise \end{cases} \qquad (4.4)$$

where $[t_i, t_{i+1})$ is a knot span formed by the two consecutive knots t_i and t_{i+1}, and $k-1$ is the polynomial order of the basis functions [Mortenson 1985].

In order to minimize f, the derivatives of f with respect to the $n+1$ control points are set to zero. For simplicity, considering only the ℓth control point, one has

$$\frac{df}{dB_\ell} = \sum_{j=0}^{r} \left\| -2P_j \sum_{i=0}^{n} N_{i,k}(u_j) + 2\sum_{i=0}^{n} N_{i,k}(u_j) \left(\sum_{i=0}^{n} N_{i,k}(u_j) B_i \right) \right\| = 0. \qquad (4.5)$$

For $\ell = 0, n$, the above expression can be rewritten in a matrix form as

$$N^T NB = N^T P \qquad (4.6)$$

where $N \in R^{(r+1)\times(n+1)}, B = R^{(n+1)\times 3}, P = R^{(r+1)\times 3}$, and

$$N = \begin{bmatrix} N_{0,k}(u_0) & N_{1,k}(u_0) & \cdots & N_{n,k}(u_0) \\ N_{0,k}(u_1) & N_{1,k}(u_1) & \ddots & N_{n,k}(u_1) \\ \vdots & \ddots & \ddots & \vdots \\ N_{0,k}(u_r) & N_{1,k}(u_r) & \cdots & N_{n,k}(u_r) \end{bmatrix}_{(r+1)\times(n+1)} \qquad (4.7)$$
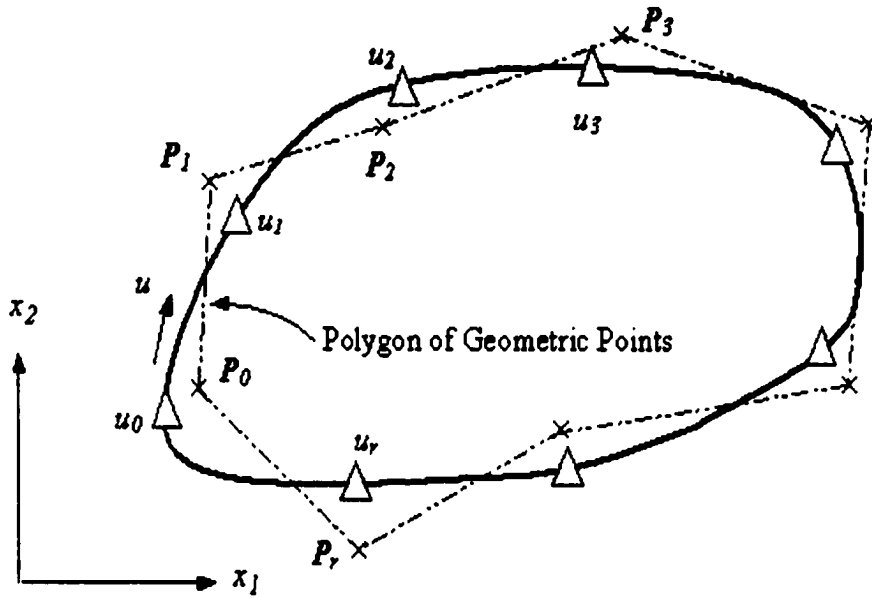
(a) Curve fitting for geometric points P_i
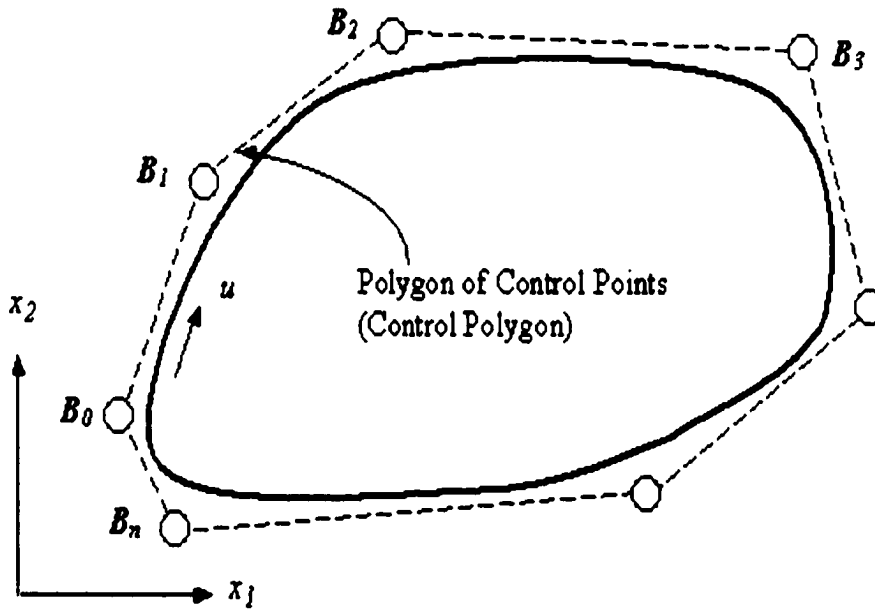
(b) B-Spline curve with control points B_i

Figure 4.17 B-Spline curve fitting

Note that $\mathbf{N^T N}$ is invertible if $N_{i,k}(u_j) \neq 0$ [DeBoor 1978]. This is true if and only if

$t_{i-k+1} < u_j < t_{i+1}$, for $i = 0, n$; and $j = 0, r$. This implies that there must exist at least one

u_j in at least one knot span so that $N_{i,k}(u_j) \neq 0$ for all basis functions. This requirement

can be achieved by adjusting the knot values of the basis functions. The curve fitting

error can be controlled by adjusting the polynomial order and the number of control

points. The output of the curve fitting is a set of control points and basis functions that

describe the smoothed section contour. The computational algorithm of B-Spline curve

fitting is summarized in Figure 4.18.

---

(1) Collect and sort geometric points;

(2) Smooth geometric points by averaging their positions with two previous and two following nodes (optional);

(3) Specify desired error bound ε;

(4) Determine polynomial order;

(5) Determine number of control points, $n+1$, as small as possible;

(6) Construct the B-Spline curve, reduce fitting error by adjusting u_j values using the chord length parameterization method;

(7) Calculate $e = f/(r+1)$, if $e < \varepsilon$, acquire control points B, to construct B-Spline curve;

(8) Otherwise, increase k or n, repeat steps 4 to 7.

Figure 4.18 The computational algorithm of B-Spline curve fitting

Surface Skinning

The fitting B-Spline curves discussed above are then related across sections to form

an open B-Spline surface, as shown in Figure 4.19, using the surface skinning technique.

Note that in this process, the number of control points of the B-Spline curves must be

kept identical across all the sections. In addition, the polynomial order of the basis

functions and knot values of the B-Spline curves must be identical on all sections. The control points are connected to their corresponding points across sections, as shown in Figure 4.19(a), to form a control polyhedron. The enclosed B-Spline surface is then constructed, as shown in Figure 4.19(b), by

$$\mathbf{x}(u, w) = \sum_{i=0}^{n} \sum_{j=0}^{m} \mathbf{B}_{ij} N_{i,k}(u) M_{j,\ell}(w),$$ (4.8)

where $n+1$ and $m+1$ are the numbers of control points in the u- and w-parametric directions, respectively; and $k-1$ and $\ell-1$ are the polynomial orders of the basis functions $N_{i,k}(u)$ and $M_{j,\ell}(w)$, respectively. Note that the B-Spline surface constructed is C^2-continuous in both u- and w-parametric directions, if cubic basis functions are assumed. End caps can be generated by introducing additional control points on the end face of the control polyhedron. More than one control points can be added to the end face and each of them can be adjusted individually to best fit the geometry of the structure. Note that the C^2-continuity is maintained between the cap and the flat end face if a bi-cubic B-Spline surface is employed. This is the main reason why the surface skinning method can produce much smoother models. The control points, $\mathbf{B}_{ij}$, and basis functions, $N_{i,k}(u)$ and $M_{j,\ell}(w)$, of the B-Spline surface can be imported back to CAD tools to support solid modeling. The computational algorithm of the B-Spline surface skinning technique is summarized in Figure 4.20.

After the closed B-Spline surfaces that represented the geometric boundary of each middle ear component were constructed using the curve fitting and the surface skinning techniques, they were then respectively imported into SolidWorks by using the API. In SolidWorks, the smooth solid models of the middle ear components were generated using
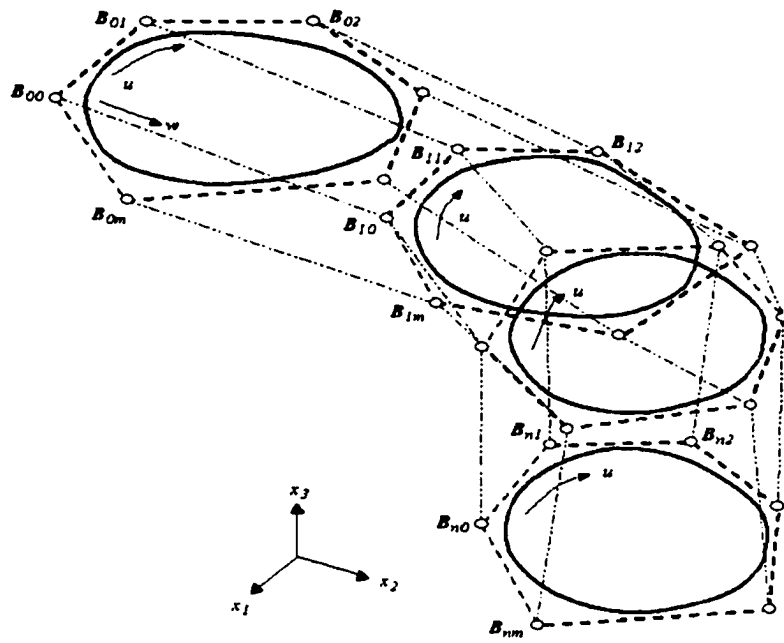
(a) Control polyhedron and section contours
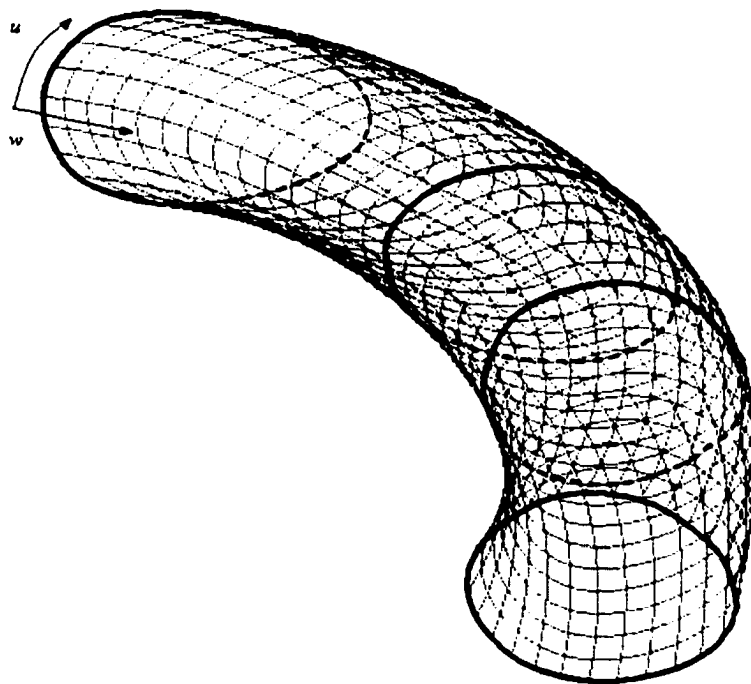
(b) B-Spline surface enclosed by the control polyhedron

Figure 4.19 B-Spline surface skinning

(1) Define the longitudinal direction (w-direction) and identify parallel sections along the direction;

(2) Acquire and sort the geometric points on each section;

(3) Find the section with the most complex geometric contour manually and construct a B-Spline curve to fit the geometric points using the curve fitting method;

(4) Obtain the minimum number of control points that describe the most complex section for a given error bound, and use it as the common number of control points for the rest of the sections;

(5) With the number of geometric points $r+1$, basis function order $k-1$, and common number of control points $n+1$ available for the jth section, use the chord length parameterization method to determine $U^j = [u_0, u_1, \cdots, u_r]$ and, subsequently, the knot vector T_u^j. This procedure is repeated for the rest of the sections;

(6) Average the knot values of the corresponding knots across all sections for a common knot vector T_u ;

(7) Generate B-Spline curves with the basis function order $k-1$, control point number $n+1$ and common knot vector T_u to fit the geometric points of each section;

(8) While performing curve fitting for each section, check the curve fitting error. If there is a section with an error that exceeds the error bound specified, define it as the section with the most complex geometric contour and repeat steps 3 to 8, until the maximum curve error is less than the desired limit ε;

(9) Construct the common basis function for the u-parametric direction, $N_{i,k}(u)$;

(10) Calculate the knot vectors T_u^{ℓ} of the ℓth row in the w-parametric direction based on the control points obtained in step 8, use the knot value placement suggested by Rogers et al. [Rogers et al. 1989]. This process is repeated for all rows.

(11) Similar to T_u, the common knot vector T_w in the w-parametric direction is determined using the same averaging scheme as step 6.

(12) Construct the common basis functions for the w-parametric direction, $M_{j,\ell}(w)$;

(13) Acquire control points B_{ij} and basis functions of the B-Spline surface, and construct the B-Spline surface.

Figure 4.20 The computational algorithm of
B-Spline surface skinning technique

the "thicken" feature. The "thicken" feature creates a solid model by thickening a surface or knitting a closed surface. Finally, these component models were assembled into the smooth middle ear model by mating their coordinate systems. Because these coordinate systems were copied from the same coordinate system used for section digitization, the assembly ensured that the components were properly positioned and oriented.

The refined middle ear solid models using the curve fitting and surface skinning techniques are shown in Figures 4.21 and 4.22. Figure 4.21 shows four middle ear components constructed. Figure 4.22 shows the assembled middle ear model in anterior view and isometric view. In comparison with the models shown in Figures 4.15 and 4.16, the quality of the surfaces of the refined model was significantly improved. The smooth model is not only closer to the real representation of the biostructure, but also facilitates translating the model from SolidWorks to other modeling tools for finite element mesh generation.

In SolidWorks, the solid model of middle ear can be easily manipulated for 3D visualization. Geometric dimensions can also be easily verified by measuring the middle ear solid model. The characteristic dimensions of the model were measured in SolidWorks and are well within the ranges of published data listed in Table 4.1. The result in Table 4.1 shows that the geometric model created by the proposed method is very accurate.

Malleus	Incus
Stapes	Eardrum
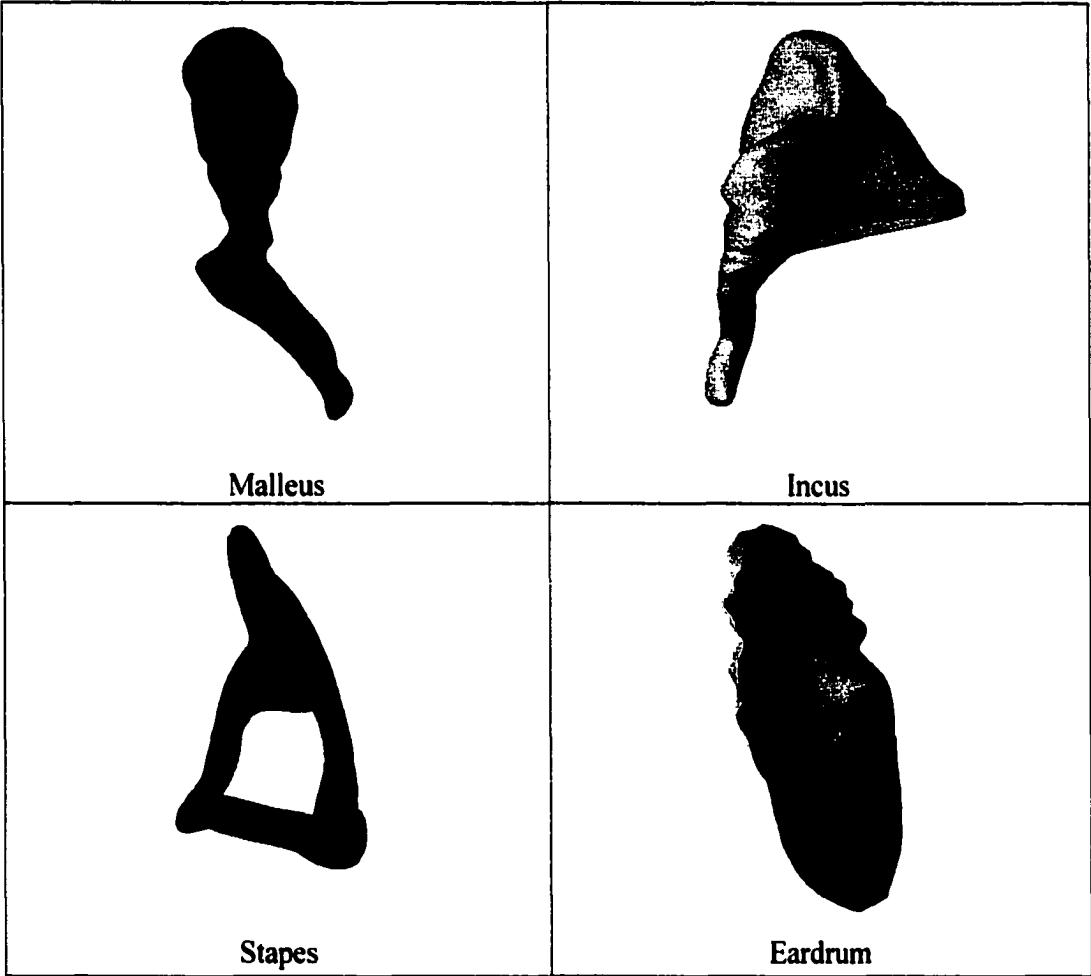
Figure 4.21 Smooth model of middle ear components

(a) Anterior View	(b) Isometric View
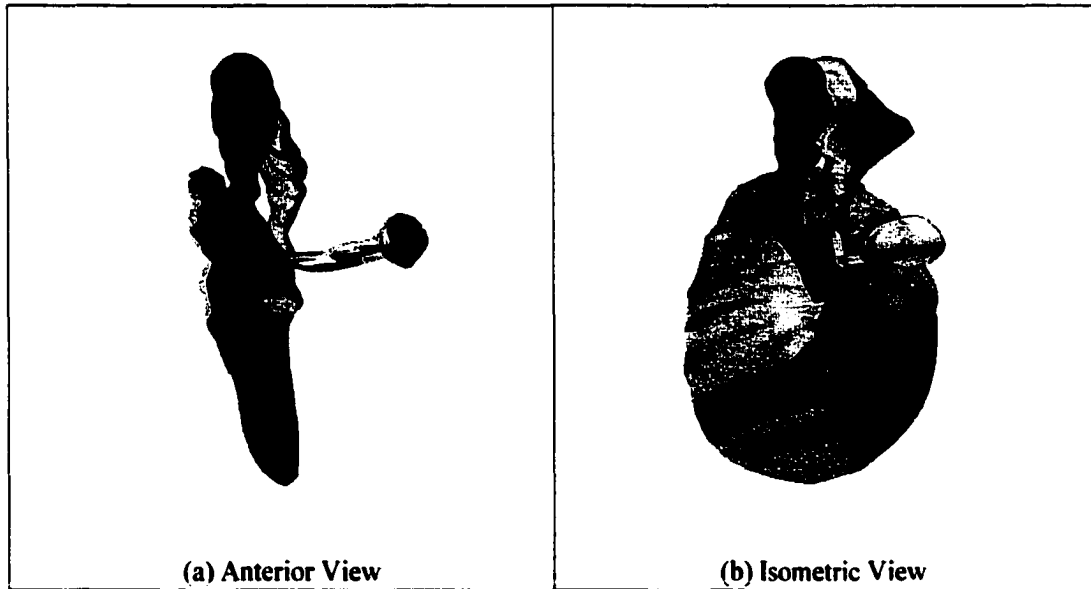
Figure 4.22 Smooth model of middle ear

EARDRUM	CAD Model Data	Published Data	Published Data References
Diameter along manubrium	8.76 mm	8.0~10.0 mm	Gray 1918 *
Diameter perpendcular to manubrium	8.93 mm	7.5~9.0 mm	Helmholtz 1863 *
Height of Cone	1.46 mm	1.54 mm 2.00mm	Wada et al. 1992 Siebenmann 1897 *
Area	66.30 mm²	55.8~85.0 mm²	Wever et al. 1954, Keith 1918 *, von Békésy 1941*
Thickness	0.05~0.074 mm	0.1 mm 0.04~0.075 mm 0.132 mm	Helmholtz 1863 * Kirikae 1960 Wada et al. 1992
MALLEUS			
Length from end of manubrium to end of lateral process	4.20 mm	5.8 mm	Stuhlman 1937 *
Total Length	7.65 mm	7.6~9.1 mm	Bast & Anson 1949 *
Weight	23.94 mg	23~27 mg	Stuhlman 1937 *, Wever et al. 1954
INCUS			
Length along long process	6.08 mm	7.0 mm	Stuhlman 1937 *
Length along short process	4.49 mm	5.0 mm	Stuhlman 1937 *
Weight	24.77 mg	25~32 mg	Stuhlman 1937 *, Wever et al. 1954
STAPES			
Height	2.87 mm	2.5~4.0 mm	Stuhlman 1937 *, Wever et al. 1954
Length of footplate	2.5 mm	2.64~3.36 mm 2.5 mm	Wever et al. 1954 Our Measurement
Width of footplate	1.38 mm	0.7~1.66 mm	Helmholtz 1863 *, Wever et al. 1954
Weight	2.24 mg	2.05~4.35 mg	Wever et al. 1954

* The work was done by the listed authors but the data came from Wever & Lawrence's book [Wever & Lawrence 1954].

4.5 Physical Middle Ear Model Fabricated By Rapid Prototyping

One major advantage of constructing a CAD solid model of the middle ear, instead of an FEA model first, is that the middle ear constructed in solid model can be fabricated for physical models directly using the rapid prototyping technique. Rapid prototyping is a fabrication technology that replicates physical prototypes of objects from their virtual mockup. The main advantage of rapid prototyping is that a physical model is built directly from the solid model, instead of employing the traditional manufacturing process. In all rapid prototyping processes, physical models are fabricated layer by layer [Jacobs 1994]. The model is mostly used for geometric verification, tooling, and for an early marketing investigation. Sometimes it can be used for function checking when high strength material such as Nylon and Polycarbonate is used.

As a general procedure, a CAD solid model is exported into a file format that describes the geometric boundary of the solid model by trianglar facets, such as an STL (Stereolithography) file [Jacobs 1994]. The faceted representation describes the approximate geometry of the solid model. In SolidWorks, the level of the approximation can be adjusted by using different quality setting. The quality setting controls the total number of the triangles in the facet approximation by adjusting the chord height deviation and the angle tolerance between the actual model surface and the triangle facets. The STL file is transferred into a slicing software, which converts the STL file into a slice-by-slice format so that the rapid prototyping machine can accept and process. The sliced model file is processed by the rapid prototyping machine to fabricate a physical prototype. The physical prototype is then fabricated and cured.

In this research, the physical model of human middle ear was fabricated using an

SLA-7000 from 3D System, Co. [3D Systems], a rapid prototyping machine as shown in Figure 4.23 (c). The CAD model of human middle ear was exported as a STL file from SolidWorks. The file includes about 390,000 facets. The STL model was then sliced by Buildstation [3D Systems], a software tool developed by 3D Systems, Co. The sliced STL file was sent to SLA-7000 and then the physical model was fabricated. The procedure is briefly shown in Figure 4.23. The physical model, as shown in Figure 4.23 (d), is pretty smooth. The model can be used for geometric verification, education, and surgical rehearsal.

By using high strength building materials, the CAD model may also be used for producing anatomically shaped prostheses through the rapid prototyping technique.

(a) CAD Model   (b) STL Model

(c) SLA-7000   (d) Physical Model
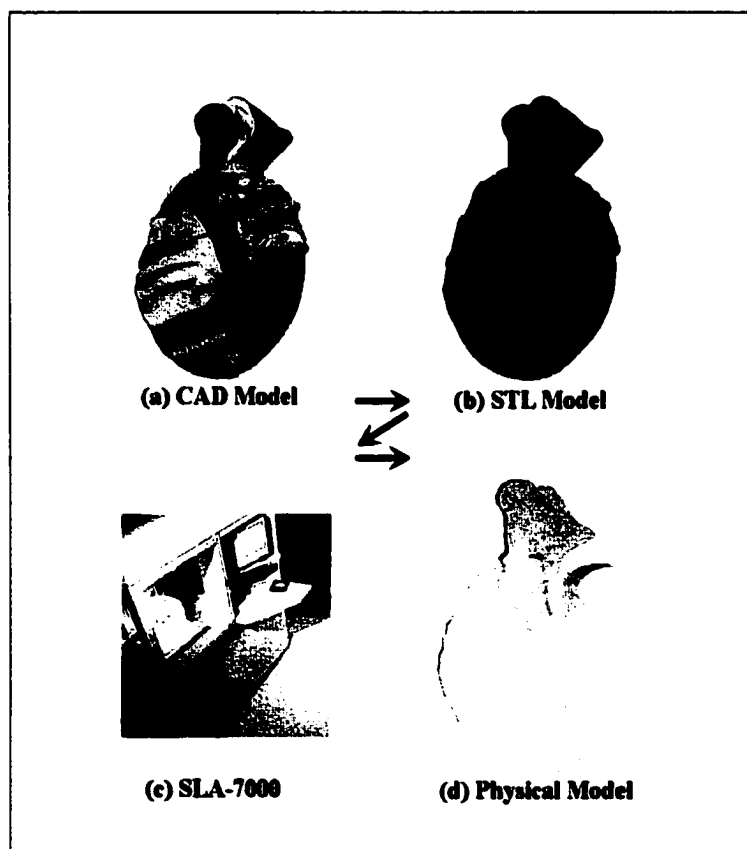
Figure 4.23 Fabrication of physical middle ear

4.6 Discussions

4.6.1 Potential Geometric Modeling Errors

We note that possible errors in the solid model mainly come from the histological section preparations (Stage 1 shown in Figure 4.1). The errors induced in the stage can be categorized into method errors and operational errors. The method errors include those induced by variations in thickness, the shrinkage, tearing, folding and wrinkle of the section issues. The variations in thickness can be alleviated by adjusting the hardness of the celloidin block and the shrinkage can be corrected by estimating the shrinking rate. The tearing, folding and wrinkle on some sections are inevitable, but the problem can be solved by substituting the damaged section by its adjacent good section and adjusting the distance from the previous layer.

The operational errors are due to inconsistency of different operators (operator inconsistency), different shrinking rate of sections and inconsistent setup if the celloidin block is cut at different time (time inconsistency), incomplete record of damaged sections, and damaged or missing fiducial marks. The operator inconsistency can be minimized by having one operator to work on the entire process. The time inconsistency can be avoided by finishing section cutting in one day. Other operational errors may be minimized or eliminated by operating carefully and keeping a good experimental record.

One other possible error may also come from the section imaging process (Stage 2 shown in Figure 4.1) while determining the center location of the fiducial mark. But it can be minimized by carefully adjusting the images; that is, carefully identifying and measuring the center of each fiducial mark. Because the computer-integrated section

digitization and solid model construction is systematic and less error-prone, we believe that the reconstructed solid model is very accurate if only the temporal bone sections are obtained consistently. This has been shown by the geometric dimensions of the constructed middle ear model comparing with those published.

4.6.2 Advantages of The Geometric Modeling Method

The proposed geometric modeling method provides researchers with a systematic and practical approach to accurately capture middle ear geometry for constructing 3D computer models. This method is accurate, systematic, low cost, and general.

This method retains the accuracy of the middle ear anatomy by employing histological section images obtained by slicing human temporal bones. The systematic imaging process aligns, orients, and resizes the section images to minimize mismatch of component contours due to inevitable operation errors. Furthermore, the error control scheme employed in the curve fitting for image contours ensures that the reconstructed geometry can be close to the real middle ear structure within a prescribed error range. The accuracy of the proposed method has been demonstrated, as shown in Table 4.1.

This method is systematic. As presented in Figure 4.1, this method follows a prescribed procedure. The standardized procedure makes the method easy to follow and eliminates potential inconsistency and mistakes. In addition, the required software tools are operating system independent and less demanding on computing resources. The computing environment can be easily created to support the modeling work using the proposed method.

The proposed method is low cost, as compared with possible alternatives such as CT, MRI or laser scans with comparable accuracy. The laboratory setup that is required

for supporting temporal bone slide preparations, as described in stage 1 of Figure 1, is very common in any bioengineering laboratory. A regular scanner, HP ScanJet Scanner [Hewlett-Packard], was employed for scanning the slide images into computer with required accuracy and resolutions. Software tools that support imaging process, image digitizing, and geometric modeling are industrial standard, off-the-shell tools. The only special tool employed in the method is the curve fitting and surface skinning that is developed separately by our research team.

Most importantly, the proposed method is general. It is applicable to structures with complicate geometry, various topology, and different physical sizes. This method works especially well with small-size structure and complicate geometry like the human middle ear.

Furthermore, the method opens up many research possibilities that require further anatomic and pathologic information about the function of complex and tiny biostructures. The solid geometric model of human middle ear has been proven to be a good basis for finite element analysis of human middle ear. It also provides a possible way to fabricate the middle ear prostheses with accurate geometry, as shown in the physical model in section 4.5.

CHAPTER FIVE

COMPUTER INTEGRATED FINITE ELEMENT

MODELING OF HUMAN MIDDLE EAR

In this chapter, a procedure of constructing the FE model of the middle ear is presented. The finite element mesh of the middle ear was first generated based on the refined middle ear solid model obtained from Chapter 4. Then the material properties were assigned to individual parts of the system. Most material properties came from published data as reviewed in Chapter 3. The remaining material properties were assumed partially based on engineering reasoning, partially through the modeling practice in Chapter 3 and partially by the FE model calibration process. The finalized FE model was verified by comparing the FE model prediction with published experimental measurements. The objective is to construct a FE model as the base-line FE model for clinical-related applications. The FE model includes malleus, incus, stapes, eardrum, joints, ligaments, muscles and cochlear impedance. The middle ear cavity was not included in this model because it is shown that the middle ear cavity does not contribute significantly to the normal middle ear mechanics [Vlaming and Feenstra 1986]. In other words, the "acoustic coupling" is assumed not playing a significant role in sound transmission in normal middle ear. And this assumption is also consistent to an experimental setup, in which the middle ear cavity is open.

5.1 Mesh Generation For The Middle Ear FE Model

To prepare for the finite element analysis of middle ear mechanics, all surfaces of the refined solid model were translated into HyperMesh via ACIS format [Spatial Corp.]. The surfaces translated into HyperMesh are shown in Figure 5.1. Based on these surfaces, the finite element mesh of the middle ear was created by means of both automatic and manual meshing capabilities in HyperMesh. A total of 1,746 3-noded triangular and 4-noded quadrilateral shell elements (SHELL 63) were created to mesh the eardrum, which yielded a resolution of 25 elements/mm^2 in average. The mesh of eardrum includes 1,561 nodes with 9,366 degrees of freedom. Surrounding the eardrum periphery, the tympanic ring was meshed using 113 3-noded triangular and 4-noded quadrilateral shell elements. There were 812 8-noded hexahedral, 6-noded pentahedral and 4-noded tetrahedral solid elements (SOLID 45) created to mesh ossicles, joints, ligaments and muscles with an

(a) Anterior View   (b) Isometric View
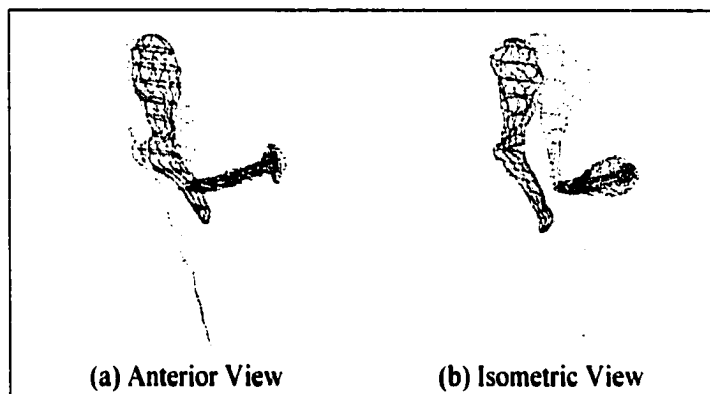
Figure 5.1 Surface model of human middle ear in HyperMesh

average resolution of 45 elements/mm^3. The total number of nodes was 1,497, and therefore the total number of degrees of freedom was 4,491. Lying in the stapes footplate plane, there were 25 spring elements (COMBIN 14) employed to model the stapedius

94

annular ligament. A total of 49 spring-damper elements perpendicular to the footplate plane were employed to model the cochlear fluid. The size of the model is adequate for an accurate FE analysis with a reasonable computation time. Figure 5.2 (a), (b) and (c) show the middle ear FE mesh in anterior, superior and isometric view, respectively.
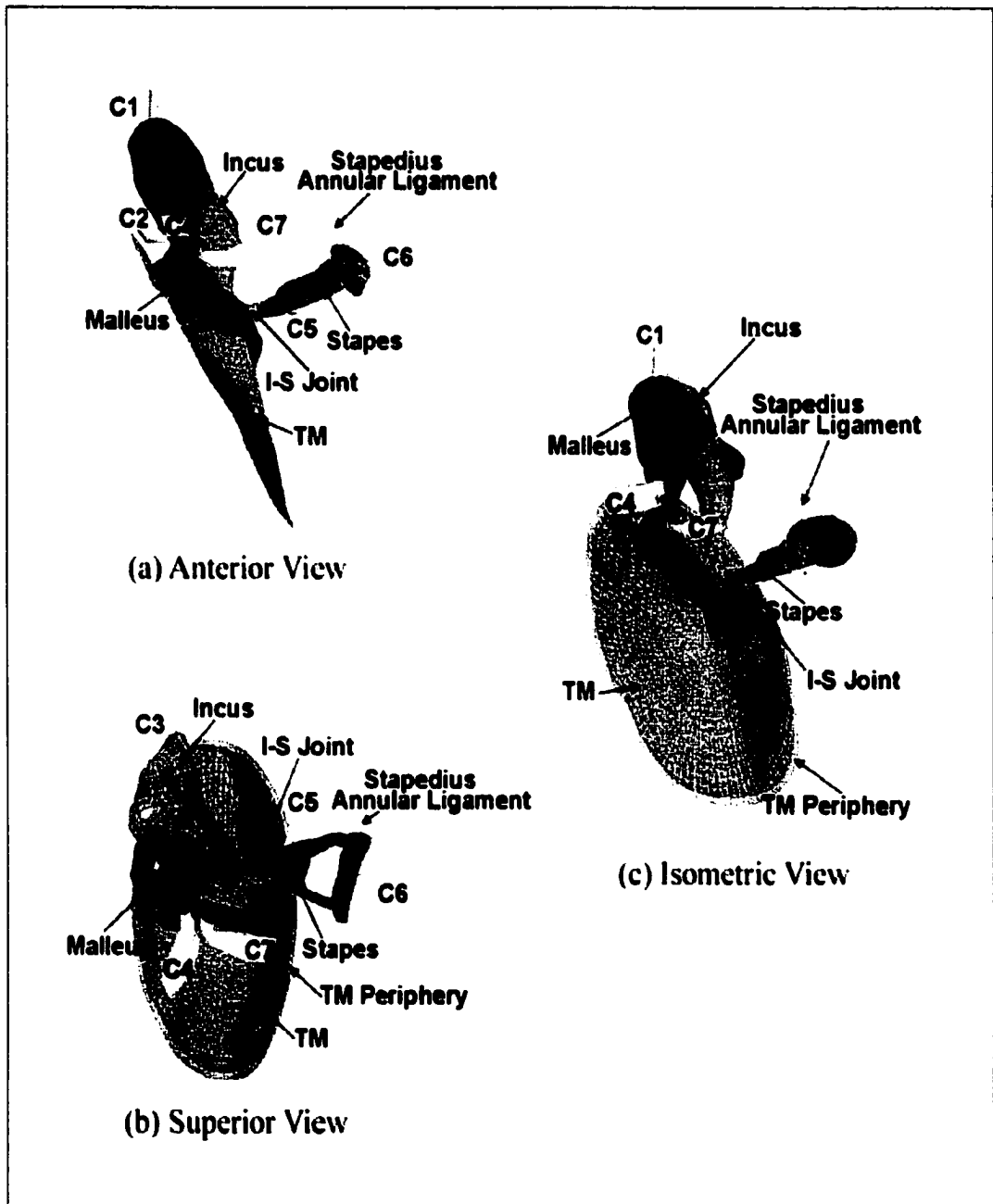
Figure 5.2 Finite element mesh of human middle ear

5.2 FE Modeling Considerations

The anatomy and functions of the middle ear discussed in Section 3.1 were incorporated into the FE modeling. The modeling considerations were realized in the FE model by assigning different material properties to different parts of the middle ear system. Most material properties came from published data reviewed in Chapter 3. The remaining material properties were assumed partially based on engineering reasoning, partially through the modeling practice in Chapter 3 and partially by the FE model calibration process.

The Poisson's ratio was assumed 0.3 for all materials of the middle ear system based on the fact that all published Poisson's ratios are close to this value. In addition, there is no evidence showing significant effects of Poisson's ratio on dynamic behaviors of the middle ear system [Funnell & Laszlo 1982]. The published stiffness and density were used for main components of the middle ear, including malleus, incus, stapes and eardrum. Ligaments, muscles, malleus attachment on the eardrum, incudostapedial joint and tympanic ring were assumed the same density as that of the eardrum. Five of six ligaments and muscles, including superior malleus and incus ligaments, lateral malleus, posterior incus, the posterior stapedial muscle and the tensor tympani muscle, and incudostapedial joint were assigned the published stiffness data. The stiffness of incudomalleolar joint was assumed by reasoning based on the published experimental observations. The stiffness of the anterior malleus ligament (C4 in Figure 5.2) and the tympanic ring were adjusted and finalized by the FE model calibration process, as described in Chapter 3. The damping coefficients for all the parts of the middle ear system were selected based on the study of the simple model presented in Chapter 3.

The detailed modeling considerations incorporated for the main middle ear

components, joints, attachment, ligaments, muscles and tympanic ring are introduced in

the following subsections.

5.2.1 Material Properties Of Middle Ear Components

Eardrum

The eardrum ultrastructure study [Lim 1968 & 1970; Shimada and Lim 1971] shows the regularity

of the radial and circumferential fibers appearing in the pars tensa. The analytical studies

by Rabbitt and Holmes [Rabbitt and Holmes 1986] also indicate the importance of anisotropic

material properties of the eardrum. The eardrum in this FE model was modeled as a linear

elastic shell structure with homogeneous and orthotropic material properties. The shell

element (SHELL 63) was employed instead of the membrane element (SHELL 41) so

that the elastic support effect of the eardrum periphery could be incorporated (unlike the

problem encountered in the simple model in Chapter 3). Based on the review of Section

3.3, the material of the eardrum was assumed to have circumferential Young's modulus

of $2.0 \times 10^7 \, N/m^2$ in the pars tensa and $1.0 \times 10^7 \, N/m^2$ in the parsa flaccida, and radial

Young's modulus of $3.2 \times 10^7 \, N/m^2$ in the pars tensa and $1.0 \times 10^7 \, N/m^2$ in the pars

flaccida, respectively. The annular ligament, which divides the eardrum into pars tensa

and pars flaccida, was assumed to have the same Young's modulus as the pars tensa. The

consideration reflects the ultrastructural chacteristics of the eardrum [Anson and Donaldson 1981;

Rabbitt and Holmes 1986], as shown in Figure 5.3. The thickness varied in accordance with the

eardrum geometry obtained in the CAD solid model.
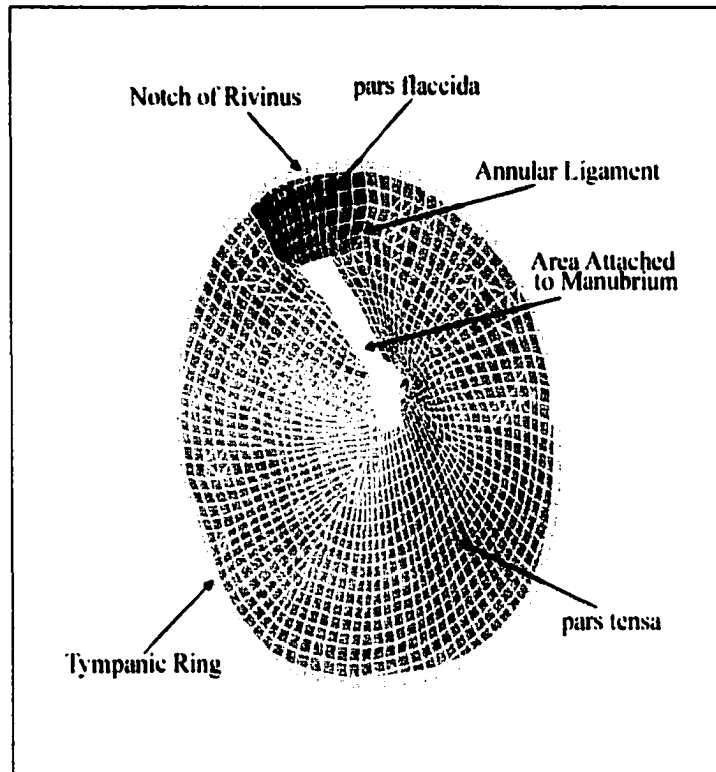
Figure 5.3 Eardrum FE model in medial view

Ossicles

The ossicles were modeled as linear elastic and isotropic structure. The homogenous

Young's modulus $1.4 \times 10^{10} \, N/m^2$ was employed. Based on the work of Kirikae [Kirikae

1960], the mass densities varied in different portions of the ossicles, which are listed in

Table 3.2. Although some research shows that there exists certain relationship between

the Young's modulus of a material and its density, the relation was not considered in this

research due to lack of experimental data.

Malleus Attachment on the Eardrum

The malleus attachment on the eardrum, as shown in Figure 5.4, was modeled as

linear elastic, homogeneous and isotropic hard tissue. The attachment is softer than
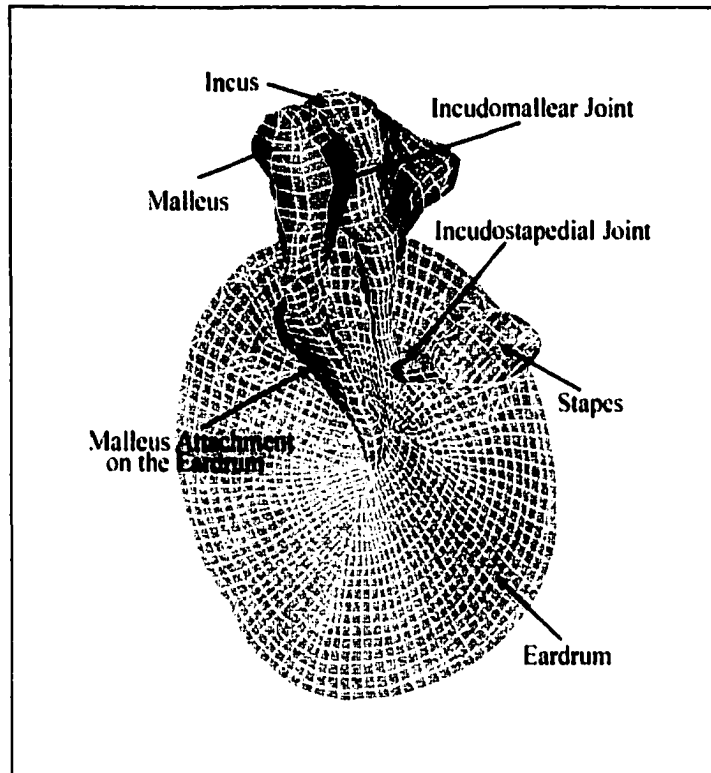
Figure 5.4 Malleus attachment on the eardrum,
incudomalleolar joint and incudostapedial joint

ossicles because the manubrium is not tightly attached to eardrum in human temporal

bone [Graham et al. 1978]. Therefore, Young's modulus of the attachment was assumed one

third of that of the ossicles to simulate the "softer" effect.

Incudomalleolar Joint

The incudomalleolar joint is shown in Figure 5.4. Studies on auditory physiology and

sound transmission through human ear have suggested that the incudomalleolar joint is

relatively rigid at physiological sound pressure levels for frequencies below 3000 Hz

[Guinan and Peake 1967; Vlaming 1987]. This means that there is no relative motion between malleus

and incus in the low frequency range. It may not be the case in the high frequency range

or high sound pressure amplitude. Therefore, the incudomalleolar joint was modeled as

homogeneous and isotropic hard tissue with a Young's modulus identical to the ossicles.

Incudostapedial Joint

The incudostapedial joint, as shown in Figure 5.4, appears to be non-rigid [Hüttenbrink 1988]. That is, there is a relative motion between incus and stapes. So the joint was modeled as homogeneous and isotropic ligamentous tissue [Ferris & Prendergast 2000]. The Young's modulus was assumed as $6.0 \times 10^5 \, N/m^2$, which was reported by Wada et al. [Wada et al. 1996].

The damping coefficients for all the middle ear components were assumed to be $\alpha = 0 \, s^{-1}, \beta = 0.0001 \, s$, based on the study of the simple model in Chapter 3. The malleus attachment on the eardrum, incudomalleolar joint and incudostapedial joint, which consist of the solid elements as described in Section 5.1, connect malleus and eardrum, malleus and incus, and incus and stapes by coupling the corresponding finite element nodes among them. The material data used for the middle ear FE model and their sources are summarized in Table 5.1.

5.2.2 Boundary Conditions

Figure 5.2 illustrates the boundary conditions employed in the FE model. As shown in this figure, three ossicles (malleus, incus, and stapes) were held at the eardrum by the malleus, and at the oval window by the stapes footplate. The ossicles were also supported by suspensory ligaments and intra-aural muscles. Four major suspensory ligaments (superior malleus and incus, lateral malleus, posterior incus, and anterior malleus), the posterior stapedial muscle and the tensor tympani muscle were regarded as elastic

Table 5.1 Material properties of middle ear components used for the FE model

EARDRUM	Data Used for FE Model	Source
Density (kg/m³)	1.2×10³	Williams et al. 1990 Wada et al. 1990, 1992, Beer et al. 1996 Ferris et al. 2000,
Young's Modulus (N/m²) pars tensa pars flaccida	 2.0×10⁷ (circumferential) 3.2×10⁷ (radial) 1.0×10⁷ (circumferential) 1.0×10⁷ (radial)	 Beer et al. 1996 Prendergast, Ferris et al. 1999
Damping	α=0 s⁻¹, β=0.0001 s	Chapter 3 of this dissertation
MALLEUS		
Density (kg/m³)	2.55×10³ (for head) 4.53×10³ (for neck) 3.70×10³ (for handle)	Kirikae et al. 1960, Wada et al. 1992
Young's Modulus (N/m²)	1.41×10¹⁰	Kirikae et al. 1960, Herrmann et al. 1972 Koike 1996, Wada et al. 1992, 1996 Prendergast et al. 1999
INCUS		
Density (kg/m³)	2.36×10³ (for body) 2.26×10³ (for short process) 5.08×10³ (for long process)	Kirikae et al. 1960, Wada et al. 1992
Young's Modulus (N/m²)	1.41×10¹⁰	Kirikae et al. 1960, Herrmann et al. 1972 Koike 1996, Wada et al. 1992, 1996 Prendergast et al. 1999
Damping	α=0 s⁻¹, β=0.0001 s	Chapter 3 of this dissertation
STAPES		
Density (kg/m³)	2.20×10³	Kirikae 1960
Young' Modulus (N/m²)	1.41×10¹⁰	Kirikae et al. 1960, Herrmann et al. 1972 Koike 1996, Wada et al. 1992, 1996 Prendergast et al. 1999
Damping	α=0 s⁻¹, β=0.0001 s	Chapter 3 of this dissertation
INCUDOMALLEOLAR JOINT		
Density (kg/m³)	3.2×10³	
Young's Modulus (N/m²)	1.41×10¹⁰	
Damping	α=0 s⁻¹, β=0.0001 s	Chapter 3 of this dissertation
INCUDOSTAPEDIAL JOINT		
Density (kg/m³)	1.2×10³	
Young's Modulus (N/m²)	6.0×10⁵ N/m²	Wada et al. 1996, Prendergast 1999 Ferris et al. 2000
Damping	α=0 s⁻¹, β=0.0001 s	Chapter 3 of this dissertation
MALLEUS ATTACHMENT ON THE EARDRUM		
Density (kg/m³)	1.0×10³	
Young's Modulus (N/m²)	4.7×10¹⁰	
Damping	α=0 s⁻¹, β=0.0001 s	Chapter 3 of this dissertation

constraints, C1~C5, C7, respectively. The tympanic ring was modeled as an elastic ring that connects the eardrum periphery and the bony wall of the ear canal. The cochlear fluid was assumed a viscoelastic constraint, C6. The detailed modeling considerations are described as follows.

Ligaments and Muscles

The ligaments and muscles, including the superior, anterior and lateral ligaments of malleus, the posterior ligament of incus, the tensor tympani muscle, the posterior stapedial muscle, (shown in Figure 5.2) were modeled as homogeneous, isotropic ligamentous tissue using solid elements as described in Section 5.1. As listed in Table 5.2, the Young's moduli of all ligaments and muscles were chosen based on the review in Section 3.3 except the anterior mallear ligament (C4 in Figure 5.2). The published Young's modulus for the anterior mallear ligament was not used in the FE model because it differs significantly from rest of the ligaments. The consideration was based on the assumption that the materials having similar histological structures should have similar mechanical properties. The value of C4's Young's modulus was adjusted and finalized through the FE model calibration process. The damping parameters for all ligaments and muscles were assumed to be $\alpha = 0\ s^{-1}, \beta = 0.0001\ s$ based on the study of the simple model in Chapter 3. Each ligament or muscle was attached to the ossicles by coupling corresponding finite element nodes among them at one end, and fixed at the other.

Table 5.2 Initial boundary conditions used for the FE model

	Young's Modulus or Spring Constant	Damping
Superior mallear ligament (C1)	4.9×10^4 N/m^2 (Beer et al. 1996)	$\alpha = 0\ s^{-1},\ \beta = 0.0001\ s$
Lateral mallear ligament (C2)	6.7×10^4 N/m^2 (Beer et al. 1996)	
Posterior incudal ligament (C3)	6.5×10^5 N/m^2 (Wada et al. 1996, Prendergast et al. 1999, Ferris et al. 2000)	
Anterior mallear ligament (C4)	2.1×10^7 N/m^2 (Wada et al. 1996, Prendergast et al. 1999, Ferris et al. 2000)	
Posterior stapedial muscle (C5)	5.2×10^5 N/m^2 (Wada et al. 1996, Prendergast et al. 1999, Ferris et al. 2000)	
Tensor tympani muscle (C7)	2.6×10^6 N/m^2 (Wada et al. 1996, Prendergast et al. 1999)	
Cochlear fluid (C6)	60 N/m (Chapter 3 of this dissertation)	0.054 N-s/m
Stapedius annular ligament	9 N/m (Converted from Lynch et al. 1982)	0 N-s/m
Tympanic ring	3.2×10^7 N/m^2	$\alpha = 0\ s^{-1},\ \beta = 0.0001\ s$

Tympanic Ring

To simulate the flexible support at the eardrum periphery [Lim 1970], the tympanic ring was modeled as an elastic ring of 0.2 *mm* width and 0.2 *mm* thick using shell elements, as described in Section 5.1. The ring was connected to the eardrum periphery at the inner edge by coupling corresponding nodes and was constrained against translational movements at the outer edge, as shown in Figure 5.3. The constraint consideration was based on Williams *et al.*'s study [Williams *et al.* 1996b]. The Young's modulus was initially assumed identical to the eardrum, and then adjusted in the FE model calibration process. To consider the effect of the missing part of the ring, notch of Rivinus, the Young's modulus of the part corresponding to the notch of Rivinus, was assumed one third of that of the ring. The damping coefficients for the tympanic ring were assumed to be identical to the eardrum.

Stapedius Annular Ligament

The in-plane stiffness action on the stapes footplate due to the stapedius annular ligament was represented by 25 linear spring elements distributed evenly around the side periphery of the footplate, as shown in Figure 5.5. These springs are perpendicular to the side periphery of the footplate. Each spring was attached to the corresponding node of the side periphery of the footplate at one end, and fixed at the other, to simulate the attachment to the margin of vestibular fenestra. The arrangement replicates the fact that the stapedius annular ligament restrains mainly against in-plane motion of the footplate. The out-of-plane stiffness was combined into the consideration for the stiffness induced by the cochlear impedance. Assuming that the material of the stapedius annular ligament
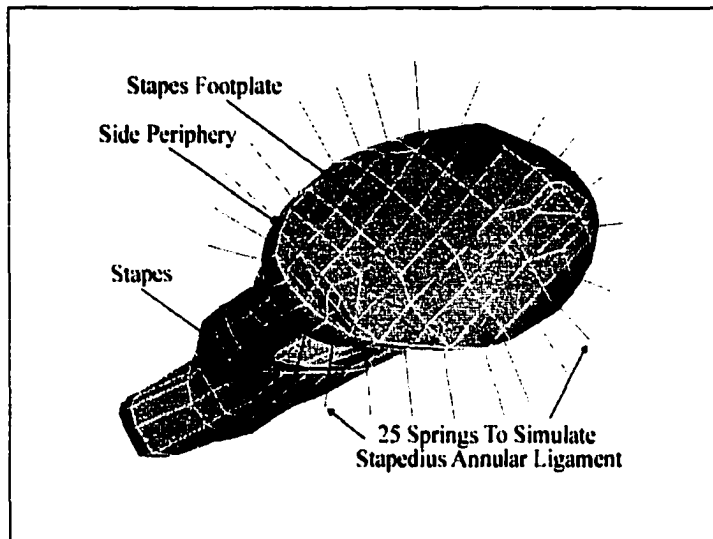
Figure 5.5 Stapedius annular ligament

is homogenous, isotropic and uniformly distributed surrounding the side periphery, Lynch et $al.$ estimated the Young's modulus of the stapedius annular ligament to be $1.0 \times 10^4 \, N/m^2$ [Lynch et $al.$ 1982]. Based on Lynch et $al.$'s assumption, the stapedius annular ligament can be considered as a slab surrounding the side periphery of the footplate. The thickness of the slab was estimated as $0.05 \, mm$ by measuring the average space between the side periphery of the footplate and the wall of the oval window on the histological sections of human temporal bone. The area of the side periphery of the footplate was measured as $1.275 \, mm^2$ using the middle ear FE model. If the slab is uniformly divided into 25 segments along the side periphery of the footplate, then each segment can be treated as a bar element perpendicular to the periphery of the footplate. Therefore, each bar has a cross-section area of $0.051 \, mm^2$ and a length of $0.05 \, mm$. Based on the discussion above, the spring constant for each spring was estimated as $9.0 \, N/m$.

Cochlear Fluid Impedance

Some researchers considered cochlear fluid impedance to be resistive and expressed it as a viscous damping [Wada et al. 1996; Ferris et al. 2000] in their FE models. The damping coefficients were estimated using the acoustic input impedance of the cochlea that was calculated from measurements of the stapes displacements. In another paper, Wada et al. modeled the cochlear impedance as a set of springs perpendicular to the plane of the footplate [Wada et al. 1992]. However, they did not give the spring constant for normal ears. In Funnell et al. and Ladak et al.'s FE models, the action of cochlear fluid and stapedial annular ligament on the stapes footplate was also considered as stiffness perpendicular to the plane of the footplate [Funnell et al. 1978; Ladak et al. 1996]. The stiffness was estimated at a specific frequency using the acoustic impedance or acoustic compliance of the cochlea that were calculated from measurements. In our FE model, the action of the cochlear fluid on the stapes footplate was modeled as a set of 49 linear springs with dashpots (damping) distributed on the footplate, as shown in Figure 5.6. Note that these springs and dashpots are oriented in the normal direction of the footplate plane.
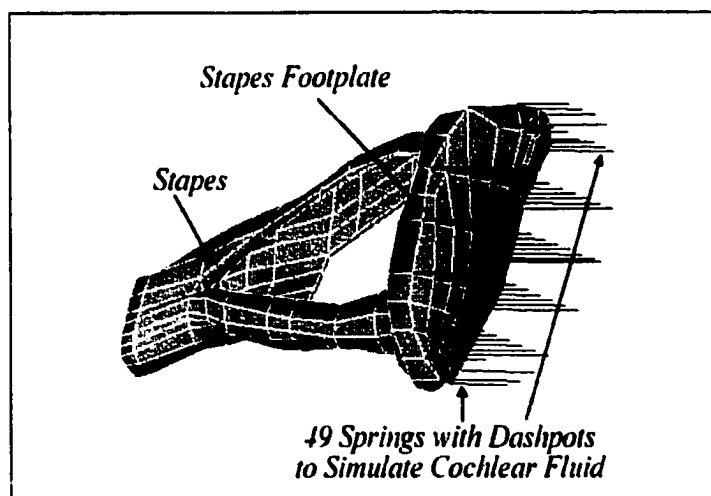
Figure 5.6 Cochlear fluid

In order to understand how to estimate the total damping coefficient and stiffness of the cochlea from the published acoustic impedance data, we consider that the cochlea is uncoiled and is simplified as shown in Figure 5.7 (a). The cochlea appears as a tapered cylinder divided into two sections, scala vestibuli and scala tympani, by basilar membrane. Note that we ignore the cochlear duct because it is quite thin compared to the scala vestibuli and scala tympani. At the larger end of the cylinder are the oval window and the round window, each of which is closed by a thin membrane. Near the far end of the basilar membrane is a small hole called the helicotrma connecting the two sections. Therefore, the fluid in scala vestibuli and scala tympani can be simplified as a one dimensional mechanical system that consists of a mass block with mass m, a spring with spring constant k and a dashpot with damping coefficient c, as shown in Figure 5.7 (b). When the system is stimulated by a sinusoidal force F, the equation of motion of the system is

| (a) Uncoiled and Simplified Cochlea | (b) One Dimensional Mechanical Model |
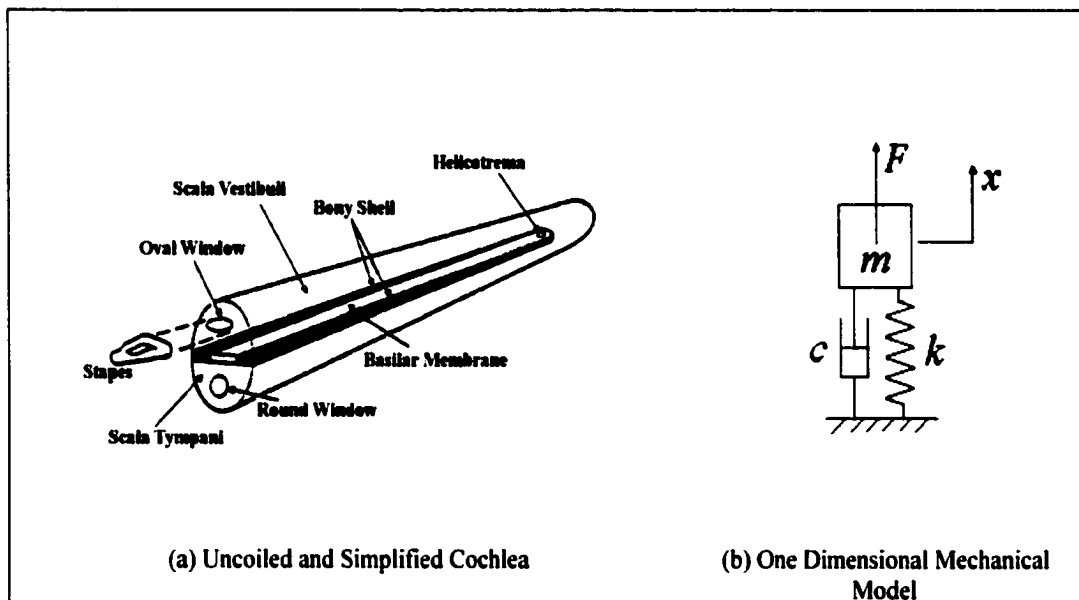
Figure 5.7 Uncoiled cochlea and one dimensional mechanical model of cochlear fluid

$$m\ddot{x} + c\dot{x} + kx = F \qquad (5.1)$$

Since F is a sinusoidal function, then the displacement x can be expressed as

$$x = Xe^{i\omega t} \qquad (5.2)$$

where $i = \sqrt{-1}$, ω is the angular frequency and X is the amplitude of the displacement x. Therefore, we have

$$x = -i\dot{x}/\omega \quad , \quad \ddot{x} = i\omega\dot{x} \qquad (5.3)$$

By substituting Eq.(5.3) into Eq.(5.1), the mechanical impedance of the system, Z_m, can be obtained as

$$Z_m = F/\dot{x} = c + i(\omega m - k/\omega) \qquad (5.4)$$

Assuming the area of stapes footplate is A and the pressure is uniform over the stapes footplate, then the volume velocity of the cochlea is $\dot{x}A$ and the pressure is F/A. Based on the definition of the acoustic impedance Z_a, which is the pressure divided by volume velocity, we have

$$Z_a = \frac{F/A}{\dot{x}A} = \frac{c + i(\omega m - k/\omega)}{A^2} \qquad (5.5)$$

Therefore the magnitude $|Z_a|$ and phase angle $\angle Z_a$ of the acoustic impedance are respectively obtained as

$$|Z_a| = \frac{1}{A^2}\sqrt{c^2 + (\omega m - k/\omega)^2} \quad , \quad \angle Z_a = \tan^{-1}\frac{\omega m - k/\omega}{c} \qquad (5.6)$$

Solving Eq.(5.6) gives

$$c = A^2|Z_a| \bullet |\cos \angle Z_a| \quad , \quad k = \omega(\omega m\text{-}c\tan\angle Z_a) \qquad (5.7)$$

where $\omega = 2\pi f$ and f is the frequency. The mass m can be estimated by halving the total mass of the fluid in scala vestibuli and scala tympani. The k and c can be determined

using the cochlear input impedance curves obtained experimentally [Aibara et al. 2000].

Igarashi et al.'s study shows that the volume of scala vestibuli and scala tympani are respectively $3.15 \times 10^{-8} m^3$ and $4.43 \times 10^{-8} m^3$ [Igarashi et al. 1986]. Assume the density of the fluid to be the same as the density of water, i.e., $1 \times 10^3 kg/m^3$; then we can estimate $m = 3.79 \times 10^{-5} kg$. From our middle ear model, we have $A = 2.91 \times 10^{-6} m^2$. The mean experimental curves of the cochlea input impedance published by Aibara et al., as shown in Figure 5.8 [Aibara et al. 2000], were employed to estimate the stiffness and damping coefficient from Eq.(5.7).
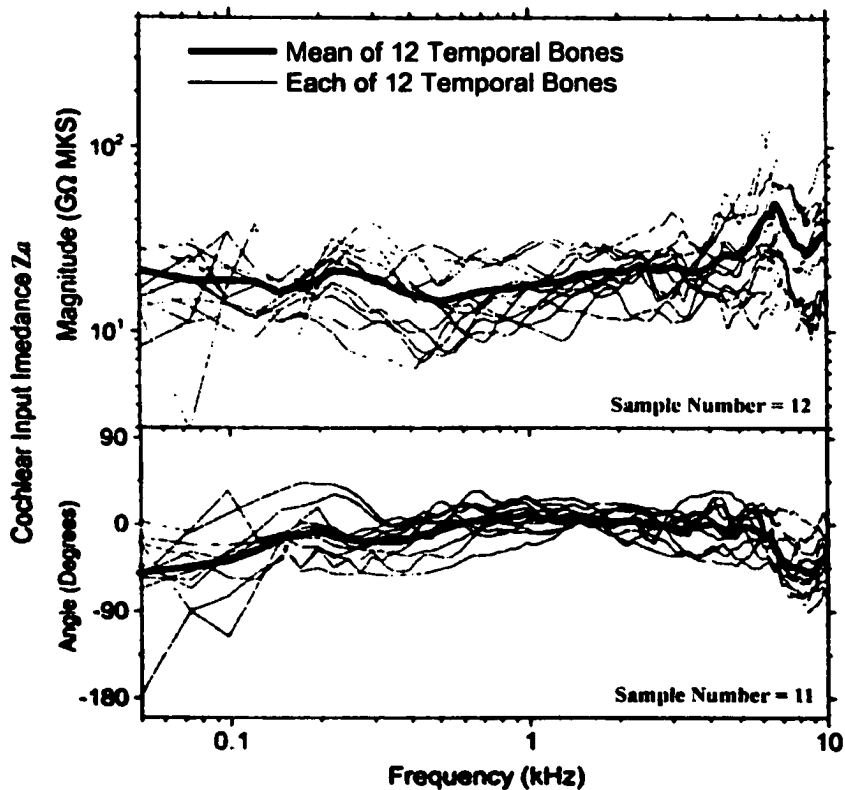
Figure 5.8 Human cochlear input impedance obtained by Aibara et al. 2000

The estimated spring constant and damping coefficient as function of frequency are plotted in Figures 5.9 (a) and (b). These results show that the spring constant and damping coefficient are dependent on frequencies. In other words, we cannot estimate a set of actural values for k and c using the experimental cochlear input acoustic impedance data. Therefore the previously published data for k and c cannot be adopted in our FE model. In our FE model, the initial total stiffness of 49 springs was assumed as 60 N/m and the initial total damping coefficient of 49 dashpots was taken to 0.054 $N\text{-}s/m$ based on the study of the simple model in Chapter 3. The final values for the two parameters were determined by the model calibration process, described in the following section. We will see that the final values determined by the model calibration process are the same as the initial values.

When all these modeling considerations were incorporated, the initial FE model of the middle ear was built.
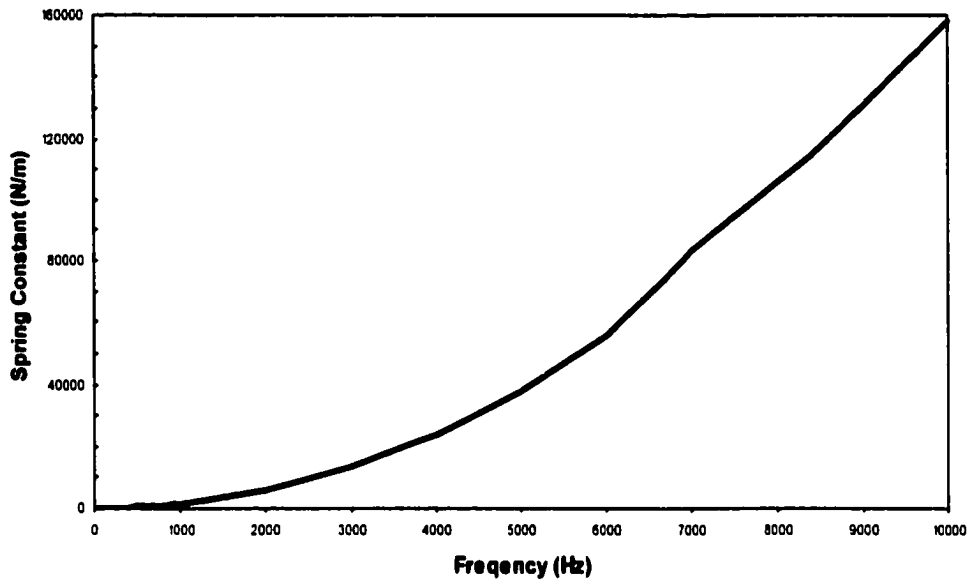
(a) Spring constant
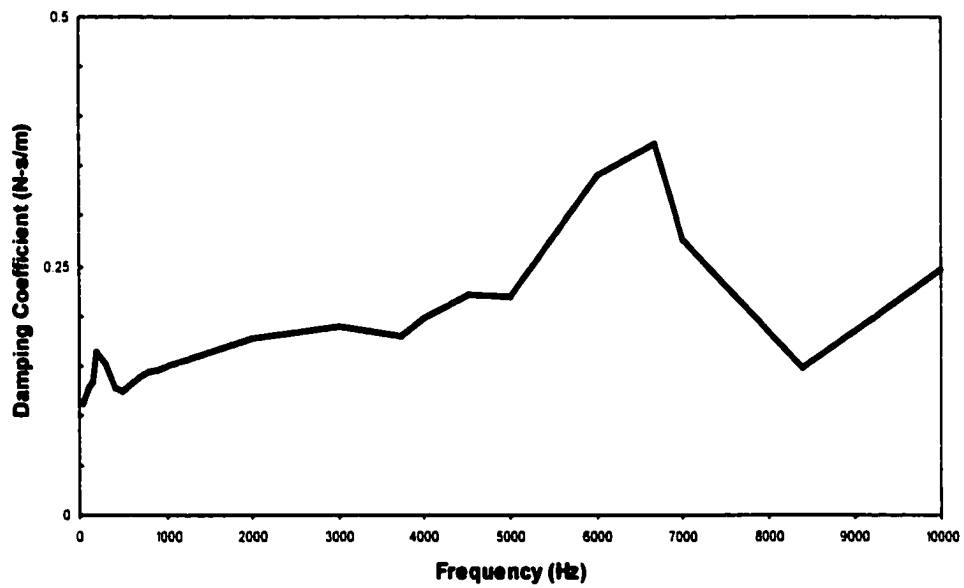
(b) Damping coefficient

Figure 5.9 Spring constant and damping coefficient in one dimensional mechanical model of cochlea derived from Aibara *et al.* 2000

5.3 FE Model Parameter Determination

According to the discussions in Section 5.2, the mechanical properties of main components of the middle ear have been assigned mainly based on the published data, partially based on published experimental observations and partially based on the practice of the simple model. These data are listed in Table 5.1. Most of the boundary conditions also have been assumed based on the published data and the practice of the simple model. There are only four model parameters that need to be determined. They are the Young's moduli of anterior mallear ligament and tympanic ring, as well as the stiffness and damping coefficient of cochlear fluid. These four parameters were determined using the FE model calibration process as described in Chapter 3.

The experimental measurements published by Gan *et al.* [Gan *et al.* 2001] were used to derive the four undetermined parameters following the FE model calibration process and are exactly the same as those used for the simple model calibration. The measured mean peak-to-peak displacement of the stapes footplate on seventeen normal fresh-frozen, cadaveric temporal bones was employed to calibrate the FE model. To be consistent with the experimental setup, a uniform pressure of 90 dB SPL (0.632 N/m^2) was applied to the lateral side of the eardrum in the initial FE model. The harmonic analysis was conducted on the FE model across the frequency range of 250-8,000 Hz. The displacements of the stapes footplate in the frequency field were collected and converted to peak-to-peak displacement response of the stapes footplate. The objective of the calibration process is to adjust the FE model prediction using the experimental curve obtained by the LDI measurement as close as possible. Through the process, the model parameters related to

the boundary conditions were finalized as listed in Table 5.3. The FE model with model parameters listed in Tables 5.1 and 5.3 is called the base-line FE model of the middle ear.

Table 5.3 Boundary conditions used for the FE model

	Young's Modulus or Spring Constant	Damping
Superior mallear ligament (C1)	4.9×10^4 N/m² (Beer *et al*. 1996)	α=0 s⁻¹,β=0.0001 s
Lateral mallear ligament (C2)	6.7×10^4 N/m² (Beer *et al*. 1996)	
Posterior incudal ligament (C3)	6.5×10^5 N/m² (Wada *et al*. 1996, Prendergast *et al*. 1999, Ferris *et al*. 2000)	
Anterior mallear ligament (C4)	2.1×10^6 N/m² (Determined by FE model calibration process)	
Posterior stapedial muscle (C5)	5.2×10^5 N/m² (Wada *et al*. 1996, Prendergast *et al*. 1999, Ferris *et al*. 2000)	
Tensor tympani muscle (C7)	2.6×10^6 N/m² (Wada *et al*. 1996, Prendergast *et al*. 1999)	
Cochlear fluid (C6)	60 N/m (Determined by FE model calibration process)	0.054 N-s/m
Stapedius annular ligament	9 N/m (Converted from Lynch *et al*. 1982)	0 N-s/m
Tympanic ring	6.0×10^5 N/m² (Determined by FE model calibration process)	α=0 s⁻¹,β=0.0001 s

The displacement magnitude at the stapes footplate obtained using the base-line FE model was plotted together with the seventeen experimental curves in Figure 5.10. The figure shows that the model-predicted stapes displacement curve falls between the
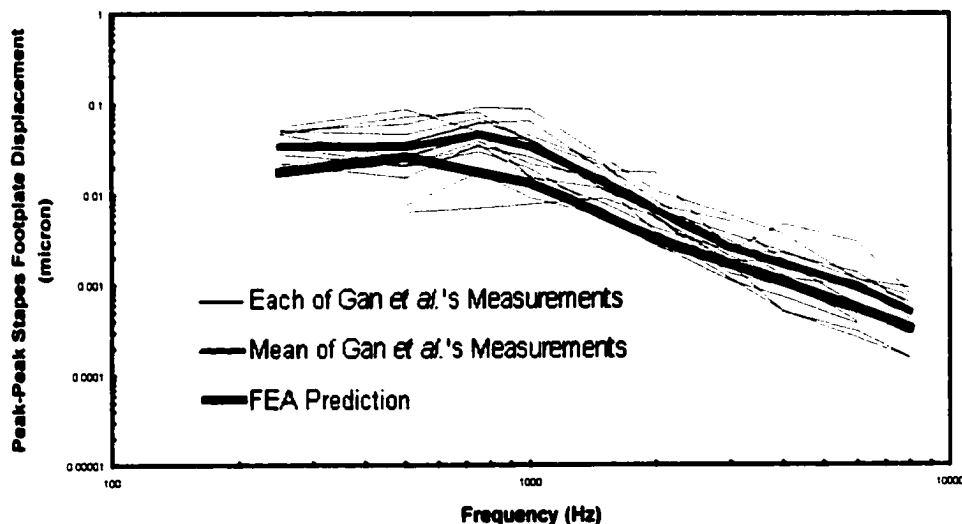
Figure 5.10 Comparison of stapes footplate displacements between prediction and Gan *et al*. experimental measurements (2001)

112

maximum and minimum of the 17 experimental curves. The predicted curve is lower than the mean experimental curve, especially in the frequency range of 700~2,000 Hz. There is a 1.92-fold difference in average between them. However, the trend is similar to the mean curve obtained experimentally across the frequency range of 250-8,000 Hz. The difference may come from the significant variations of individual temporal bones. The possible reasons to produce the difference will be discussed in section 5.4.

5.4 FE Model Verifications

In order to verify the accuracy of the base-line FE model, four independent experimental results were employed. These experimental data include: (1) the magnitude of the umbo displacement as a function of frequency measured by Nishihara et al. [Nishihara et al. 1996], (2) the stapes velocity transfer function published by Aibara et al. [Aibara et al. 2000], (3) the ratio of the umbo displacement to that of the stapes footplate converted from the measurements of Nishihara et al. [Nishihara et al. 1993], and (4) the ratio of the umbo displacement to that of the malleus short process converted from the measurements of Goode et al. [Goode et al. 1994].

5.4.1 Comparison Of Frequency Response Of The Umbo Displacement

The experimental data from 64 normal ears were selected for the comparison. The data are part of the experimental results published by Nishihara et al. [Nishihara et al. 1996]. In their work, 99 ears of fifty-two human subjects (age 14 to 88 years, 31 males and 21 females) were used. In experiments, a small piece of reflective tape was placed on subject's umbo to serve as a laser-reflective target. When each of the thirty-four pure tone sounds of 80 dB SPL were delivered to the eardrum, the umbo displacement induced by the sound pressure on the eardrum was measured across the frequency range of 195-19,433 Hz. The measurements were performed using a laser Doppler interferometer by focusing the laser beam on the target placed at the umbo. The measured peak-to-peak displacements at the umbo on the sixty-four ears were employed to verify the base-line model.

114

To be consistent with the experimental setup, a uniform harmonic pressure stimulus

of 80 dB SPL (0.2 N/m^2) at the lateral side of the eardrum was applied to the FE model.

The harmonic analysis was conducted on the base-line FE model across the frequency

range of 250-8,000 Hz. The umbo displacements in frequency field were collected and

converted to peak-to-peak displacement response curve. The curve was plotted together

with the mean and the upper and lower bounds of the sixty-four experimental curves, as

shown in Figure 5.11. The comparison shows that the model-predicted umbo

displacements are within the bounds of the sixty-four experimental curves across the

frequency range of 250-8,000 Hz. It is noticed that the FEA prediction is close to the

lower bound of the experimental results, which is consistent to the case of the stapes

footplate displacement in comparison with Gan *et al.*'s results.
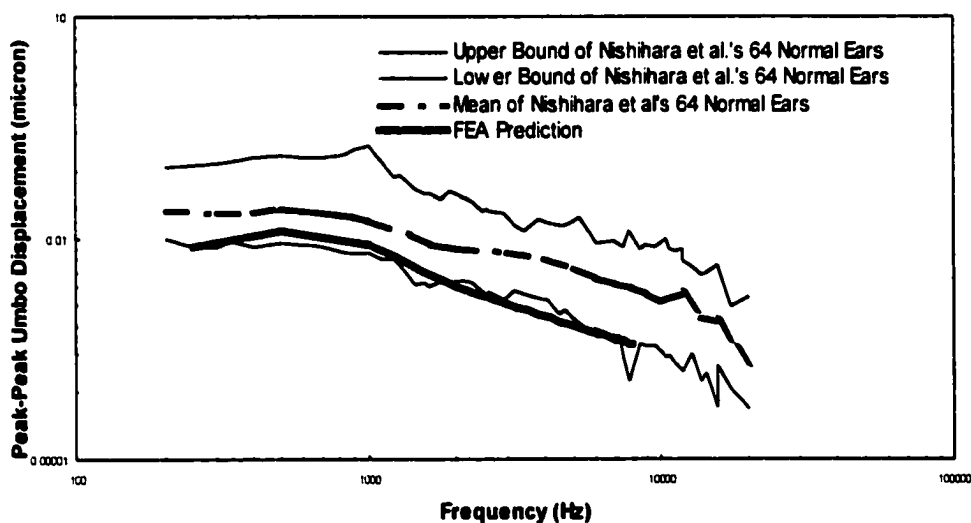

Figure 5.11 Comparison of umbo displacement between FEA prediction
and Nishihara *et al.* experimental measurements (1996)

5.4.2 Comparison Of Human Middle Ear Sound Transfer Function

The ratio of the footplate velocity to the pressure at ear canal is termed as the ear canal sound pressure to the stapes footplate velocity transfer function (STF). In this comparison, the STF curves reported by Aibara *et al.* were employed to verify our base-line model [Aibara *et al.* 2000]. The experimental measurements were conducted on twelve normal fresh temporal bones (age 36-81 years, 9 males and 3 females). When a pure tone sound of 90~120 dB SPL was delivered to the eardrum, the stapes footplate velocities caused by the sound pressure on the eardrum was measured across the frequency range of 50-10,000 Hz. The measurements were performed using a laser Doppler interferometer by aiming the laser beam on a small reflective tape on the center of the stapes footplate. Sound pressure in the ear canal was measured near the eardrum using a probe-tube microphone. The STF's were calculated based on the measurements.

Because of the linear characteristics of the FE model, the ratio of the stapes footplate velocity to the pressure at ear canal does not depend on the magnitude of the sound pressure applied to the eardrum. Therefore, a uniform pressure of 90 dB SPL (0.632 N/m^2) on the lateral side of the eardrum was applied to the base-line model. A harmonic analysis was conducted on the base-line model across the frequency range of 250-8,000 Hz. The stapes footplate velocities in the frequency field were collected and converted to the STF, which was plotted together with the mean and the upper and lower bounds of the eleven experimental curves, as shown in Figure 5.12. This figure shows that the model-predicted STF curve lies close to the lower bound of the experimental curves. Again, it is consistent to previous observations.
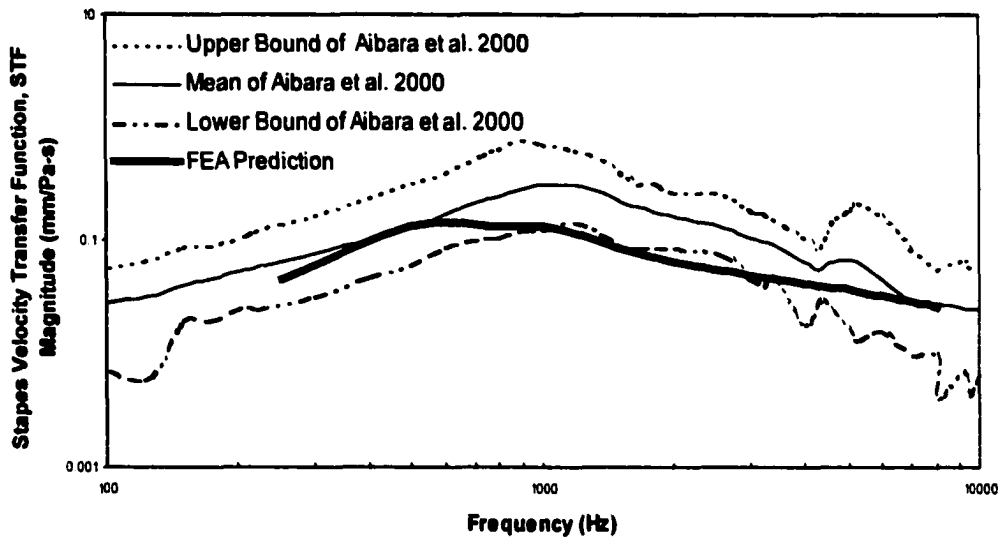
Figure 5.12 Comparison of STF between FEA prediction
and Aibara *et al.* experimental measurements (2000)

5.4.3 Comparison Of The Ratio Of Umbo To Stapes Footplate Displacements

The ratio of the umbo displacement to the stapes footplate displacement reflects the

effectiveness of the middle ear system in coupling sound pressure into the inner ear. For

FE model, the ratio may not be within a reasonable range even though both the stapes

footplate displacement and the umbo displacement are within the reasonable ranges.

Therefore, it is meaningful to test the base-line model by comparing the ratio between

experimental measurements and FE model prediction. The experimental data for the

comparison were calculated from Nishihara *et al.* measurements [Nishihara *et al.* 1993]. The

experimental setup is similar to that described in Section 5.4.1. When a pure tone sound

of 80 dB SPL was delivered to the eardrum, the displacements of the stapes footplate and

the umbo caused by the sound pressure on the eardrum were measured using a laser

Doppler interferometer. The results are plotted in Figure 5.13. The FE model prediction
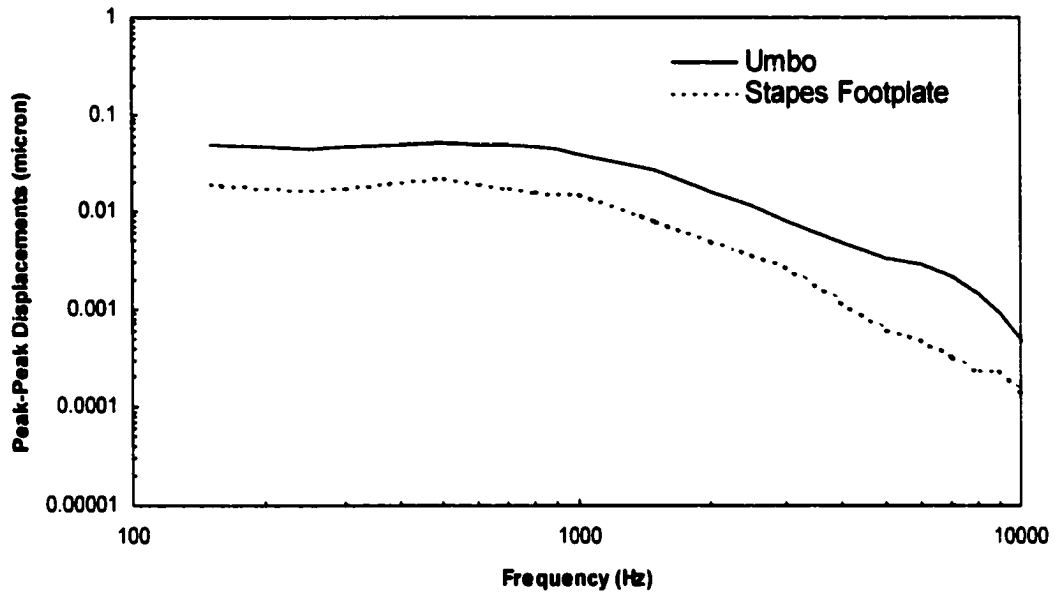
Figure 5.13 Mean peak-to-peak displacement obtained by Nishihara *et al.* 1993
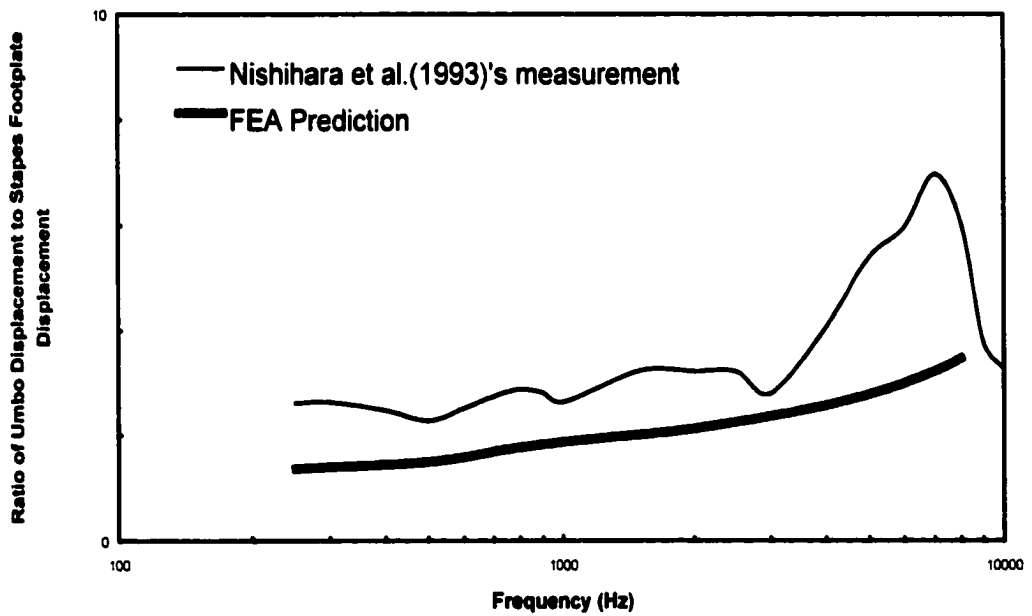
Figure 5.14 Comparison of ratio of umbo displacement to stapes footplate displacement
between FEA prediction and Nishihara *et al.* measurements (1993)

was calculated from the harmonic analysis results on the FE model under a uniform sound pressure of 80 dB SPL. Figure 5.14 shows that the FEA prediction is, in general, consistent with the experimental result.

5.4.4 Comparison Of The Ratio Of Umbo To Malleus Shortprocess Displacements

The ratio of the umbo displacement to the malleus shortprocess displacement reflects the vibration pattern of the malleus that affects the sound transmission in the ossicular chain. Therefore, it is meaningful to test the FE model by comparing the ratio between experimental measurements and FE model prediction. The experimental data for the comparison was calculated from Goode *et al.*'s measurements [Goode *et al.* 1994]. The experimental setup is similar to that of Section 5.4.1. When a pure tone sound of 94 dB SPL was delivered to the eardrum, the displacements of the shortprocess and the umbo caused by the sound pressure on the eardrum were measured using a laser Doppler interferometer. The results are plotted in Figure 5.15. The FE model prediction was calculated from the harmonic analysis results on the FE model under a uniform sound pressure stimulus of 94 dB SPL. Figure 5.16 shows that the FEA prediction is close to the experimental result in most range of frequency when the frequency is greater than 1,000 Hz. However, the prediction is lower than the experimental result in lower frequency range. This experimental result indicates an unstable sound transmission effect from the eardrum to the shortprocess in the entire frequency range, i.e., lower in low frequency and higher in high frequency. The unstable sound transmission is not shown in FE model prediction probably because we used the uniform Young's modulus but non-uniform
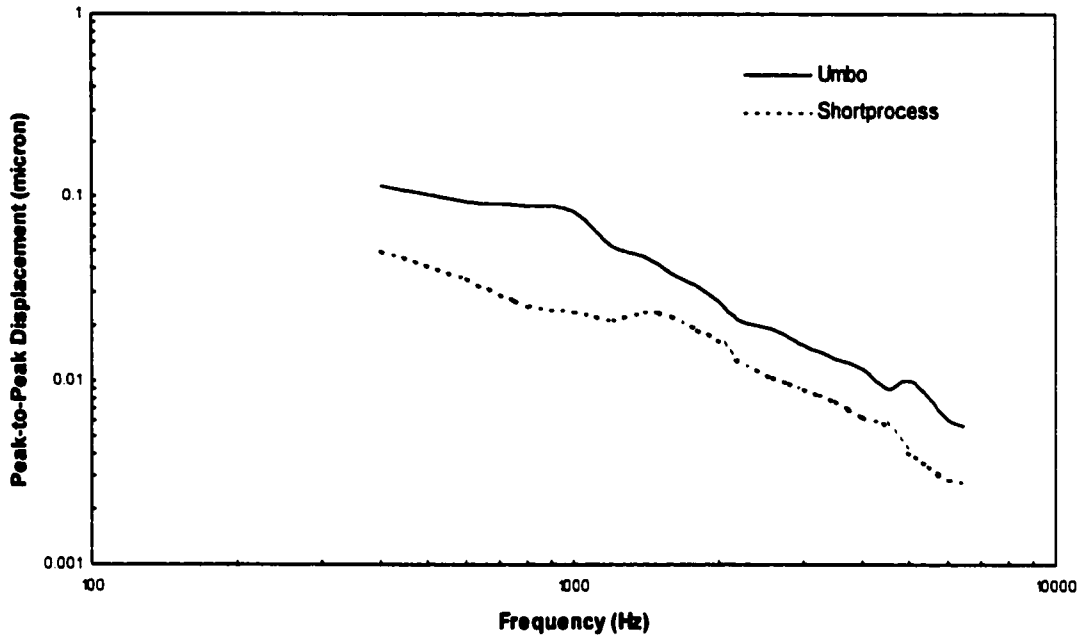
Figure 5.15 Mean peak-to-peak displacement obtained by Goode *et al.* 1994
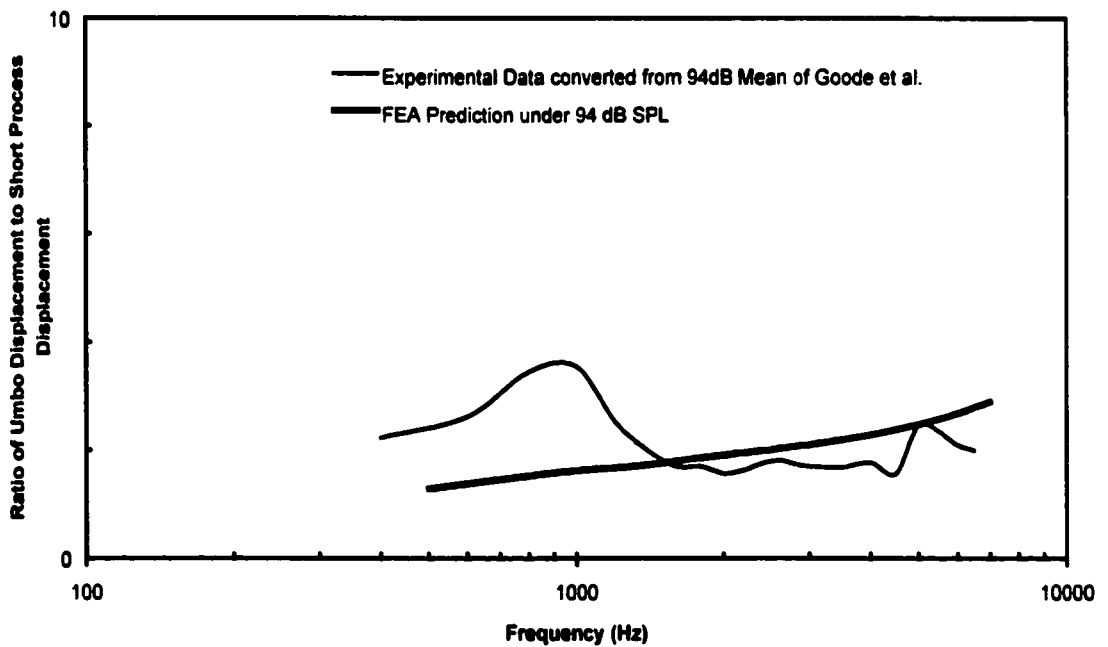

Figure 5.16 Comparison of ratio of umbo displacement to shortprocess displacement
between FEA prediction and Goode *et al.* measurements (1994)

density in malleus in the base-line FE model. The inconsistency of Young's modulus and the density may affect the transmission characteristics in low frequencies.

As discussed above, the verifications of the base-line FE model include four experimental measurements, the umbo displacement, the stapes footplate velocity transfer function, the ratio of the umbo displacement to the stapes footplate displacement and the ratio of the umbo displacement to the malleus short process displacement. The results were measured at three reference points, the umbo, the stapes footplate and the malleus shortprocess. These verifications plus the comparison of the stapes footplate displacements between FEA prediction and Gan *et al.*'s experimental measurements show that the base-line FE model predictions, in general, match the experimental results. It is also noticed that the predictions for the stapes footplate displacement, the umbo displacement and the stapes velocity transfer function are consistently lower than the corresponding mean experimental measurements, especially in the frequency range of 700-2,000 Hz. The difference may be explained as follows:

(1) The individual difference in geometry and material properties induced the difference between the predictions and the experimental results since the base-line model was only based on one temporal bone and one set of mechanical properties. It has been stated that the anatomical and physiologic individual differences of the external and middle ear can induce up to 25 dB individual variation in hearing thresholds, particularly in the frequency range of 1,000~4,000 Hz [Dallos 1973; Fleischer 1978; Goode, Gyo et al. 1986, Goode 1986].

(2) Some of the material properties adopted in the base-line model were assumed or determined by the calibration process, which may not be the actual values.

(3) The ear canal was not included in the FE model. It has been reported that the ear canal acts as a pipe resonator that boosts hearing sensitivity in the range of 2,000-5,000 Hz [Rossing 1990].

(4) The action of the cochlear fluid was linearlized in the FE model. It is not the case in reality, as discussed in Section 5.2.2.

(5) The uniform Young's modulus and non-uniform density were employed in the ossicles in the base-line model. It is not the case in reality. The inconsistency of Young's modulus and the mass density may affect the transmission characteristics in low frequency.

(6) The sound pressure at the eardrum was simplified as uniform pressure load. In reality, the load is non-uniform due to the particular shapes of the eardrum and the ear canal [Stinson 1985].

Although there are some differences between the base-line model predictions and experimental data, we can still conclude that the base-line model is useful for predicting the dynamic behaviors of the middle ear. It is appropriate to use the base-line model to simulate the middle ear frequency response characteristics, which are the major concern in the middle ear sound transmission study.

CHAPTER SIX

APPLICATIONS OF THE BASE-LINE FE MODEL

In this chapter, the base-line FE model will be employed to investigate the dynamic characteristics of human middle ear and support the otologic studies. The investigation includes the dynamic characteristics of normal and altered ears. The otologic applications focused on predicting the dynamic behaviors of the middle ear under various otologic situations.

6.1 Rocking Of The Footplate

In this study, five points along the long and short axes of the stapes footplate were selected to characterize the movements of the footplate, as shown in Figure 6.1. For convenience, the direction normal to the footplate plane was defined as the piston direction. The piston-like movement of the footplate was characterized using the piston-directional displacement of the center point. The rotational movements of the footplate were characterized by two rocking angles: anterior-posterior rocking angle (RA_{a-p}) and superior-inferior rocking angle (RA_{s-i}), as well as two relative rocking angles: relative anterior-posterior rocking angle (RRA_{a-p}) and relative superior-inferior rocking angle (RRA_{s-i}). These rocking angles are defined as:

$$RA_{a-p} = \tan(\frac{d_a - d_p}{l_{long}}), \quad RA_{s-i} = \tan(\frac{d_s - d_i}{l_{short}}) \tag{6.1}$$

$$RRA_{a-p} = \frac{RA_{a-p}}{d_c}, \quad RRA_{s-t} = \frac{RA_{s-t}}{d_c} \tag{6.2}$$

where d_a, d_p, d_s, d_i, and d_c represent the piston-directional displacement at the anterior, posterior, superior, inferior and central point of the footplate respectively; and l_{long}, l_{short} represent the length of the long and short axes of the footplate respectively. The rocking angles provided a way to understand how the footplate rocks. The relative rocking angles allowed us to observe the levels of the rotational movements of the footplate in anterior-posterior plane and inferior-superior plane relative to the piston-like movement.
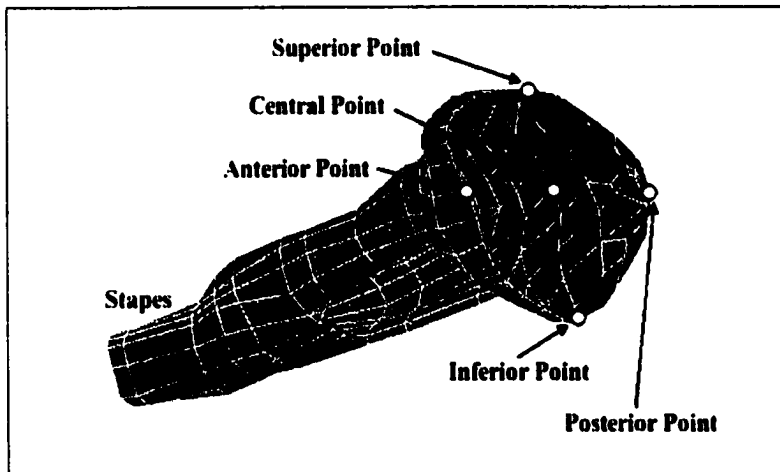
Figure 6.1 Measure points at the stapes footplate

In order to obtain the FE model predictions of these angles in the frequency range of 250-8,000 Hz, the harmonic analysis was conducted using the base-line FE model with a uniform stimulus of 90 dB SPL sound pressures applied on the lateral side of the eardrum. The displacements of the five points were recorded to calculate these angles. Figure 6.2 shows that the anterior-posterior and superior-inferior rocking angles have patterns similar to Prendergast et al.'s calculations, as shown in Figure 6.3, although their

124
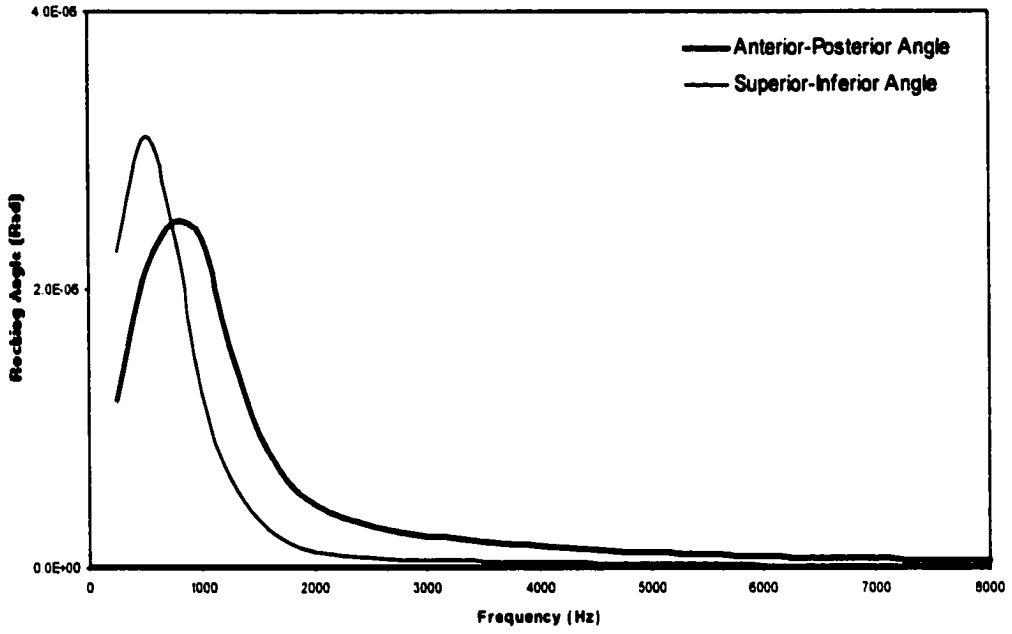
Figure 6.2 Rocking angles as function of frequency
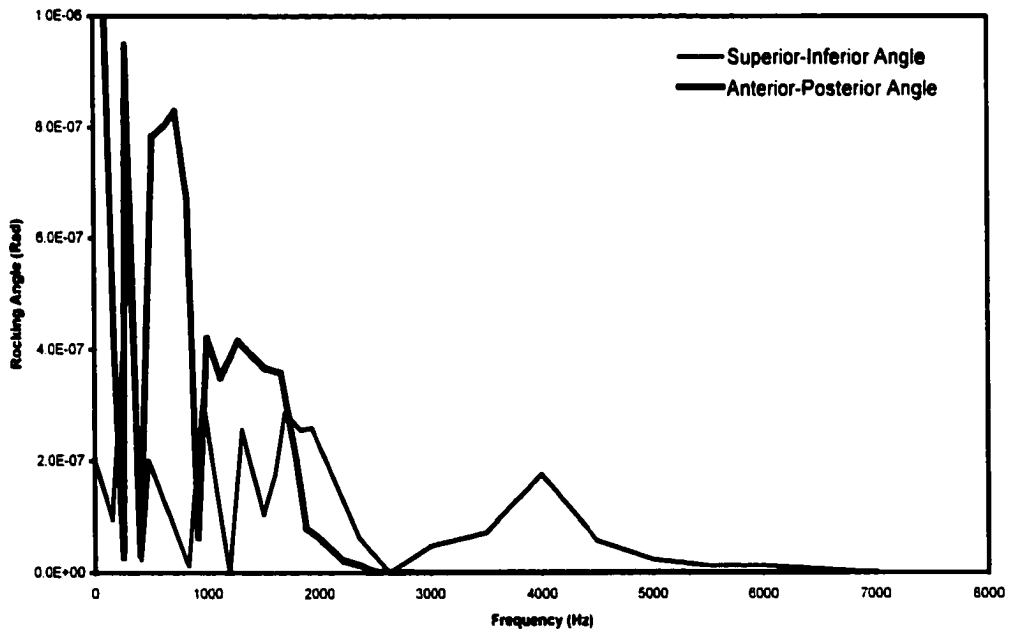
Figure 6.3 Rocking angles as function of frequency calculated
by Prendergast, Ferris *et al.* 1999

curves have more fluctuations [Prendergast, Ferris et al. 1999]. Figure 6.4 indicates that the level of anterior-posterior rocking movement increases with rising frequency but the level of superior-inferior rocking movement reverses. The observation that the level of anterior-posterior rocking movement increases with rising frequency is consistent with Heiland et al.'s experimental conclusion [Heiland et al. 1999]. Between 250-1,000 Hz, the predominant movement is piston-like plus superior-inferior rocking. However, with increasing frequency, the stapes displays increasing anterior-posterior rocking motions.
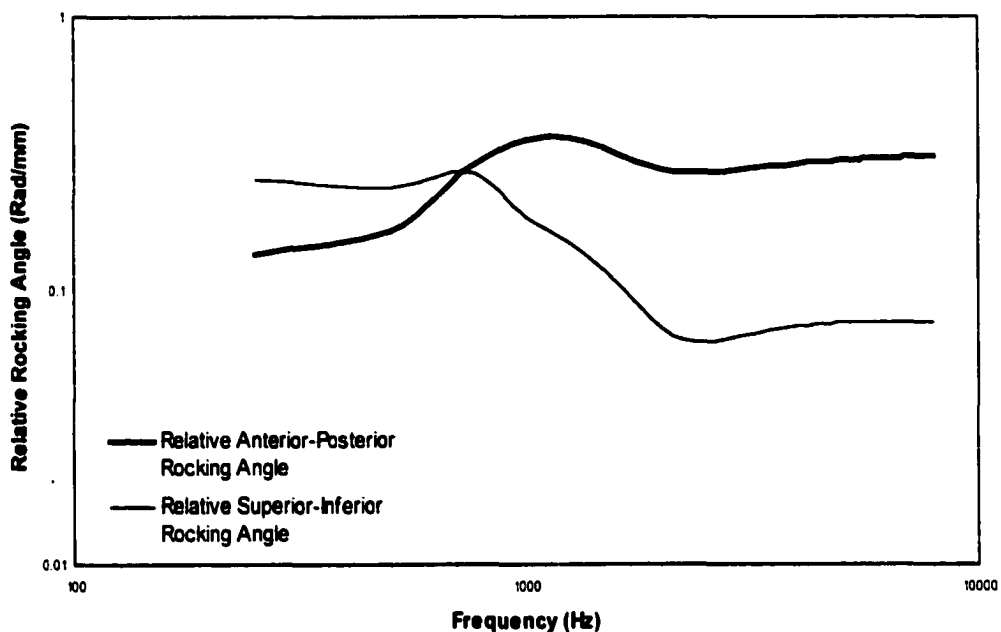
Figure 6.4 Relative rocking angles as function of frequency

As Heiland et al. suggested, the studies might have important clinical implications [Heiland et al. 1999]. If the assumption holds, that is, the piston-like motion of the stapes is the most effective in stimulating the cochlear fluid in vibrations of the stapes, any surgical alteration on the middle ear may increase the non-piston-like motion of the stapes at

126

certain frequencies. As a result, a patient may experience poor post-surgical hearing thresholds at these frequencies. Therefore, it is possible to aid surgical plans by FE analysis on the vibration modes of the stapes before any surgical alteration, for example, the ossicular replacement prosthesis. The behaviors of normal middle ear should always be set as a goal for designing middle ear prosthesis.

6.2 Mass Loading On The Ossicles

The middle ear as a sound transmission system is affected by the mass changes in the ossicular chain. An additional mass loading is detrimental to middle ear function [Ball et al. 1997; Gan et al. 2001]. Therefore, it is helpful for bioengineers to determine the effect of the mass of implants on stapes footplate movement before designing a new implantable device.

In this study, the middle ear base-line FE model was used to predict the variations of the footplate displacement due to different implants. As shown in Figure 6.5, the implant was modeled as a mass block of prescribed mass density using solid elements. The mass
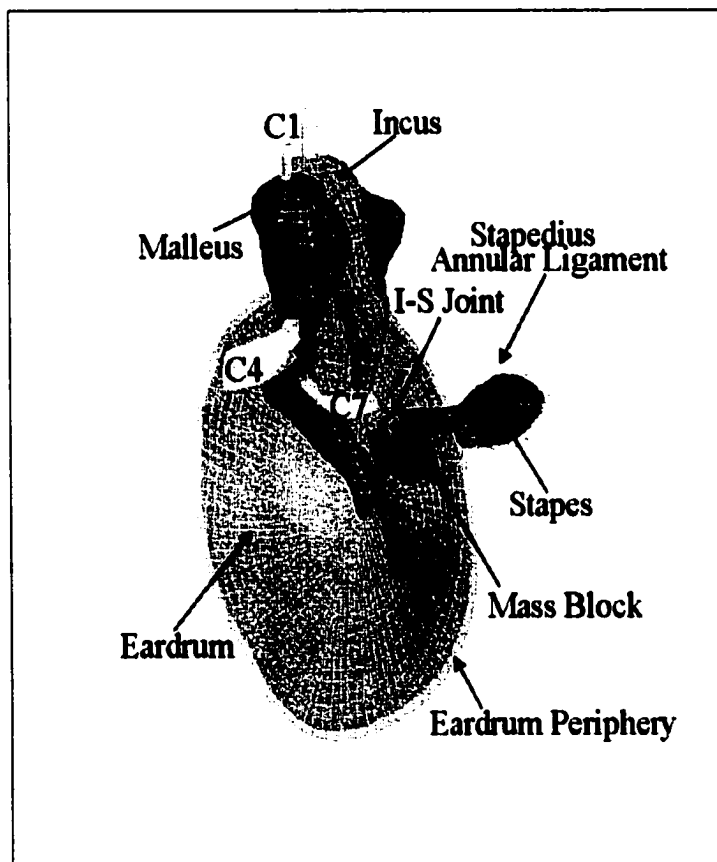
Figure 6.5 FE model of human middle ear with mass block
on incudostapedial joint

block was placed onto the incudostapedial joint to simulate the implant mass loading of a passive middle ear device, such as the SOUNDTEC [TM] Direct System or the Symphonix [TM] Vibrant. Two experimental middle ear implants A and B (weighing 22.5 and 37.5 mg) were used for this study. These two implants were in cylindrical configuration. Both implants were 1.5 mm in diameter, but the implant A was 1 mm shorter than the implant B (3 mm long).

To obtain the displacements of the stapes footplate from the middle ear base-line FE model with two different implants, the harmonic analyses were conducted. Then, the difference of the stapes footplate displacements for the two implants were calculated in dB using the following equation:

$$\delta dB = 20\log(d_A/d_{ref}) - 20\log(d_B/d_{ref}) = 20\log(d_A/d_B) \tag{6.3}$$

where d_A and d_B are the stapes footplate displacements calculated from the base-line FE model with implant A and implant B on the incudostapedial joint, respectively; and d_{ref} is the reference displacement. Therefore δdB is the displacement difference in dB of the two situations. It also indicates how large the displacement improvement can be obtained when the implant mass is reduced.

Using Eq.(6.3) we calculated the variation of footplate displacements in dB due to change of the mass loadings. It is found that 22.5 mg mass loading, compared to the 37.5 mg mass loading, results in an average 3 dB improvement across the frequency range of 250-8,000 Hz. The result was plotted in Figure 6.6 with the broken line. For comparison, the result of an experimental study was plotted with the solid line in the same figure [Gan et al. 2001]. The experimental data show that there is no change in displacement due to the mass reduction at the low frequencies (<1000 Hz). But an obvious improvement at high

frequencies (>3000 Hz) was observed due to the 15 mg (=37.5-22.5) mass reduction. The

base-line model prediction also shows an improvement at high frequencies (>3000 Hz)

similar to the experimental data.
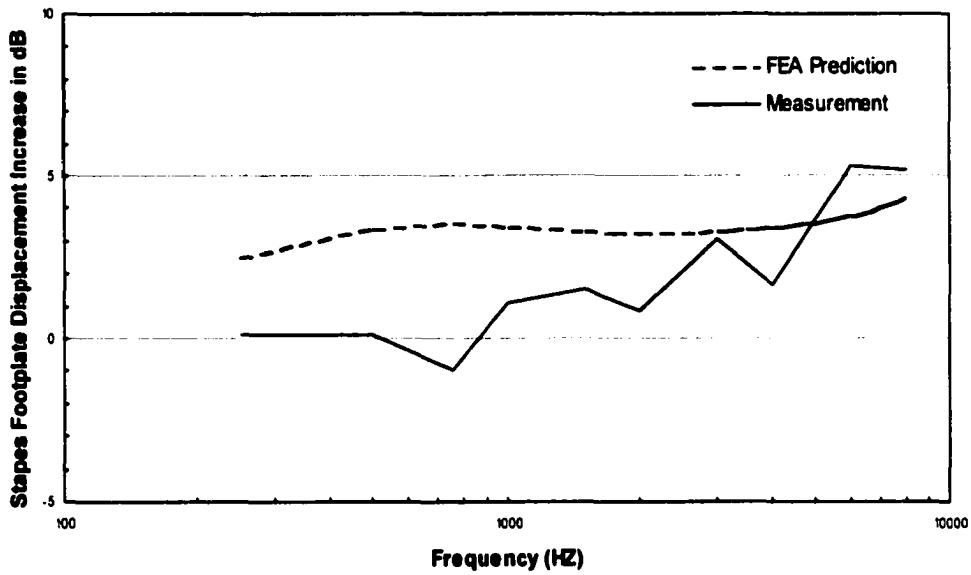
Figure 6.6 Stapes footplate displacement increase due to a 15 mg
mass loading reduction on incudostapedial joint

6.3 Change Of The Eardrum Stiffness

In this study, the influence of eardrum stiffness on stapes footplate displacements was examined using the base-line FE model. The harmonic analyses were conducted using the base-line model under uniform pressure stimuli of 90 dB SPL at the lateral side of the eardrum. The displacements of the stapes footplate for different stiffness of the eardrum pars tensa were collected and plotted in Figure 6.7. In this figure, the solid line represents the normal eardrum, having circumferential Young's modulus of 2.0×10^7 N/m^2 and radial modulus of 3.2×10^7 N/m^2. The dotted line and broken line represent respectively the increment and decrement of the eardrum Young's moduli by a factor of 10. The change was applied to both circumferential and radial values. As shown in Figure 6.7, the stiffness of the eardrum affects the frequency response of the stapes footplate displacement. An increased stiffness (Young's modulus higher than normal) of the eardrum results in reduced stapes displacements at low frequencies (<1250 Hz) and increased displacements at high frequencies (≥1250 Hz). A decreased stiffness of the eardrum results in reduced stapes displacements in a large frequency range (≥350 Hz) and a reverse result in a small frequency range (<350 Hz). These results agree with the predicted effects of the eardrum stiffness on the transmission factor of the middle ear by Koike *et al.* [Koike *et al.* 2000]. The transmission factor was defined as the ratio of the intracochlear pressure to the stimulus pressure in front of the eardrum, which has the similar meaning to the footplate displacement in responding to the input sound pressure level at the eardrum. This suggests that an eardrum-stiffness-related hearing loss can be studied using the base-line model. For this purpose, we have to determine what cause the increase or decrease of the eardrum stiffness.
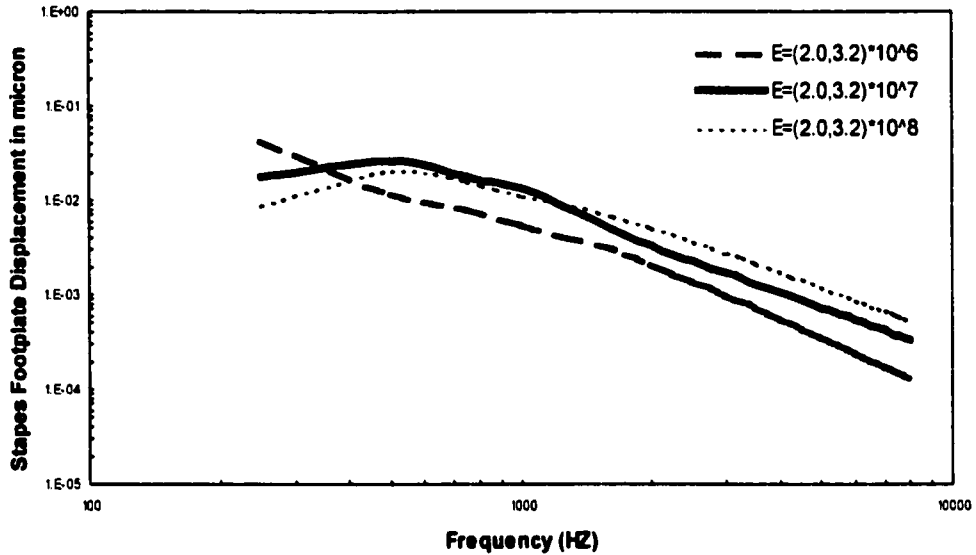
Figure 6.7 Effect of the eardrum stiffness on stapes footplate displacement

These preliminary clinical applications of the base-line model predicted rocking of the footplate, the effects of passive implant mass loading on the ossicles and changes in the eardrum stiffness on middle ear system function. The results suggest that the base-line model is useful in the study of middle ear mechanics and the design of implantable hearing devices. Perforations of the eardrum, otosclerosis, and both passive and active functions of implantable hearing devices may extend the utility of this base-line FE model. In a word, the base-line FE model can provide a convenient, fast and economic way to predict the consequences of diseases and surgeries. It also can be used to support the design of implants and prostheses in selecting materials, configurations and other design parameters. Especially, the base-line FE model can be employed to optimize the positions and orientations of implants and prostheses in the ear by comparing different surgical plans.

132

CHAPTER SEVEN

CONCLUSIONS AND RECOMMENDATIONS

7.1 Conclusions

The research work presented in this dissertation involves the development of a computer-aided geometric modeling method for constructing human middle ear solid models from histological sections of human temporal bone, a computer-integrated finite element modeling method that converts the solid model to the analysis model for human middle ear mechanics, and the preliminary clinical applications of the FE model. The approach provides a tool for physicians and bioengineers to investigate 3D morphometry and dynamic behaviors of human middle ear from 2D histological sections of temporal bones. The outcome is a 3D base-line FE model of human middle ear with accurate geometric representation and relevant clinical applications of the model.

The outcome proves all the hypotheses formulated for the research in Chapter 1. First, the results of Chapters 5 and 6 prove that FEM can be used to appropriately predict the dynamic behaviors of normal, diseased, and altered human middle ears. Second, the results of Chapter 4 prove that an accurate and systematic geometric modeling method can be developed to support the human middle ear FE modeling. Third, the results of Chapters 3 and 5 prove that the FE middle ear models can be successfully calibrated using experimental results to simulate the behaviors of normal ears. Fourth, the results of

Chapter 6 prove that some clinical applications can be characterized by identifying and quantifying FE model parameters.

The outcome also indicates the achievement of all objectives in the research. The major contributions of this research are:

(1) A systematic computer-aided geometric modeling method for constructing accurate human middle ear solid models in computer.

(2) A computer-integrated finite element modeling procedure for the human middle ear.

(3) A thorough review on the mechanical properties of human middle ear.

(4) An experimentally verified base-line FE model of human middle ear.

(5) Three successful applications of the base-line FE model for investigating the dynamic behaviors of normal and altered human middle ears.

The computer-aided geometric modeling method was developed to accurately reconstruct the geometry of human middle ear. The accurate geometry is essential for realistic middle ear dynamic analysis. The method begins with the histological section slide preparation of human temporal bone. The section slides are scanned into computer and calibrated into standard section images. The section images are then digitized to construct the geometry of human middle ear using the curve fitting and surface skinning techniques and CAD tool. This method is accurate, systematic, general and low cost. By employing the histological sections of human temporal bone, the accurate details of the structure are captured. By the systematic imaging process, the mismatch of component contours due to inevitable operation errors is minimized. By the error control scheme implemented in the curve fitting for image contours, the reconstructed geometry can be close to the real middle ear structure within a prescribed error bound. The standardized

procedure makes the method easy to follow and eliminates potential inconsistency and mistakes. The fewer requirements for laboratory instruments and computer software tools make the method cost effective. Most importantly, it is applicable to structures with complicate geometry, various topology, and different physical sizes. This method works especially well with small-size structure and complicate geometry like human middle ear. The solid geometric model of human middle ear has been proven to be a good basis for fabricating the physical model and building the FE model of human middle ear.

The computer-integrated FE modeling method was developed to predict the dynamic behaviors of the middle ear. The method begins with the generation of finite element meshes of human middle ear. The anatomic characteristics and functions of the middle ear are incorporated in to the FE model by assigning different material properties to different parts of the middle ear system. Most material properties are selected based on a thorough investigation about the mechanical properties of the middle ear. The remaining material properties are assumed partially through engineering reasoning and partially by the FE model calibration process. By perturbing model parameters in a restrictive manner, the FE model is calibrated to match the FE model prediction with the laser Doppler interferometry measurements of the stapes footplate displacement. The procedure produces the base-line FE model of human middle ear.

The base-line model is verified by using four independent experimental measurements. The verifications test three points, the umbo, the stapes footplate and the malleus shortprocess, of the FE model using these measurements. The verifications show that the FE model predictions match the experimental results well. Therefore, we believe that the base-line FE model is very useful for predicting the dynamic behaviors of the

middle ear. It is appropriate to investigate the middle ear frequency response characteristics using the base-line model, which are the major concern of the middle ear sound transmission study.

The detailed review about the mechanical properties of the middle ear is crucial for building and finalizing the FE model. It will also benefit future research related to middle ear mechanics.

Movement of the stapes footplate generally represents the mechanical output of the middle ear in response to sound input at the eardrum. In the application studies, the displacement of the stapes footplate was selected as the primary variable. The clinical applications of the base-line model predicted the rocking of the normal ear, the effects of passive implant mass loading on ossicles, and the effects of eardrum stiffness variation on the middle ear system function. The results suggest that the finite element model is useful in the study of middle ear mechanics and the design of implantable hearing devices. Perforations of the eardrum, otosclerosis, and both passive and active functions of implantable hearing devices may extend the usage of the base-line FE model.

7.2 Recommendations

The purpose of the section is to discuss additional research issues that ought to be explored to advance our understanding on the middle ear mechanics. There are several areas in which the current research may be expanded.

7.2.1 Finite Element Model Of The Middle Ear

The efficacy of the base-line FE model can be further improved by adding more ear components related to sound transmission into the model. These components include the external ear canal, the middle ear cavity and the cochlea. Adding these components will simulate the real sound transmission process from the external ear to the inner ear by the ossicular chain. The ear canal and middle ear cavity can be modeled using acoustic elements to form the real sound pressure distribution on the eardrum and the real vibration environment for the middle ear. The cochlea can be modeled using fluid elements that will effectively realize the real cochlear input impedance. In the model, an additional boundary will be applied at the Eustachian tube, and the sound pressure can be applied at the open end of the ear canal. The new FE model, once developed, will be suitable to predict the sound transmission characteristics for the entire ear including outer, middle and inner ears. It also provides a possibility to investigate the effect of the perforation of the eardrum and the injury of the ear due to violent environmental factors such as blasts, abrupt environmental pressure change, intense noise, etc.

7.2.2 Multibody Model Of The Middle Ear

The multibody dynamic analysis of human middle ear serves as one of the theoretical

bases of the artificial ear. To prepare for the multibody analysis of the middle ear, the mass properties of the ossicles, including the mass, the center of mass and the moments of inertia, can be calculated easily based on the CAD model of the middle ear using SolidWorks. The multibody model is also suitable to explore the dynamic behaviors of the incudomalleolar and incudostapedial joints.

7.2.3 Material Property Test Of The Ear System

In FE modeling of human middle ear, the most difficult task is to find the real mechanical properties of the middle ear system. Unfortunately, there is still lack of experimental data for a complete set of material properties. In the base-line FE model, some mechanical properties came from estimates. The base-line FE model was finalized by the FE model calibration process that yields the best estimates of the mechanical properties. We need more accurate mechanical property data for better models that will produce more accurate predictions.

7.2.4 Identifications Of The Mechanical Parameters Related To Clinical
Situations

For successful clinical applications using the FE model, the relations between the FE model parameters and the clinical situations, such as diseases and aging, must be first identified. Once the work is completed, the FE model can be used to explore various clinical situations in computer using the variations of the model parameters as input. It is a fast and less expensive way to understand how various diseases affect the middle ear function. The implementation of the work will require more collaboration between bioengineers and physicians.

REFERENCES

[1]   3D Systems, Co. http://www.3dsystems.com

[2]   Adobe Systems Incorporated. http://www.adobe.com

[3]   Aibara R, Welsh JT, Puria S, Goode RL. *Human middle ear sound transfer function and cochlear input impedance* in The function and mechanics of normal, diseased and reconstructed middle ears (edited by Rosowski J and Merchant S). Kugler Publications. Netherlands. 2000. 71-88.

[4]   American Optical Corporation. American Optical no longer makes AO microtomes that are now manufactured by Leica Microsystems. http://www.leica.com

[5]   Altair Computing Inc. *HyperMesh 2.1 reference manual.* Altair Computing, Inc. 1757 Maplelawn Drive, Troy, MI. 1997

[6]   Altair Computing, Inc. *HyperMesh 2.1 user's manual.* Altair Computing, Inc. 1757 Maplelawn Drive, Troy, MI. 1997

[7]   Anson B J, Donaldson J A. *Surgical anatomy of temporal bone.* W B Saunders Company. 1981.

[8]   Autodesk, Inc. AutoCAD Release 13 user's guide. Autodesk, Inc. 111 McInnis Parkway, San Rafael, CA 94903. 1995

[9]   ÄWengen DF, Nishihara S, Kurokawa H, Goode RL. Measurements of the stapes superstructure. *Ann Otol Rhinol Laryngol* 1996; 104:311-316.

[10]   Ball GR, Huber A, Goode RL. Scanning laser Doppler vibrometry of the middle ear ossicles. ENT Journal. Vol 76 (4). 1997.

[11]   Beer HJ, Bornitz M, Drescher J, Schmidt R and Hardtke HJ. *Finite element modeling of the human eardrum and applications.* Proceedings of the international workshop on middle ear mechanis in research and otosurgery. Dresden, Germany. 1996: 40-47

[12]   Beer HJ, Bornitz M, Hardtke HJ, Schmidt R, Hofmann G, Vogel U, Zahnert T and Hüttenbrink KB. *Modeling of components of the human middle ear and simulation of their dynamic behaviour.* Audiol Neurootol. Vol 4. 1999. 156-162

[13] Blayney AW, Williams KR, Rice HJ. *A dynamic and harmonic damped finite element analysis model of stapedotomy.* Acta Otolaryngol (Stockh). Vol 117(2). 1997: 269-273

[14] Bornitz M, Zahnert, Hardtke HJ and Hüttenbrink KB. *Identification of parameters for the middle ear model.* Audiol Neurootol. Vol 4. 1999: 163-169

[15] Carl Zeiss, Inc. http://www.zeiss.com

[16] Dallos P. *The auditory periphery—biophysics and physiology.* Academic Press. New York.1973

[17] DeBoor C. *A practical guide to splines.* Springer-Verlag, New York. 1978.

[18] Donahue D, Gussen R. *Rapid parlodion embedding of temporal bones.* Arch Otolaryn. Vol 83. Jan 1966.

[19] Drescher J, Schmidt R, Hardtke HJ. *Finite element modeling and simulation of human tympanic membrane.* HNO. 146(2). 1998: 129-134

[20] Eiber A. *Mechanical modeling and dynamical investigation of middle ear.* Proceedings of the international workshop on middle ear mechanics in research and otosurgery. Dresden, Germany. 1996: 61-66

[21] Empire Level Mfg. Corp. http://www.empirelevel.com

[22] Ferris P, Prendergast PJ. *Middle-ear dynamics before and after ossicular replacement.* J Biomechanics. Vol 33. 2000: 581-590

[23] Fleischer G. *Evolutionary principles of the mammalian ear.* Adv Anat Embryol Cell Biol. Vol 5(5). 1978: 1-70

[24] Fujiyoshi T, Mogi G, Watanabe T and Matsushita F. *Undecalcified temporal bone morphology: a methodology useful for gross to fine observation and three-dimensional reconstruction.* Acta Otolaryngol (stockh). Suppl 493. 1992: 7-13

[25] Funnell WRJ, Decraemer WF, Khanna SM. *On the damped frequency response of a finite element model of the cat eardrum.* J Acoust Soc Am. Vol 81. 1987: 1851-1859

[26] Funnell WRJ, Khanna SM, Decraemer WF. *On the degree of rigidity of the manubrium in a finite element model of the cat eardrum.* J Acoust Soc Am. Vol 91 (4 pt 1). 1992: 2082-2090

[27] Funnell WRJ, Laszlo CA. *A critical review of experimental observations on eardrum structure and function.* ORL. Vol 44. 1982: 181-205

[28] Funnell WRJ, Laszlo CA. *Modeling of the cat eardrum as a thin shell using the finite element method.* J Acoust Soc Am. Vol 63. 1978: 1461-1467

[29] Funnell WRJ. *Low-frequency coupling between eardrum and manubrium in a finite element model.* J Acoust Soc Am. Vol 99 (5). May 1996: 3036-3043

[30] Funnell WRJ. *On the undamped natural frequencies and mode shapes of finite element analysis of the cat eardrum.* J Acoust Soc Am. Vol 73 .1983: 1657-1661

[31] Fung YC. *Biomechanics: mechanical properties of living tissues* (2nd Ed.). Springer-Verlag. New York. 1996

[32] Gan RZ, Dyer, RK, Wood MW, Dormer KJ. *Mass loading on ossicles and middle ear function.* Annals of Otology, Rhinology, and Laryngology. Vol 110 (5). 2001:478-485.

[33] Gan RZ. *Laser interferometry and finite element modeling for middle ear implant transfer functions.* Research Proposal submitted to The Whitaker Foundation. 1998

[34] Gatti PL, Ferrari V. Applied structural and mechanical vibrations: theory, method and measuring instrumentation. E & FN SPON. London. 1999

[35] Goode RL. *Middle ear function, biologic variation and otosurgical alchemy: can we turn tin ears into gold?* Arch Otolaryngol Head Neck Surg. Vol 112. 1986: 923-924

[36] Goode RL, Gyo K, Aritomo H, Gonzalez J. *Surgery for sensorineural hearing loss mechanism, diagnosis, treatment.* Proceedings Scott M. Reger Memorial Conference (edited by Lee HJ and Glattke T). University of Iowa Press. Iowa City. 1986: 253-275

[37] Goode RL, Killian M, Nakamura K, Nishihara S. New knowledge about the function of the human middle ear: development of an improved analog model. American J Otol. Vol 15(2). 1994: 145

[38] Graham M D, Reams C, Perkins R. *Human tympanic membrane: malleus attachment.* Ann. Otol. Rhinol. Laryngol. Vol 87. 1978: 426-431

[39] Guinan J J Jr., Peake W T. *Middle ear characteristics of anesthetized cats.* J Acoust Soc Am. Vol 41. 1967: 1237-1261

[40] Gulick WL, Gescheider GA, Frisina RD. *Hearing: physiological acoustics, neural coding, and psychoacoustics.* Oxford University Press. New York. 1989

[41] Hart GC, Wong K. *Structural dynamics for structural engineers.* John Wiley & Sons, Inc. 2000.

[42] Heiland KE, Goode RL, Asai M, Huber AM. A human temporal bone study of stapes footplate movement. The American Journal of Otology. Vol 20 (1). 1999:81-86

[43] Helmholtz HFL (translated by Hinton J). *The mechanics of the ossicles and the membrane Tympani.* New Sydenham Society, London. Vol 62. 1874. 97-155

[44] Herrmann G, Liebowitz H. *Chapter 10 Mechanics of bone fractures* in Fracture: an advanced treatise Vol VII (edited by Liebowitz H). Academic Press, New York. 1972. 772-840

[45] Hewlett-Packard. http://www.hp.com

[46] Hudde H, Weistenhöfer C. *A three-dimensional circuit model of the middle ear.* Acustica United with acta acustica. Vol 83 (3). 1997: 535-549.

[47] Hüttenbrink KB. *The mechanics of the middle-ear at static air pressures: the role of the ossicular joints, the function of the middle-ear muscles and the behaviour of stapedial prostheses.* Acta Otolaryngol Suppl. 1988; 451: 1-35

[48] Igarashi M. The inner ear anatomy of the squirrel monkey: the study of horizontal serial sections. NASA Joint Report, Monogragh No.8. US Naval School of Aviation Medicine. 1964.

[49] Igarashi M, Ohashi K, Ishii M. *Morphometric comparison of endolymphatic and perilymphatic spaces in human temporal bones.* Acta Otolaryngol 101. 1986:161-164

[50] Jacobs PF. *StereoLithography and other RP&M technologies.* ASME Press, New York, NY, 1994.

[51] Kirikae I. *The structure and function of the middle ear.* Tokyo: University of Tokyo Press, 1960.

[52] Koike T, Wada H, Kobayashi T, Takasaka T. *Finite element method (FEM) analysis of human middle- ear.* Procedings of the ARO meeting. 1996.

[53] Koike T, Wada H, Kobayashi T. *Analysis of the finite-element method of transfer function of reconstructed middle ear and their postoperative changes* in The function and mechanics of normal, diseased and reconstructed middle ears (edited by Rosowski J and Merchant S). Kugler Publications. Netherlands. 2000. 309-320

[54] Kringlebotn M. *Network model for human middle ear.* Scan Audiol. Vol 17. 1988: 75-85.

[55] Ladak HM, Funnell WRJ. *Finite element modeling of the normal and surgically repaired cat middle ear.* J Acoust Soc Am. Vol 100 (2 pt 1). 1996: 933-944

[56] Lee K. *Principles of CAD/CAM/CAE Systems.* Addison-Wesley. Reading, Massachusetts. 1999

[57] Lesser THJ, Williams KR, Blayney AW. *Mechanics and materials in middle ear reconstruction.* Clin Otolaryngol. Vol 16. 1991: 29-32

[58] Lesser THJ, Williams KR, Skinner DW. *Tympanosclerosis, grommets and shear stress.* Clin Otolaryngol. Vol 13. 1988: 375-380

[59] Lesser THJ, Williams KR. *The tympanic membrane in cross section: A finite element analysis.* J Laryngol Otol. Vol 102. 1988: 209-214

[60] Lim DJ. *Human tympanic membrane.* Acta Otolaryngology. Vol 70(3). 1970: 176-186

[61] Lim DJ. *Tympanic membrane: electron microscopic observation, Part 1, pars tensa.* Acta Otolaryngology. Vol 66(6). 1968: 181-198

[62] Lynch TJ, Nedzelnitsky V and Peake WT. *input impedance of the cochlea in cat.* J Acoust Soc. Am. Vol 72. 1982: 108-130

[63] MacNeal-Schwendler Corporation. MSC/Patran Version 7.5 release guide. 1998

[64] Merchant SN, Ravicz ME, Puria S, Voss SE, Whittemore KR Jr., Peak WT and Rosowski JJ. *Analysis of middle ear mechanics and application to diseased and reconstructed ears.* The American J of Otology. Vol 18. 1997: 139-154

[65] Merchant SN, Ravicz ME, Voss SE, Peak WT and Rosowski JJ. *Midder ear mechanics in normal, diseased and reconstructed ears.* J Laryngology and Otology. Vol 112. August 1998: 715-731

[66] Mortenson ME. *Geometric modeling.* John Wiley & Sons, Inc. New York. 1985

[67] Nishihara S, Aritomo H, Goode RL. *Effect of changes in mass on middle ear function.* Otolaryngol Head Neck Surg. 109 (5). Nov.1993. 899-910

[68] Nishihara S, Goode RL. *Measurement of tympanic membrane vibration in 99 human ear.* Proceedings of the international workshop on middle ear mechanics in research and otosurgery. Dresden, Germany. 1996. 91-93

[69] Onchi Y. *A study of the mechanism of the middle ear.* J Acoust Soc Am. Vol 21(4). July 1949: 404-410

[70] Peake WT, Rosowski JJ, Lynch TJ. *Middle-ear transmission: acoustic versus ossicular coupling in cat and human.* Hearing Research. Vol 57(2). 1992:245-268

[71] Prendergast PJ, Ferris P, Rice HJ, Blayney AW. *Vibro-acoustic modeling of the outer and middle ear using the finite element method.* Audiol Neurootol. 4(3-4). 1999: 185-191

[72] Prendergast PJ, Kelly DJ, Rafferty M, Blayney AW. *The effect of ventilation tubes on stresses and vibration motion in the tympanic membrane: a finite element analysis.* Clin Otolaryngol. Vol 24. 1999: 542-548

[73] Rabbitt RD, Holmes MH. *A fibrous dynamic continuum model of the tympanic membrane.* J Acoust Soc Am. Vol 80 (6). December 1986: 1716-1728

[74] Reklaitis G V, Ravindran A, Ragsdell K M. *Engineering optimization: methods and applications.* Wiley. New York. 1983

[75] Roberson RE, Schwertassek R. Dynamics of multibody systems. Springer-Verlag. Berlin. 1988

[76] Rogers DF, Fog NG. *Constrained B-Spline curve and surface fitting.* Computer-Aided Design. Vol 21 (10). 1989: 641-648

[77] Rosowski JJ. *Models of external- and middle ear function.* In Auditory Computation. Springer Handbook Of Auditory Research (Edited by Fay RR, Popper AN). Springer. New York. 1996

[78] Rossing T D. *The science of sound.* Addison-Wesley Publishing Company, Inc. 1990.

[79] SAS IP Inc. *ANSYS elements reference.* Seventh Edition. 1998a

[80] SAS IP Inc. *ANSYS structural analysis guide.* First Edition. 1998b

[81] Shimada T, Lim DJ. *The fiber arrangement of the human tympanic membrane: a scanning electron microscopic observation.* Ann Otol Rhinol Laryngol. Vol 80(3). 1971: 319-329

[82] Silverstein H, Wolfson R J, Rosenberg S. *Diagnosis and management of hearing loss.* Clinical Symposia. Vol 44 (3). 1992.

[83] SolidWorks Corporation. *SolidWorks98 user's guide.* SolidWorks Corporation. 150 Baker Avenue Ext., Concord, MA. 1998

[84] Spatial Corp. *The ACIS 4.0 Save File (SAT) format manual.* Spatial Corp. 2425 55th Street, Suite 100, Boulder, CO.

(Online File: http://www.spatial.com/support/publications/satfile.htm)

[85] Speirs AD, Hotz MA, Oxland TR, Häusler R, Nolte L-P. *Biomechanical properties of sterilized human auditory ossicles.* J of Biomechanics. Vol 32. 1999:485-491

[86] Stinson MR. *The spatial distribution of sound pressure within scaled replicas of the human ear canal.* J. Acoust. Soc. Am. Vol 78 (5). 1985: 1596-1602

[87] Stuhmiller JH. *Use of modeling in predicting tympanic membrane rupture.* Ann Otol Rhinol Laryngol. Vol 98. 1989: 53-60

[88] Szabó B, Babuška I. *Finite element analysis.* John Wiley & Sons, Inc. 1991

[89] Takagi A and Sando I. *Computer-aided three-dimensional reconstruction: a method of measuring temporal bone structures including the length of the cochlea.* Ann Otol Rhinol Laryngol. Vol 98. 1989: 515-522

[90] Takahashi H, Sando I and Takagi A. *Computer-aided three-dimensional reconstruction and measurement of the round window niche.* Laryngoscope. Vol 99. May 1989: 505-509

[91] Tang P-S. Integration of topology and shape optimizations for design of structural components. MS Thesis. The University of Oklahoma, Norman, OK. 1999

[92] Vlaming M S M G and Feenstral. *Studies on the mechanics of the normal human ear.* Clinical Otolaryngology. Vol 11. 1986: 353-363

[93] Vlaming M S M G. *Middle ear mechanics by laser Doppler interferometry.* Ph.D. Dissertation. Techniche Universiteit Delft, Delft. 1987

[94] VMBHRC (The University of Washington's Virginia Merrill Bloedel Hearing Research Center). *Hearing Loss.* http://depts.washington.edu/hearing/. 2000: Information Articles > Hearing Loss

[95] von Békésy G. *Experiments in hearing.* McGraw-Hill. New York. 1960

[96] von Békésy G. *The structures of the middle ear and the hearing of one's own voice by bone conduction.* J Acoust Soc Am. Vol 21(3). 1949: 217-232

[97] Wada H, Kobayashi T. *Dynamic behavior of middle ear: theoretical study corresponding to measurement results obtained by newly developed measuring apparatus.* J Acoust Soc Am. Vol 87. 1990: 237-245

[98] Wada H, Koike T, Kobayashi T. *Three-dimensional Finite-element method (FEM) analysis of the human middle ear.* Proceedings of the international workshop on middle ear mechanics in research and otosurgery. Dresden, Germany. 1996: 76-80

[99] Wada H, Metoki T, Kobayashi T. *Analysis of dynamic behavior of human middle ear using a finite method.* J. Acoust Soc Am. Vol 92 (6). December 1992: 3157-3168

[100] Weistenhöfer C, Hudde H. *Determination of the shape and inertia properties of human auditory ossicles.* Audiol Neurootol. Vol 4. 1999: 192-196

[101] Wever EG, Lawrence M. *'Physiological acoustics'.* Princeton University Press. Princeton. 1954: 416-417

[102] Williams KR and Lesser THJ. *A dynamic and natural frequency analysis of the FISCH II spandrel using the finite element method.* Clin Otolaryngol. Vol 17(3). 1992: 261-270

[103] Williams KR, Blayney AW, Lesser THJ, *A 3-D finite element analysis of the natural frequencies of vibration of a stapes prosthesis replacement reconstruction of the middle ear.* Clin Otolaryngol. Vol 20. 1995: 36-44

[104] Williams KR, Blayney AW, Lesser THJ. *Mode shapes of a damaged and repaired tympanic membrane as analysed by the finite element method.* Clin Otolaryngol. Vol 22. 1997: 126-131

[105] Williams KR, Blayney AW, Rice HJ. *Middle ear mechanics as examined by the finite element method.* Proceedings of the international workshop on middle ear mechanis in research and otosurgery. Dresden. Germany. 1996a: 67-74

[106] Williams KR, Blayney AW, Rice HJ. *Development of a finite element model of the middle ear.* Rev Laryngol Otol Rhinol (Bord). Vol 117(3). 1996b: 259-264

[107] Williams KR, Lesser THJ, *A finite element analysis of the natural frequencies of vibration of the human tympanic membrane Part I.* Br J Audiol. Vol 24(5). 1990: 319-327

[108] Williams KR, Lesser THJ, *Natural frequencies of vibration of a fiber supported human tympanic membrane analyzed by the finite element method.* Clin. Otolarngol. Vol 18. 1993: 375-386

[109] Zahnert T, Schmidt R, Hüttenbrink KB and Hardtke HJ. *FE-simulation of vibrations of the dresden middle ear prosthesis.* Proceedings of the international workshop on middle ear mechanis in research and otosurgery. Dresden. Germany. 1996: 200-206

[110] Zwislocki J. *The role of the external and middle ear in sound transmission.* In The Nervous System. Vol 3. Human Communication and Its Disorders (Edited by Tower DB). Raven Press. New York. 1975: 45-55

146